QATAR UNIVERSITY

COLLEGE OF ENGINEERING

WAVE PROPAGATION IDENTIFICATION OF VISCOELASTIC AND METALLIC MECHANICAL METAMATERIALS

BY

RATIBA FATMA GHACHI

A Dissertation Submitted to

the College of Engineering

in Partial Fulfillment of the Requirements for the Degree of

Doctorate of Philosophy in Civil Engineering

June 2021

COMMITTEE PAGE

The members of the Committee approve the Dissertation of
Ratiba Fatma Ghachi defended on 18/04/2021.

Dr. Wael Alnahhal
Thesis/Dissertation Supervisor

Dr. Khairedin Abdalla
Committee Member

Prof. Sadok Sassi
Committee Member

Approved:

Khalid Kamal Naji, Dean, College of Engineering

ABSTRACT

GHACHI, RATIBA, F., Doctorate : June : 2021, Doctorate of Philosophy in Civil Engineering

Title: Wave Propagation Identification of Viscoelastic and Metallic Mechanical Metamaterials

Supervisor of Dissertation: Wael, I, Alnahhal.

Mechanical Metamaterials (MMs) are artificially engineered composites which have unconventional mechanical properties that stem from their microstructural geometry rather than from their chemical composition. Several studies have shown the effectiveness of viscoelastic MMs in vibration attenuation due to their inherent vibration dissipation properties. This study investigates different metamaterial wave transmission properties, namely viscoelastic phononic crystals and plates with locally resonant zigzags, hence giving rise to the two MMs vibration attenuation phenomena called Bragg scattering and local resonance. First, an analytical dispersion relation of an arbitrary multilayered crystal using the transfer matrix method was investigated. The analytical results from this computation served as a topology design tool for bilayered phononic crystals later in the study. Second, a multi-objective optimization was introduced to find the viscoelastic phononic crystal with the lowest vibration transmission in a targeted frequency range. Another objective was optimization of the phononic crystal mass since inertia correlates with vibration attenuation. Experimental testing and finite element analysis were used to support the optimization procedure. An electrodynamic shaker was used to measure the vibration transmission of the three control specimens and the optimal specimen in the frequency range of 1 to 1200Hz.

The test results demonstrated that the optimized specimen provided better vibration attenuation than the control specimens by both having a band gap starting at a lower frequency and having less transmission at its passband. Third, in order to explore another type of vibration attenuation mechanism, namely local resonance, a genetic algorithm optimization of zigzag cutouts was developed for an optimal zigzag mass and stiffness and localization in two types of thin cantilever aluminum plates. The objective of the optimization was to cut out optimal zigzags so as to attenuate vibration in a specific frequency range and consequently transform the resonance frequency band around the plate's natural frequency to a low transmission zone. The effectiveness of the proposed optimization was demonstrated numerically and experimentally. Lastly, the nonlinear vibration attenuation properties of the viscoelastic MMs were investigated. The electrodynamic shaker was used to investigate the wave motion through MMs. However, the nonlinear behavior viscoelastic constituent of the crystal made it difficult for the proper identification with low amplitude tests. Therefore, a modified SHPB setup was used to investigate the impulse-dependent behavior of viscoelastic phononic crystals. The proposed modified SHPB setup was a hybrid SHPB with an aluminum input bar and a nylon output bar to bypass the conventional SHPB limitations such as high signal-to-noise ratios and low incident impulse. Experimental results demonstrated a good agreement between the low transmission zones observed in the shaker test and their counterparts in the SHPB tests. Nevertheless, new low transmission zones appeared in the SHPB high-impulse test results that were not shown in the shaker test results with linear harmonic excitation.

DEDICATION

To Adem.

ACKNOWLEDGMENTS

The work described in this dissertation was carried out at the Department of Civil and Architectural Engineering at Qatar University. First, I would like to express my sincere gratitude to my advisor, Dr. Wael Alnahhal, for his continuous support during my Ph.D. research, for his patience, motivation, and guidance.

I would also like to thank my committee members, Prof. Sadok Sassi and Dr. Khairedin Abdalla for their time and valuable feedback.

I would like to acknowledge the financial support provided by the Qatar National Research Fund (a member of Qatar Foundation) via the National Priorities Research Program, project number NPRP-8-1568-2-666.

I am very grateful to my publications' coauthors: Dr. Jongmin Shim, Prof. Amjad Aref, and Dr. Jamil Renno for giving me the opportunity to work under their direction and vision.

Special thanks are due to Center for Advanced Materials (CAM) for providing access to their expert Material testing equipment.

I would like to express my sincere gratitude to, Dr. Osama Abdeljaber and Eng. Yehia Elsaid and Eng Antonio Gonzales. Their continuous support has been key to the success of this work.

Finally, these acknowledgments would not be complete without expressing my sincere gratitude to my late parents Mohamed Ali Ghachi and Wafa Hanafi; my husband Adem Allalou and my sister Anissa Ghachi. Without their infinite support, it would have been impossible to reach such level of education.

TABLE OF CONTENTS

LIST OF TABLES

LIST OF FIGURES

LIST OF ABBREVIATIONS

ABS	Acrylonitrile Butadiene Styrene
ANN	Artificial Neuronal Network
ASR	Average Square Root
ATF	Acoustic Transfer Function
CAM	Center for Advanced Materials
CCLD	Constant Current Line Drive
DMA	Dynamic Mechanical Analysis
FE	Finite Element
FEM	Finite Element Model
FFT	Fast Fourier Transform
FRF	Frequency Response Function
GA	Genetic Algorithm
HDPE	High-Density Polyethylene
IPBC	Infinitely Periodic Bilayered Composites
IPMC	Infinitely Periodic Multilayered Composites
LDPE	Low Density Polyethylene
LRPC	Locally Resonant Photonic Crystal
MM	Mechanical Metamaterial
NPRP	National Priorities Research Program
PC material	Polycarbonate
PC	Phononic Crystal

PCB	Printed-Circuit-Board
PPCB	Phononic Piezoelectric Cantilever Beam
PTFE	Polytetrafluoroethylene
PVC	Polyvinyl chloride
RMS	Root-Mean-Square
SDOF	Single Degree-of-Freedom
SHPB	Split Hopkinson Pressure Bar
SMP	Shape Memory Polymer
UHMW	Ultra High Molecular Weight
UHMWPE	Ultra-High-Molecular-Weight Polyethylene
VEH	Vibration Energy Harvesting

LIST OF SYMBOLS

u	Displacement
σ	Stress
T_p	Transfer Matrix
ω	Angular frequency
$tr(T_p)$	Trace of the Transfer Matrix
ρ	Density
d	Thickness
a_3	Lattice constant
$c_{p,j}$	Pressure wave
$c_{s,j}$	Shear wave
E	Modulus of elasticity
E’	Storage modulus
E”	Loss modulus
E_∞	Elastic equilibrium modulus
n	Number of cells
r	Radius
$a_1,$	Aluminum layer
d	Lattice constant
T	Total thickness
W	Total width of the plate
w_z	Width of the zigzag opening
H	Total height of the plate

h_z	Height of the zigzag opening
$\hat{\varepsilon}_R(x_0, \omega)$	Rightward traveling wave
$\hat{\varepsilon}_L(x_0, \omega)$	Leftward traveling wave
x_0	Random reference point in the bar
$\kappa_{bar}(\omega)$	Propagation coefficient of the SHPB bar
$\hat{E}(\omega)$	Bar material complex modulus
$\hat{\varepsilon}_{inc}$	Incident wave
$\hat{\varepsilon}_{ref}$	Reflected wave
α	Pressure wave
β	Shear wave
J_0 , J_1	Bessel functions of the first kind
$\hat{\varepsilon}_{inc}(\omega)$,	FFT of the incident signal
$\hat{\varepsilon}_{tra}(\omega)$	FFT of the transmitted signal
ρ	Density
s	Cross section area
$C_t(\omega)$	Wave transmission coefficient
T_c	Chirp signal time duration
B_c	Linear frequency bandwidth
f_c	Signal starting frequency
k_c	Linear rate of the frequency change

CHAPTER 1: INTRODUCTION

Energy absorption, vibration control, and acoustic shielding are highly sought after in construction, aerospace, and automotive applications. Mechanical metamaterials (MMs) incorporating metallic and viscoelastic constituents hold great promise for their potential applications in infrastructure monitoring and even shielding structures from earthquakes. Despite the fascinating concept of MMs, practical products of MMs have not appeared yet, and will not appear in the immediate future due to several challenges. To illustrate, one of the most challenging obstacles for practical vibration control is that elastic band gap materials made of conventional structural materials (e.g., metals) possess typically narrow spectral band gaps in some high-frequency ranges (i.e., beyond hundreds of kHz). However, undesirable vibrations/noises disturbing the human body are characterized by broadband frequency content in a rather low-frequency regime (commonly only up to a few kHz). Thus, in order to bring down band gap frequencies to acceptable practical ranges, the use of viscoelastic materials becomes inevitable. Numerical studies based on linear viscoelasticity theory clearly show that band gaps are widened and placed in a lower frequency range when viscoelastic materials (e.g., elastomers) are employed as one of the MM constituents. However, a recent study of nonlinear elastic PCs reports that the nonlinearity driven by finite displacements allows some higher harmonic waves to penetrate band gaps, which can adversely affect the attenuation properties of PCs subjected to finite-amplitude displacement excitation. Thus, there is an urgent need to experimentally and numerically investigate the amplitude-dependent attenuation properties of viscoelastic MMs subjected to finite-amplitude excitations. There is a further need to assess their effectiveness for realistic applications, whose loading conditions are typically represented by broadband frequency content and a multitude of finite-

amplitude excitations.

1.1 Background

One of the most critical challenges in practice is the realization that MMs which possess low-frequency band gaps (< 10 kHz) strongly affect the human body. For example, the frequency band gaps of typical PCs are of the order of c/a, where c is a wave speed in a media, and a is the lattice constant related to the length-scale of a lattice structure. Thus, for the matrix (i.e., host of PCs) made of conventional structural materials like metals, the band gap structures for low frequencies that affect the human body would require impractical meter-scale macrostructures. The microstructure of smaller scales (e.g., millimeter-scale or smaller scales) can only be achieved by employing compliant matrix materials having very low elastic modulus such as elastomers (i.e., polymer with viscoelasticity). Alternatively, local resonance independent of microstructural periodicity is also combined with PCs in order to overcome the limitations associated with metallic PCs. Typically, the local resonance is brought into PC matrices by introducing elastomer-coated metal inclusions. For instance, Liu et al. [1] have experimentally observed that the acoustic frequency band gaps were as low as 400 Hz using elastomer-coated lead spheres embedded in an epoxy matrix.

Furthermore, due to the strong energy absorption properties of some viscoelastic materials (e.g., polyurea), the consideration given to practical applications such as vibration isolation and noise reduction naturally leads to the idea of employing elastomers in the matrix of PCs. However, viscoelastic materials have not been considered effective for creating PCs due to their inherent damping property, and it was only recently that researchers started actively working on the numerical investigation of wave propagation in PCs made of dissipative media.

1.2 Motivation

Phononic crystals and locally resonant materials require close consideration both experimentally and numerically for them to be applied in practice. The elastic bilayered materials composed of only metals show a very high-frequency attenuation, thus, to achieve low-frequency attenuation, a large dimension would be required. The use of viscoelastic materials paired with metals overrides this problem due to the wave propagation impedance mismatch between them. However, another problem arises because the inherent damping of the viscoelastic material affects the dispersion relation of the crystal. Thus, viscoelasticity also has been shown to induce deviation in the dispersion relation of viscoelastic composites.

The FE method has been used to model geometric and material nonlinearities, however, numerical analysis for vibration is impaired in the FEM by fictitious modes [2–4]. One solution to avoid the appearance of fictitious modes is to reduce the height of the crystal.

Thus, there is a need to experimentally and numerically investigate the attenuation properties of viscoelastic MMs subjected to finite-amplitude excitations. Scientists must assess their effectiveness for realistic applications (e.g., vibration isolation/control and impact energy absorption), whose loading conditions are typically represented by broadband frequency content and a multitude of finite-amplitude excitations.

1.3 Objective

In this dissertation, phononic crystals are investigated vis-à-vis their attenuation proprieties when using viscoelastic constituents and inserts for their natural damping proprieties. The general objective of this study is to develop nonlinear MMs possessing energy-absorbing capability (i.e., impact-resistant MMs), and investigate their characteristic effect on elastodynamic waves. This will provide a tool to assess

the attenuation characteristics of viscoelastic MMs with the distinct benefit of filling a knowledge gap. The following points summarize the main objectives of this study:

- ✓ Identify amplitude-dependent low transmission frequency zone performance (i.e., attenuation characteristics) of MMs.
- ✓ Determine the Dispersion Relation of various bilayered crystals using the transfer matrix method.
- ✓ Simulate the behavior of viscoelastic phononic crystals numerically using the FE method.
- ✓ Assemble an electrodynamic shaker setup for testing in the structure laboratory.
- ✓ Develop metal and polymer SHPB equipment for the structure laboratory.
- ✓ Assess the effectiveness of amplitude-dependent MMs subjected to practical and wide-ranging loading conditions represented by broadband frequency content and a multitude of finite-amplitude excitations. Thus, to identify potential key factors by which their band gap performance can be improved and.
- ✓ Write multiobjective optimization algorithms that successfully generate optimal specimens whose low transmission zones can be validated numerically and experimentally for both 1D phononic crystals and 2D locally resonant materials.
- ✓ Utilize SHPB to measure the band gap performance of MMs experimentally at high impulse on a high-frequency range.

1.4 Dissertation Outline

In order to achieve these objectives, different numerical and experimental methods

are proposed. Since the dissertation focuses on the characterization and optimization of mechanical metamaterials, different aspects of the study are outlined in six chapters. Besides the Chapters related to the introduction and conclusion, the content of the remaining four chapters is outlined in this section.

Chapter 2 is a literature review. In Chapter 3, an analytical investigation of the dispersion relation of phononic crystals using the transfer matrix method is presented. The analytical results are used to estimate specimen size and testing matrices used in the forthcoming chapters.

Chapter 4 presents a full procedure of multiobjective genetic algorithm optimization which generates a vibration attenuation optimal specimen whose low transmission zones can be validated numerically and experimentally. The chapter details the experimental procedure using the electrodynamic shaker, along with a numerical simulation of the viscoelastic phononic crystal that allows for the polymer's viscoelastic nature.

Chapter 5 summarizes an optimization study on 2D locally resonant materials achieved by enhancing thin plate vibration attenuation through introducing zigzag inserts with various geometries and tip masses. Multiple parameters are optimized with the main focus on the practical application on real-life structures.

Chapter 6 describes the development of the experimental facility for large-amplitude excitation SHPB and impact testing. Elastic and viscoelastic SHPBs are used to test a 1D phononic crystal, and the setup is modified to include a hybrid system with an aluminum input bar and a nylon output bar. The aim is to apply a large impact load to the specimen without much wave dissipation using the aluminum bar and to read the weak transmitted signal with the nylon output bar in an effort to adapt the SHPB apparatus to Mechanical Metamaterial testing.

CHAPTER 2: LITERATURE REVIEW

2.1 Phononic crystals (PCs)

A decade ago, Liu et al. [1] conducted pioneering experiments on a composite structure, which significantly affects acoustic transmission in a narrow frequency band. Since then, there has been a growing interest in the field of mechanical metamaterials (MMs) [5–7]. These are identified as artificial materials engineered to have unconventional mechanical properties stemming from their microstructural geometry rather than from their chemical composition. It is well known that much research has reported predominantly on the numerical aspect of phononic crystals (PCs) made of periodic structures designed to control the mechanical waves through Bragg scattering [8–11]. Research has also been reported on locally-resonant materials (LRMs) having the added feature of local resonances [12,13], and cloak materials characterized by transformation-based cloaking/waveguide features [14–16]. Potential applications of MMs can range from vibration control [17], noise reduction [18], to waveguide endeavors [19].

Despite the fascinating concept of MMs, practical products of MMs have not appeared yet, and may not appear in the immediate future due to several challenges. To illustrate, one of the most challenging obstacles for practical vibration control is that elastic band gap materials made of conventional structural materials (e.g., metals) possess typically narrow spectral band gaps in some high-frequency ranges (i.e., beyond hundreds of kHz or higher). However, unwanted vibrations/noises disturbing the human body are characterized by broadband frequency content in a rather low-frequency regime (20 kHz and less). To bring down band gap frequencies to acceptable ranges, the use of viscoelastic materials becomes inevitable. Numerical studies based on linear viscoelasticity theory clearly show that band gaps are widened

and placed in a lower frequency range when viscoelastic materials (e.g., elastomers) are employed as one of the MM constituents [20–24]. However, a recent study on nonlinear elastic PCs reports that the nonlinearity driven by finite displacements allows some higher harmonic waves to penetrate band gaps [25], which can adversely affect the attenuation properties of PCs subjected to finite-amplitude displacement excitation.

2.2 Investigation methods

2.2.1 Analytical Studies

Many studies have investigated the analytical dispersion relation for wave propagation perpendicular to the layers of elastic, infinitely periodic, bilayered composites (IPBC) [26–28] and infinitely periodic, multilayered composites (IPMC) [29–31] . Several investigations [32–34] have also been conducted on the analytical dispersion relations of the sagittal wave in IPBC. Other studies [35–37] have focused on the dispersion relation of oblique wave propagation in IPMCs. Due to the complexity of the formulation in the aforementioned studies, few studies have presented a generalized formulation for the analytical dispersion relation in multilayered composites [38].

In order to reach low-frequency range attenuation, polymeric materials have been used as a constituent of composites due to the existing impedance mismatch between them and metals. Note that polymeric materials are viscoelastic in nature. Researchers have considered the viscoelasticity of these polymers since their damping attenuation affects the overall periodic composite vibration attenuation. For instance, Tanaka and Kon-No [39] used the polymer complex moduli to compute the dispersion relation of viscoelastic-elastic layered composites. Other numerical methods to determine the complex dispersion relation of viscoelastic composites are: the transfer matrix method [40], the finite element method [41], the finite difference method [42], the Fourier

expansion method [43], the variational method [42], and the plane wave expansion method [24].

2.2.2 Numerical Studies

Researchers studying wave propagation in periodic composites have also used numerical techniques. These include the plane wave expansion method [24], the finite difference method [42], the continuum power series method [44,45], the effective stiffness method [46–48], the mixture theory [49–51], the variational method [52,53] and the finite element method [2,54,55]. The FEM Is the most used method due to the ease of use, the possibility of modeling multilayered composites, and the seamless modeling of nonlinear geometries and materials [55–59].

2.2.3 Experimental Studies

In order to experimentally characterize a phononic crystal wave attenuation behavior, vibration shakers, transducers, and impact testing are used. In this section, a literature review on these methods is presented.

2.2.3.1 Small Amplitude Experiments using shaker

One-Dimensional Crystals

Case 1 (Mass-Spring System)

A periodic mass-spring system was created by Wen et al. [60] to determine the band gap property of a crystal. A set of round copper and aluminum plates was connected by springs within a guiding pole system as shown in Figure 1. The crystal was excited along its vertical direction by a vibrometer (VE 5000) derived by a signal analyzer B&K 3650. For the excitation signal in the frequency range 0-2kHz, the response was obtained by the accelerometer (B&K 4507B) at the base and top of the crystal. A comparison of the two signals presents the attenuation characteristics of the crystal. The crystal was analyzed for the loaded and unloaded condition. In both cases,

attenuation of the wave was found at frequencies 60-125 Hz (Figure 2).

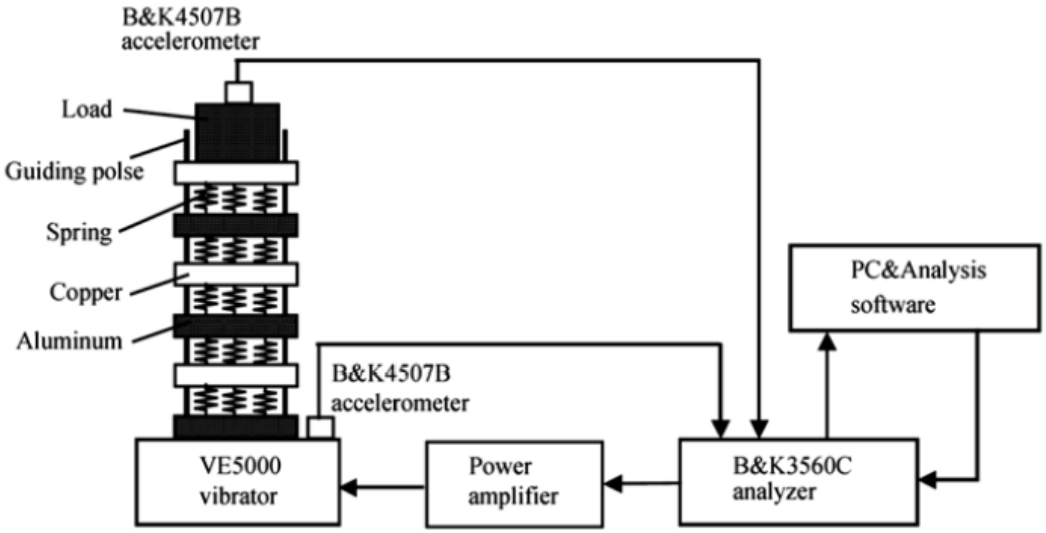

Figure 1. Schematics of Experiment Setup by Wen et al. [60]

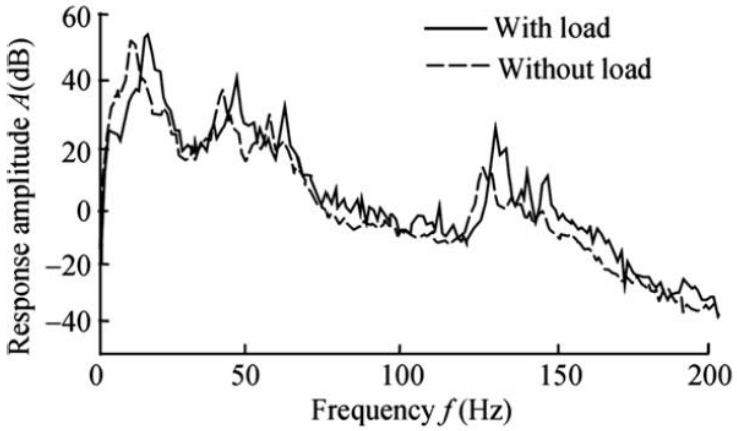

Figure 2. Wave Transmission Property of Mass-Spring Crystal Wen et al. [60]

Case 2 (Copper -Silicone rubber)

Another one-dimensional phononic crystal was experimentally investigated by Wang et al. [61] . Only the longitudinal wave was applied to the specimen made of copper and silicone rubber material through a vibration exciter. The diameter and length of each plate were 25 mm and 20 mm respectively, which gave a 120 mm long specimen overall. A force sensor was used for measuring the applied force of the vibration, and an accelerometer was used for determining the dynamic response. The result was

obtained for a low-frequency range of 0 – 2 kHz and a definite band gap frequency range was not observed. The reason was attributed to the viscoelastic damping property of the rubber material.

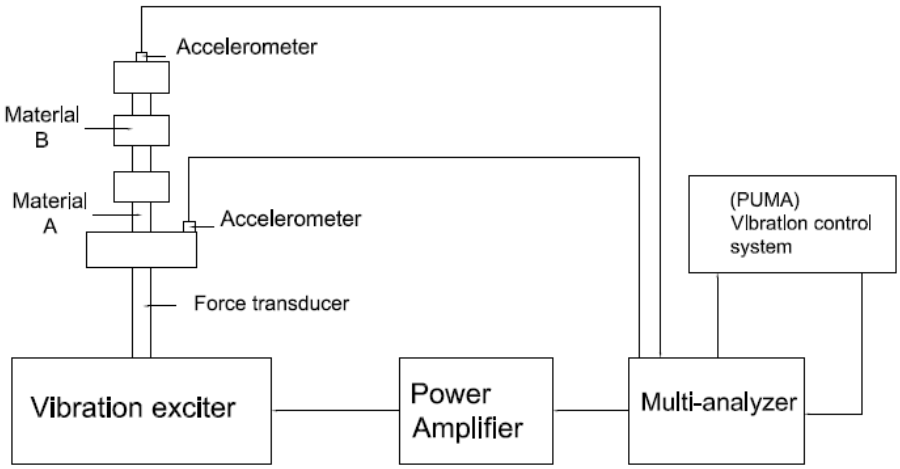

Figure 3. Schematic of Experiment Setup by Wang et al. [61]

Case 3 (Periodic Airfoil System)

The effect of fluid-structure interaction on the band gap property of a periodic airfoil was investigated by Casadei and Bertoldi [62]. Each unit cell was prepared by attaching an aluminum bender with acrylic flaps by superglue. Six-unit cells were connected to an aluminum beam to finally produce the periodic airfoil system. The total length of the airfoil was 300 mm.

The study showed that the band-structure property of the periodic airfoil was highly dependent on the airflow velocity. For the experiment shown in Figure 4, the periodic airfoil system was placed inside a wind tunnel by clamping one end and keeping free boundary conditions on the other. The velocity of the wind was varied to determine the evolution of the band gap. Moreover, two different lengths of the bender were used for the experiment to obtain the tunable property of the system. The K2025E013 electrodynamic shaker was used to excite the clamped end of the airfoil through a load cell (208C01 PCB Piezotronics). Two accelerometers (352C22 PCB Piezotronics)

were placed at two ends of the airfoil to determine the input and output responses. The transmission coefficient obtained from the ratio of accelerometer responses shows the band gap shifting behavior for different air velocities and bender lengths as demonstrated in Figure 5.

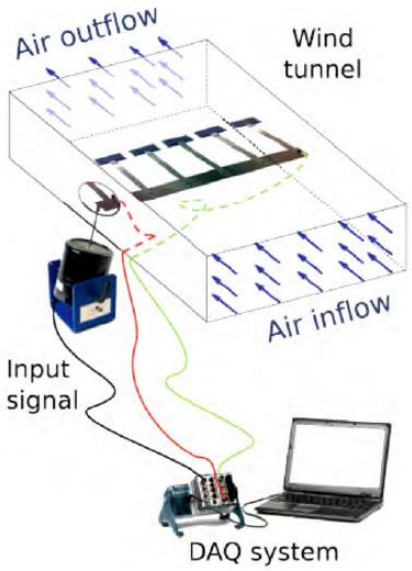

Figure 4. Experiment Setup for Periodic Airfoil System by Casadei and Bertoldi [62]

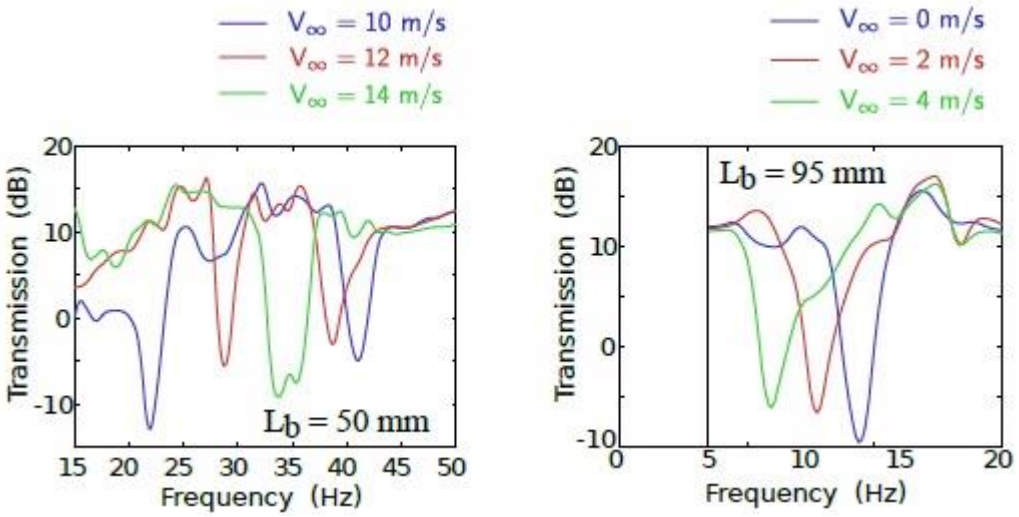

Figure 5. Evolution of Band gap Property of Periodic Airfoil System for Different Bender length and Airflow Velocity [62]

Case 4 (1-D Waveguide)

The attenuation property of the flexural wave in the 1-D waveguide (length = 3 m) was determined by Domadiya et al. [63] using two types of periodic beam system.

The steel and aluminum beams were experimented on by suspending them from both ends. The excitation system was composed of a suspended mini shaker which was attached to the beams by a stinger to apply a linear sweep between 100 to 6000 Hz. By suspending the entire system as shown in Figure 6, it was possible to generate purely flexural waves without any longitudinal or torsional modes.

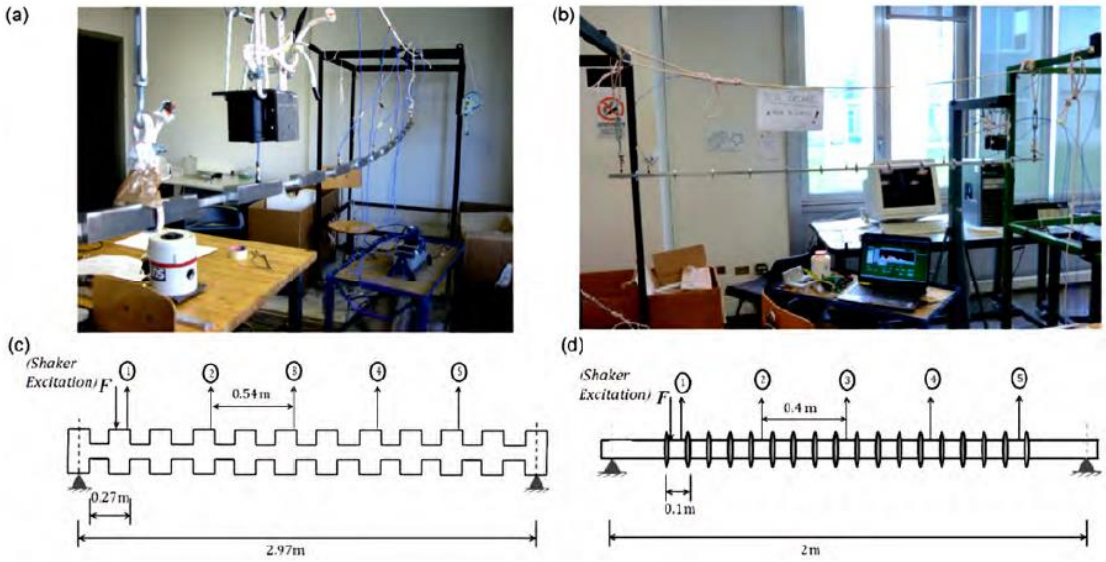

Figure 6. Experimental Setup of 1-D Waveguide [63]

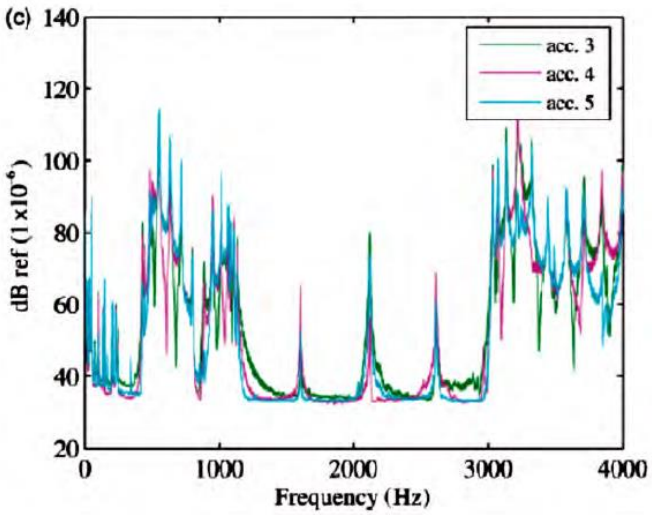

Figure 7. Acceleration-Power Spectra Obtained from Different Accelerometers [63]

The shaker produced a linear sweep in the frequency range of 100-6000 Hz. The acceleration response of the system was obtained through use of accelerometers at five different locations. The acceleration power spectra of the experiment are shown

in Figure 7.

Case 5 (Elastic/ Viscoelastic Layers)

For a composite pipe made of a periodic repetition of steel and rubber, Wen et al. [64] performed a vibration experiment to determine the attenuation property of the pipe. They used two different specimen settings for this test. In one case, they used three-unit cells in the specimen, while the other case included six-unit cells. In each of the cases, the length of the unit cell length was 1.27 m (a_{steel} = 1.05m, a_{rubber} = 0.22m).

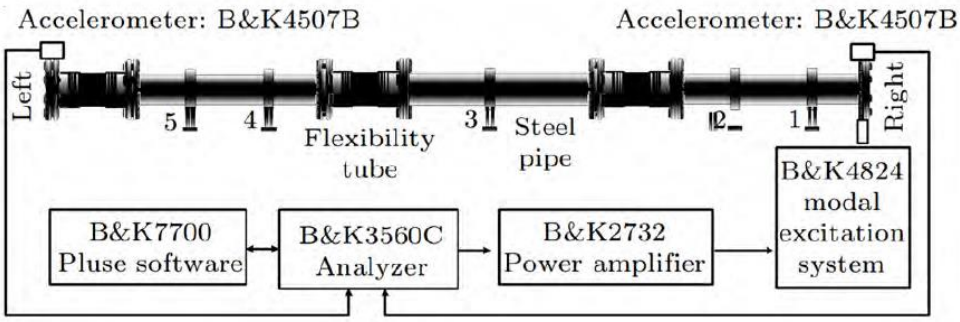

Figure 8. Experimental Setup for Pipe System from Wen et al. [64]

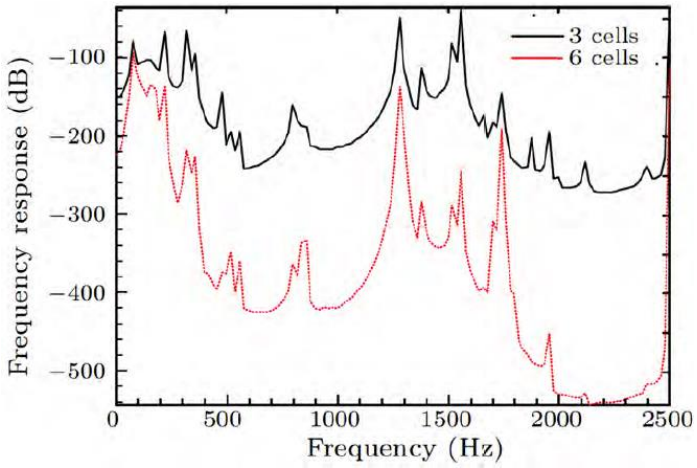

Figure 9. Frequency Response for Pipe with 3 and 6 Unit Cells, Wen et al. [64]

The pipe system was excited using a force transducer. A white noise signal between bandwidths 0.0-3.2 kHz was sent to this transducer using a vibration shaker (B&K Modal Exciter - 4824) as shown in Figure 8. The vibration generated a flexural wave in the pipe, and its response was measured on two ends for obtaining the input and

output spectral responses. The attenuation of the signal was obtained by comparing the spectral result of the two accelerators. It was found that the pipe had two distinct band gaps at frequency ranges 0.45-1.68 kHz and 1.78-2.45 kHz for both specimens (See Figure 9).

Case 6 (Piezoelectric cantilever beams)

Chen et al. [65] have researched broadband vibration energy harvesting using the piezoelectric effect. Their research widened the resonant bandwidth of a piezoelectric harvester using one-dimension PPCBs (Phononic piezoelectric cantilever beams). First, they calculated and analyzed the band gap. Then they conducted a parametric study by use of numerical and finite element simulations. The proposed method was validated by experimental tests.(Figure 10)

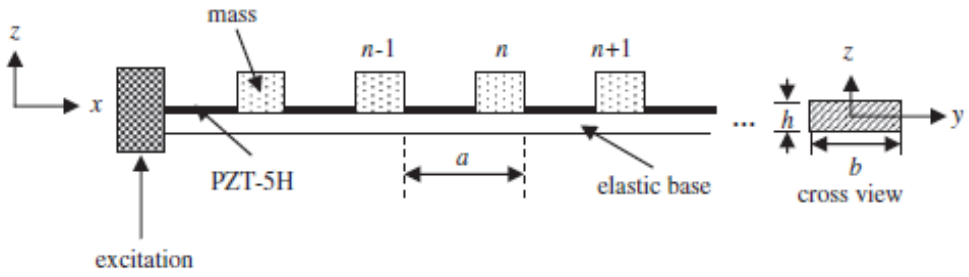

Figure 10. Diagram of a one-dimensional PPCB [65]

The main focus of their research was to introduce PCs into the VEH field. The broad bandwidth of a piezoelectric cantilever beam could be achieved by resorting to band gaps.

Table 1. Testing results under different masses (m)

m	0.002 kg	0.004 kg	0.006 kg	0.008 kg	0.010 kg
Band gap (Hz)	74.8	80.6	84.4	88.2	92.7
Center frequency (Hz)	134.1	127.2	123.1	121.2	116.1
ASR of voltage (V)	5.0467	5.8797	6.0354	6.1347	6.02596

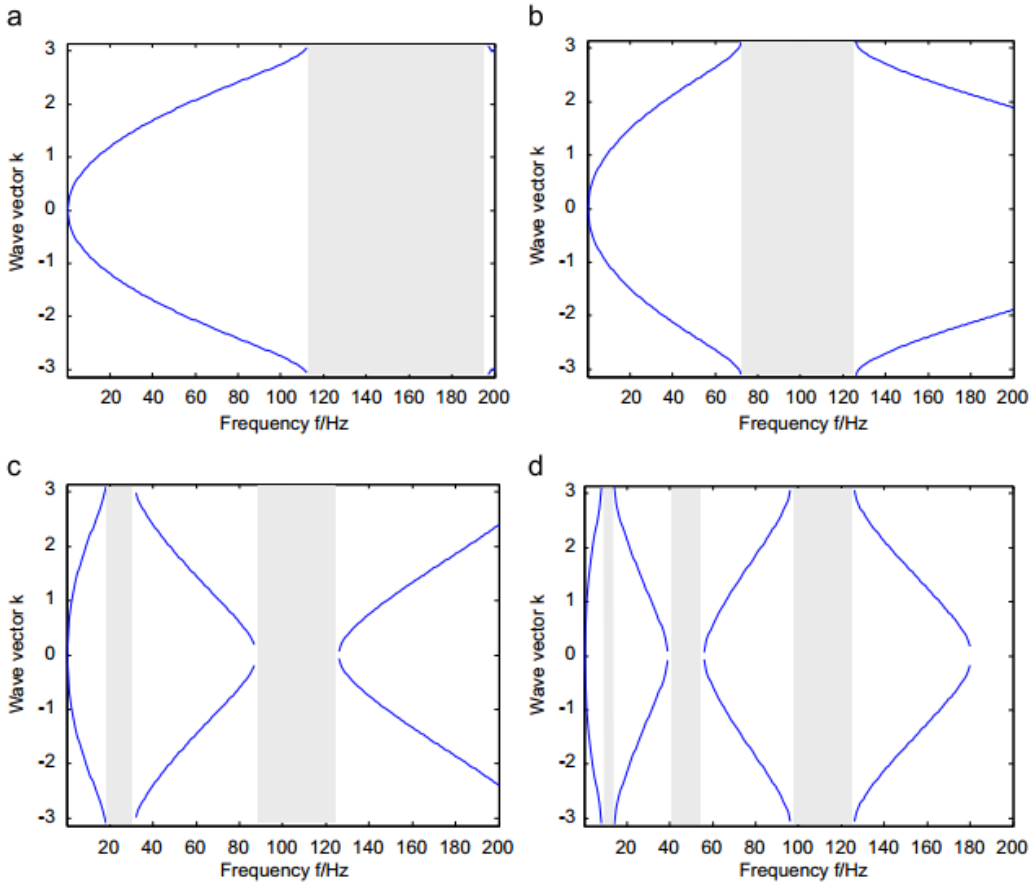

Figure 11. Vibration band gaps under different amplitudes (a) a=0.08m, (b) a=0.1m, (c) a=0.2m and (d) a=0.3m [65]

The correlation between vibration band gaps and the amplitude is presented in Figure 11. There was a direct correlation between the number of band gaps and the input vibration amplitude. By increasing the amplitude, the band gap would move to a lower frequency and the bandwidth would decrease. Table 1 shows the test results for the center frequency, the band gap, and the ASR for the voltage for different masses.

Two-Dimensional Crystals

Case 1 (Tunable Pattern Transformation)

Shan et al. [66] studied the effect of tuning of a 2-D phononic crystal on the elastic band gap. They used a highly tunable soft PC (initial lattice constant 10 mm and dimension 200 mm × 240 mm) and determined the band gaps at different deformed shapes by both FEM and experiments. Figure 12 shows the numerical and

experimental results of the pattern transformation of the PC due to a different angle of loading.

Using an electrodynamic shaker (model K2025E013), the vibration was applied to the specimen for finding the phononic band gap of the PC (Figure 13). An amplifier was used to generate a Gaussian white noise. A uniform in-plane wave was guaranteed using a PTFE block which guaranteed a proper contact surface between shaker and sample. The response of the crystal resulting from the vibration was captured using the miniature accelerometer (352C22 PCB Piezotronics). This response was compared with the input force signal obtained from the load cell.

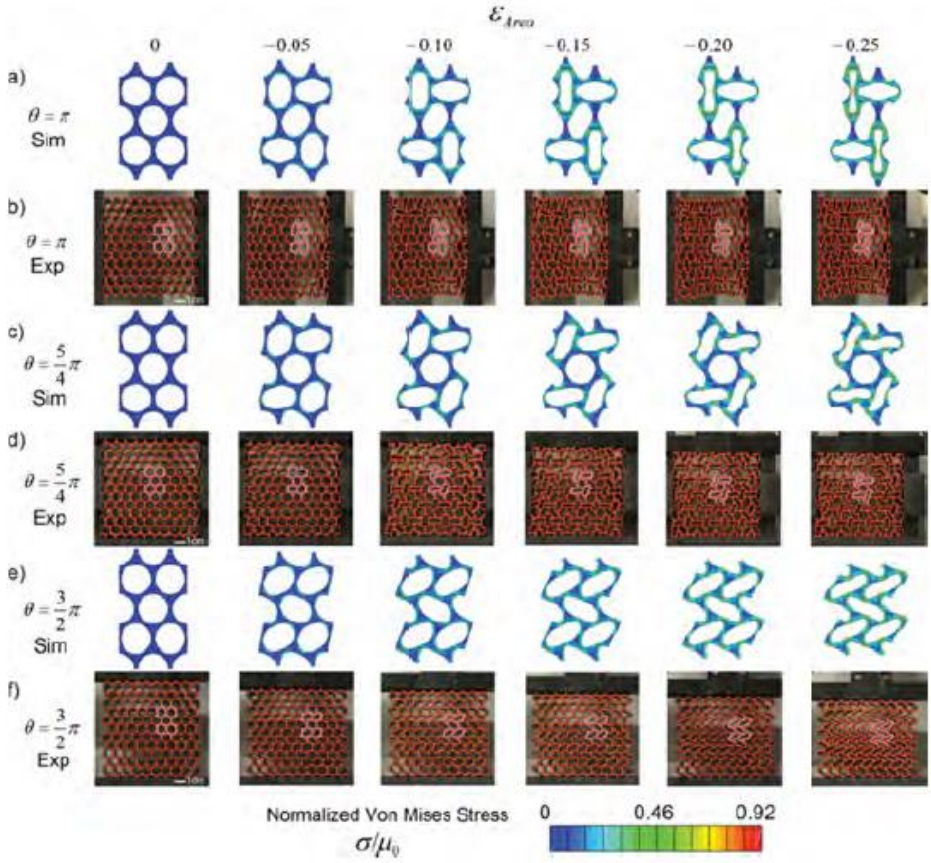

Figure 12. Different Deformed Shapes of Tunable Phononic Crystals Shan et al. [66]

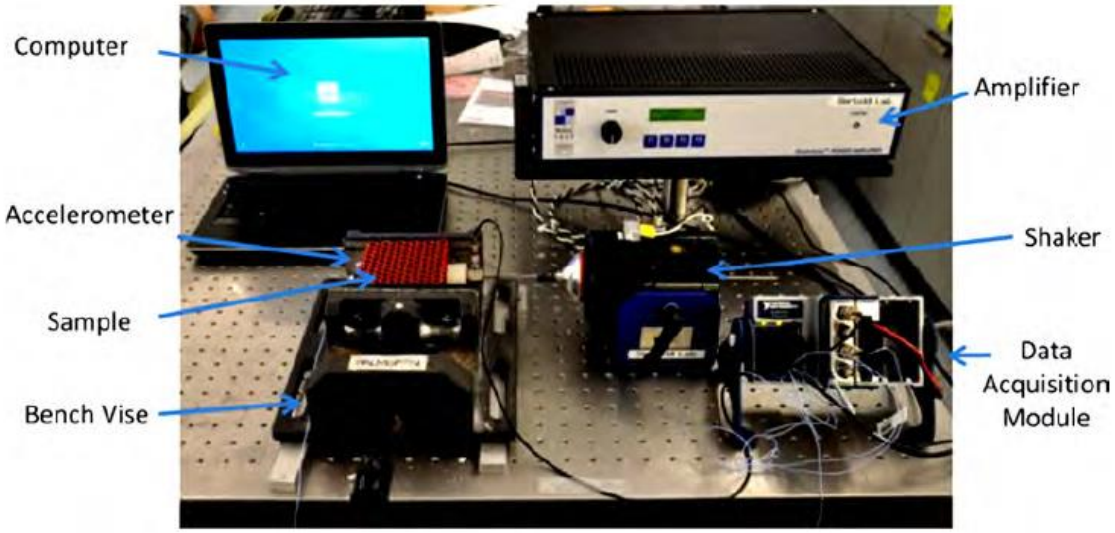

Figure 13. Experimental Setup by Shan et al. [66] for determining the band gap

The parameter set for obtaining a quantitative response was the ratio of the output acceleration signal to the input force signal. Figure 14 shows the band gap results at the non-deformed and different deformed shapes of the PC obtained numerically and experimentally.

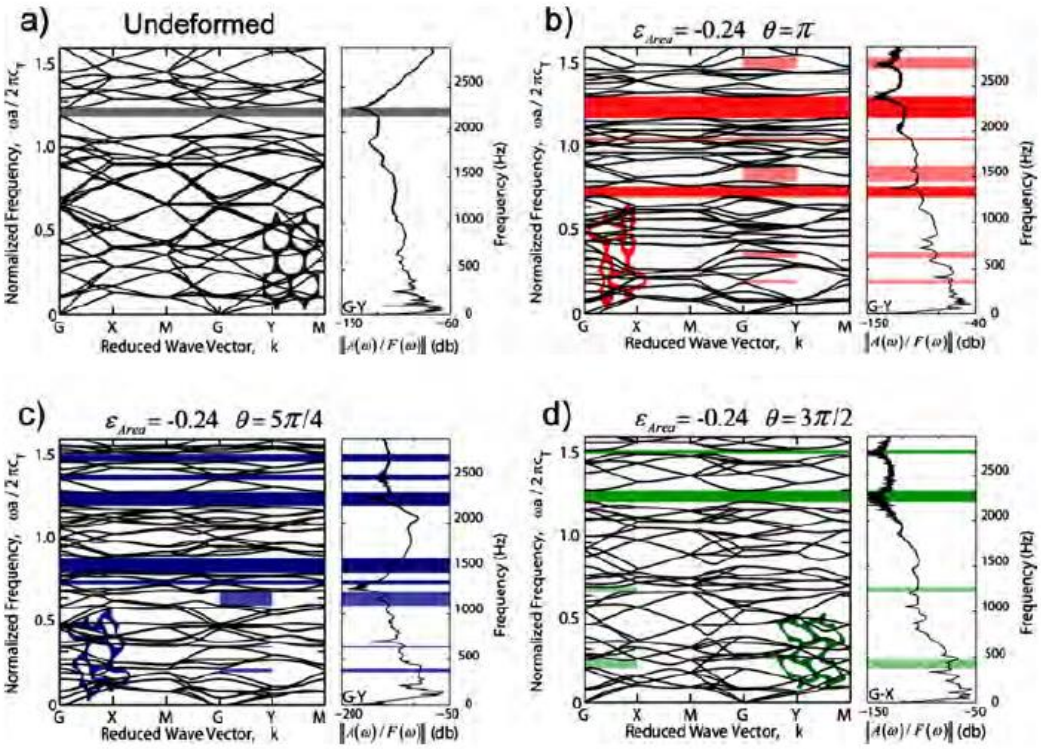

Figure 14. FEM (left) and Experimental (Right) Phononic Band gap [66]

Case 2 (Phononic Crystal Plate)

The frequency band gap of a phononic crystal plate with scatter was experimentally obtained by He and Jin [67]. Round steel (4 mm thick) and silicone rubber (5 mm thick) scatters of 40 mm diameter were placed in a square array pattern on an aluminum plate acting as the matrix (1 m×0.8 m×0.5 m). The lattice constant of each unit cell was 50 mm, and the overall size of the crystal was 0.75m×0.25m. The entire matrix was suspended by rubber rope to replicate free boundary conditions as shown in Figure 15. The experimental instruments are shown in Table 2.

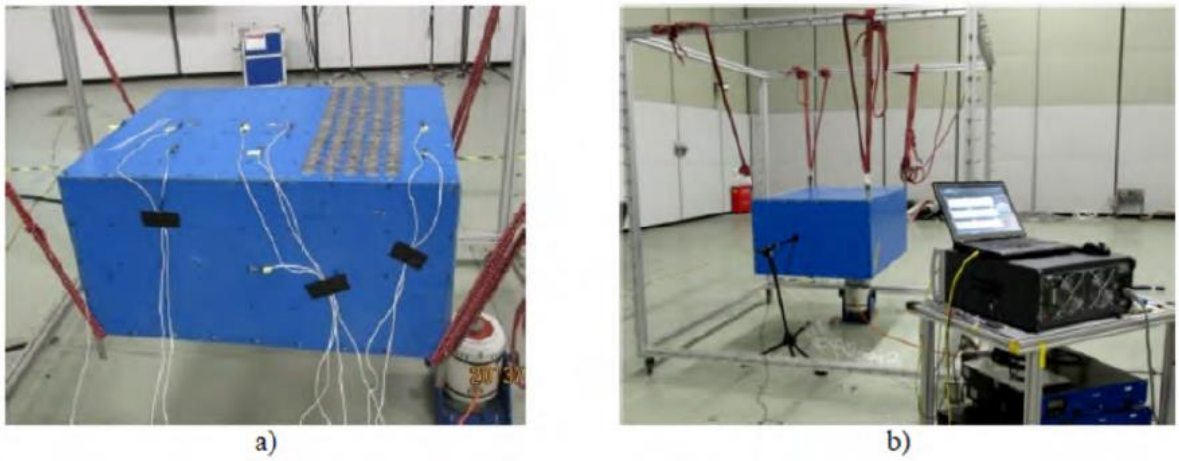

Figure 15. Experimental Setup for Aluminum Plate with Scatter [67]

Table 2. Experimental Instrument [67]

Item No.	Name	Model No.	Supplier
1	Signal generation module	LMS SCADASIII	LMS
2	Power amplifier	BAA120	TIRA, Germany
3	Exciter		TIRA, Germany
4	Force sensors		PCB, USA
5	Acceleration sensor	ICP	PCB, USA
6	Intelligent acquisition system	LMS SCADASIII	LMS
7	Software	Test lab 11A	LMS

A vibration exciter was used to apply vertical excitation from the bottom of the suspended matrix. The white noise input signal from a signal generator was used for driving the exciter. The response of the crystal due to this excitation was measured by nine accelerators. The transmission spectra in Figure 16 show the response comparison of the matrix with and without the phononic crystal. The result shows that the use of a phononic crystal attenuates waves in the band gap frequency range.

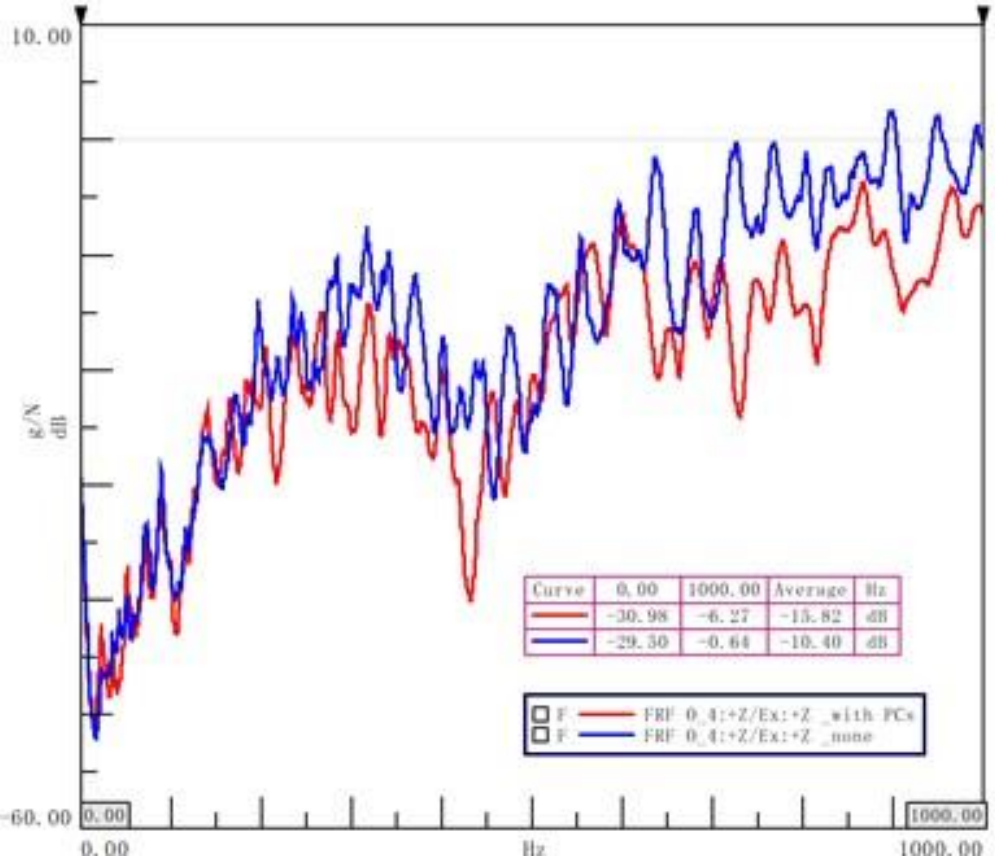

Figure 16. Wave Transmission Property of Aluminum Matrix with and without the Phononic Crystal [67]

Table 3 summarizes the keys features of the electrodynamic shaker experiments of metamaterials in the presented literature review.

Table 3. Summary of the listed experiments using an electrodynamic shaker

Subsection	Specimen Description	Specimen Dimension	Experiment Frequency Range (kHz)	Excitation System's Frequency (kHz)	Excitation System's Displacement	Receiver
1	Aluminum-Copper Mass-Spring		0.2	Vibrator (VE5000)		Accelerometer (B&K 4507B)
2	Copper - Silicone Layered	120 mm	2.0	(Vibration exciter)		Accelerometer
3	Airfoil System	300 mm	0.05	(K2025E013 shaker) 9.0	16 mm	Accelerometers (352C22 PCB Piezotronics)
4	1-D Waveguide	3.00 m	6.0	Mini shaker		Accelerometer
5	Steel-Rubber Pipe	3.81m	3.2	5.0 (B&K Exciter: 4824)	25 mm	Accelerometer (B&K 4507B)
6	2-D Silicone Rubber with Air Hole	200×240 mm^2	3.0	9.0 (K2025E013 shaker)	16 mm	Accelerometers (352C22 PCB Piezotronics)
7	Crystal Plate	750×250 mm^2	1.0	20.0 (TIRA: TV 50018)	5 mm	Accelerometers (ICP PCB)

Case 3 (Triangular beam lattices)

Qi Jian Lim et al. [68] investigated the effect of hierarchy on the propagation of elastic waves in triangular beam lattices. They found that a structural hierarchy could be used to introduce an additional type of band gap other than the Bragg type and locally resonant band gaps which could provide a way to design lattice-based metamaterials possessing hybrid band gap properties.

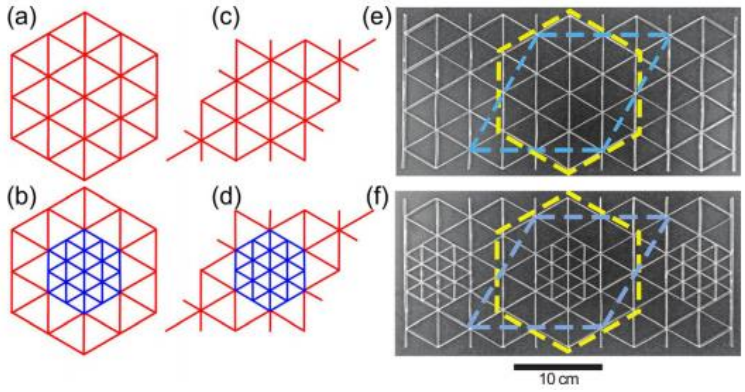

Figure 17. Triangular lattice structure with a different order of hierarchy

The researchers studied the propagation of small amplitude elastic waves in fractal-inspired beam lattices. This was first done numerically using the Finite Element (FE) commercial package Abaqus/Standard and then experimentally by use of an electrodynamic shaker (Brüel & Kjær - model LDS V406).The shaker was attached to the left edge, and the dynamic response was recorded using miniature piezoelectric accelerometers (DJB Instruments-model A/25/E) attached at both ends of the sample. The findings show that the position of this gap was fully predictable (it always occurs at X = 1), thus facilitating the design of systems that suit the engineering constraints.

Case 4 (resonating units scattered in an elastic matrix)

Pai Wang et al. [68] described a new class of tunable switchable acoustic metamaterials that consisted of resonating units scattered in an elastic matrix (Figure 18). The structure of this material was a metallic core connected to the elastomeric matrix through elastic beams. The buckling of the beams was exploited for the control of elastic wave propagation. The development of the locally resonant band gap was shown first by a numerical analysis, and the effect of nonlinear pre-deformation was fully studied . In the experimental front, He et al. [28] measured the transmission of vibration while changing the applied loading in a finite-size sample. This study proposed the concept of expanding the abilities of an acoustic metamaterial by

enabling tuning over a wide frequency range. The researchers demonstrated that deformation can be used for turning on and off the band gap and opening the way for adaptive switches design.

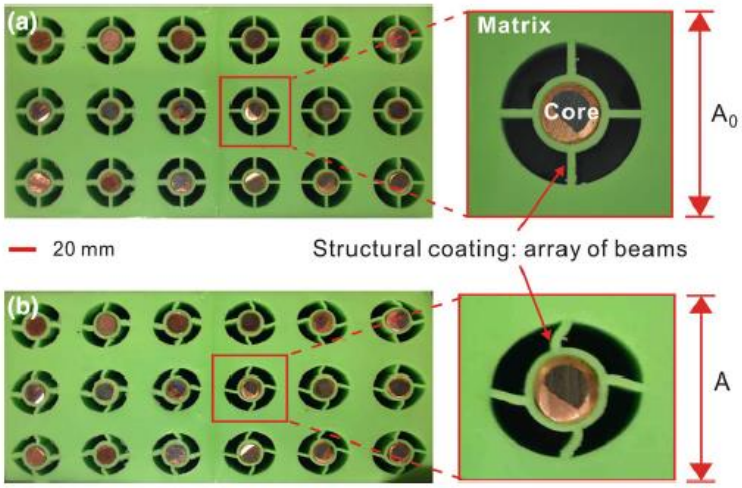

Figure 18. Tunable acoustic metamaterial [68]

Three-Dimensional Crystal

Case 1 (Sandwich panel)

Delpero et al. [69] presented a three-dimensional phononic crystal whose dispersion properties shows a large band gap starting from 2 kHz.. A sample of the crystal was used as a core of a sandwich panel to verify the presence of the band gap. The acoustic transmissibility between the two panel faces showed a large attenuation in this range of frequency. This study clarified the simplicity and reliability of the concept and permitted the finding of the reduction value. Other geometric configurations could be explored other than the one presented in order to shift the attenuation band to lower ranges (Figure 19).

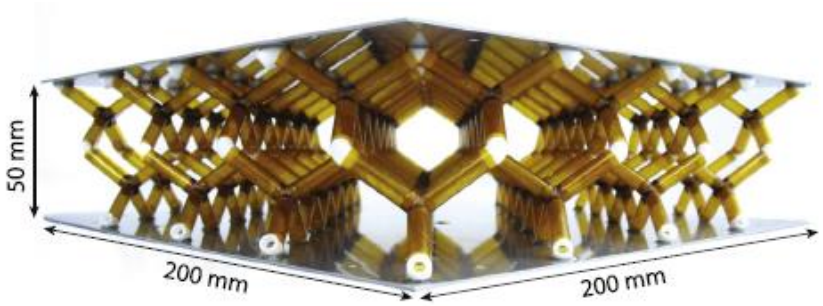

Figure 19. Sandwich panel with the phononic crystal core [69]

Case 2 (Cylindrical resonators distributed in soil)

Krödel et al. [70] designed a new civil "metastructure" to protect structures from seismic vibration through application of locally resonant metamaterials to decrease low-frequency waves. They validated their concept in a 1:30 scale system and suggested a full-scale resonator geometry that considered the construction constraint and using rubber bearings. The metastructures consisted of arrays of cylindrical tubes enclosing a resonator suspended by a soft bearing. Eigenvalues were used to obtain broadband attenuation characteristics (See Figure 20).

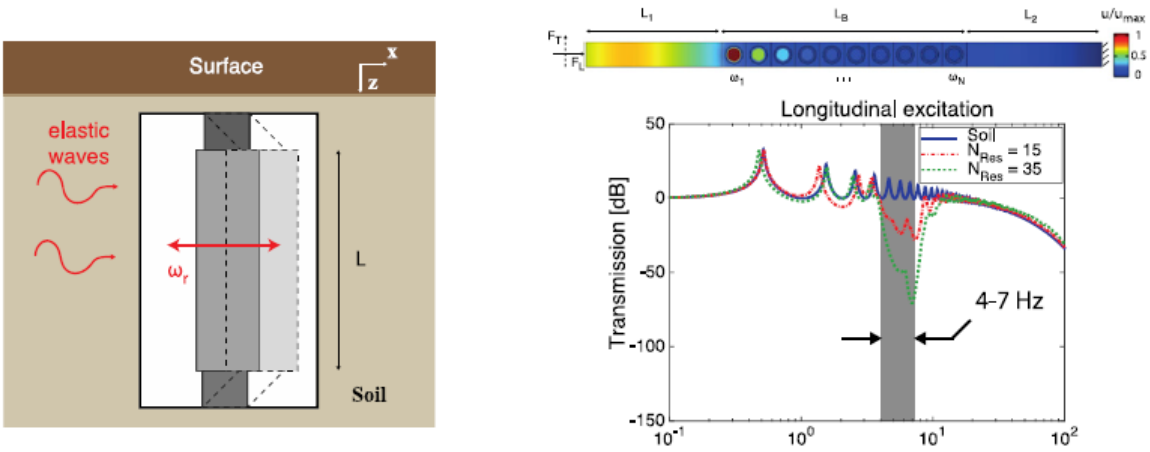

Figure 20. Components in a resonator, consisting of a cylindrical hollow tube containing a heavy bulk cylinder (left). Schematic diagram of a resonator array in our 2-D equivalent model with transmission spectrum (right) [70]

2.2.3.2 Small Amplitude Experiments using Transducers

One-Dimensional Crystal

Case 1 (Elastic-Elastic Layers)

There have been very few experimental studies conducted for determining band gap generated by the shear waves in a layered phononic crystal. One such was done by Robinson and Leppelmeier [71]. They combined multiple layers (0.002″) of steel and copper foils through diffusion bonding. The specimen parameters are shown in Table 4. In order to cover a wide range of frequency responses, two techniques were applied using quartz transducers. Responses for frequencies below 10 MHz were determined using the pulse-echo method, and those above 8 MHz were determined using the long-pulse method. Figure 21 shows a dispersion relation comparison and spectral results presented by this study.

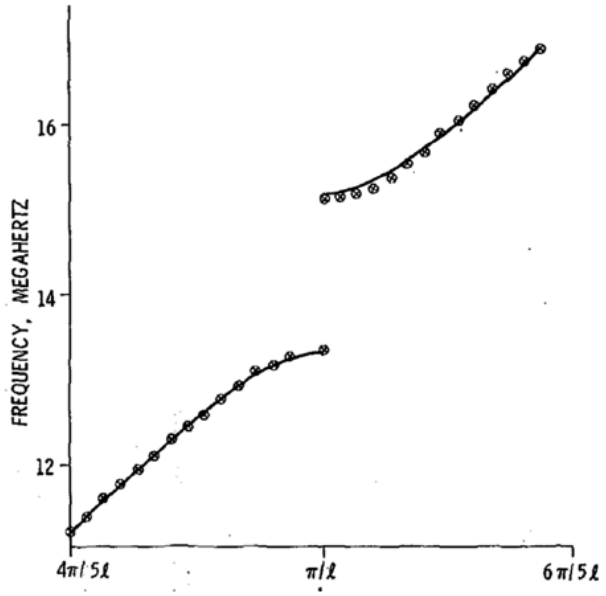

Figure 21. Analytical (Solid) and Experimental (Dot) Dispersion of 1st Shear Band gap [71]

Table 4. Specimen Description of Experiments by Robinson and Leppelmeier [71]

Materials	Layer thickness	Number of Cells	Overall Thickness
Steel and Copper	0.002” (0.05 mm)	75	0.15” (3.75 mm)

Case 2 (Elastic/Elastic and Elastic/Viscoelastic Layers)

One of the noteworthy experiments into the acoustic band gap of the one-dimensional multilayered composite was done by Hayashi et al. [72]. They used different combinations of steel, aluminum, copper, and PVC for finding the band gap of the multilayer composite samples shown in Figure 22.

Also, the combinations of different materials which were used in the specimens for this study are shown in Table 5. The main objective of the study was to characterize the imaginary wavenumber i.e., attenuation property of the samples. When the imaginary part of the complex wave number increases, i.e., attenuation rises, the band gap in the real part of the wavenumber takes place. Figure 23 shows the theoretical dispersion curve for both real and imaginary wave numbers for steel aluminum PC. Here, the band gap in the real wave vector was observed in the frequency range, where the imaginary wave vector appeared.

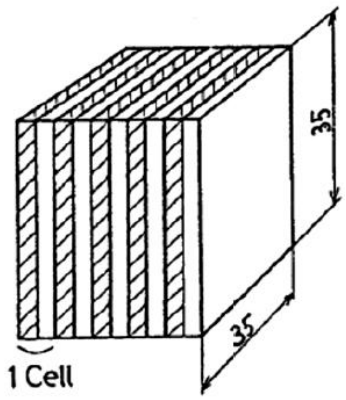

Figure 22. Sample Specimen from Hayashi et al. [72]

Table 5. Details of Specimen used in the Study of Hayashi et al. [72]

Materials	Thickness of Each Layer	Number of Cells	Overall Thickness
Steel and Aluminum	Steel 0.02” (0.5 mm) and Aluminum 0.02” (0.7 mm)	35	1.34” (35 mm)
Steel and Aluminum	Steel 0.027” (0.7 mm) and Aluminum 0.027” (0.7 mm)	20	1.1” (28 mm)
Steel and Copper	Steel 0.02” (0.5 mm) and Copper 0.02” (0.5 mm)	20	0.79” (20 mm)
Copper and Aluminum	Copper 0.027” (0.7 mm) and Aluminum 0.027” (0.7 mm)	20	1.1” (28 mm)
Steel and PVC	Steel 0.011” (0.3 mm) and PVC 0.011” (0.3 mm)	35	0.87” (22 mm)
Aluminum and PVC	Aluminum 0.011” (0.3 mm) and PVC 0.02” (0.5 mm)	35	1.1” (28 mm)

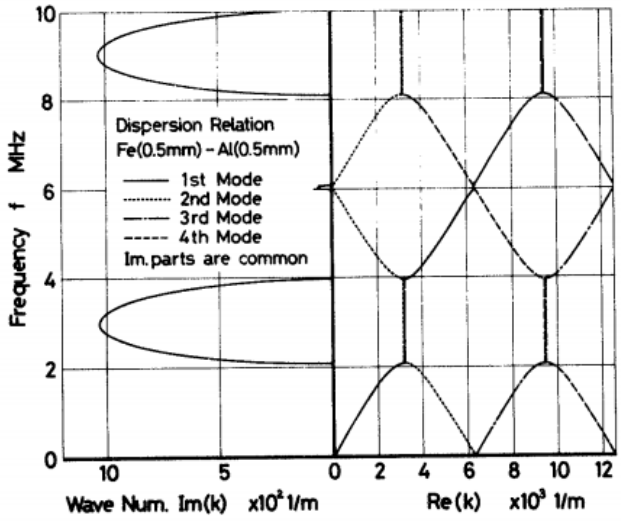

Figure 23. Dispersion Relationship of 1D Fe-Al Phononic Crystal [72]

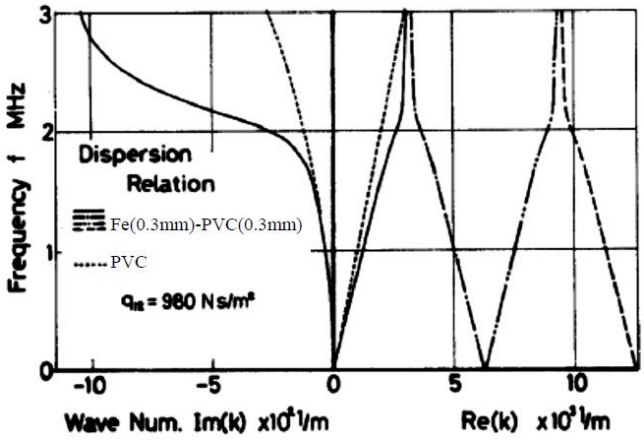

Figure 24. Attenuation Comparison of Steel-PVC and Steel-Aluminum [72]

The theoretical results for viscoelastic PVC itself, compared with a steel-PVC periodic specimen are shown in Figure 24. Here the frequency is plotted against both real and imaginary parts of the wave numbers. Until around 1.5 MHz, both the real and imaginary wave vector increases similarly. After that, the periodic specimen of Fe-PVC attenuated severely compared with the viscoelastic PVC. At the same time, the real wave vector of Fe-PVC started to open the band gap.

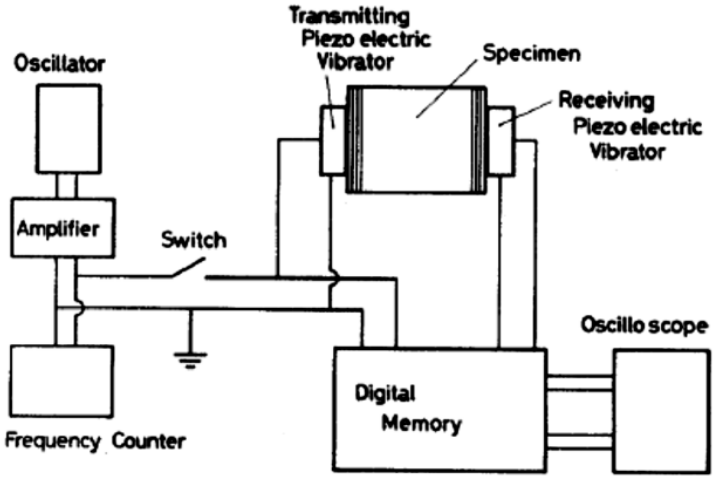

Figure 25. Schematics of Experimental Setup by Hayashi et al. [72]

For the experiment, a specimen was placed between a transmitting and receiving piezoelectric vibrator. The studies presented only the imaginary part of the wavenumber which defined the attenuations of the specimen. Figure 26 shows the frequency content of the attenuation for elastic/ elastic and elastic/viscoelastic specimens.

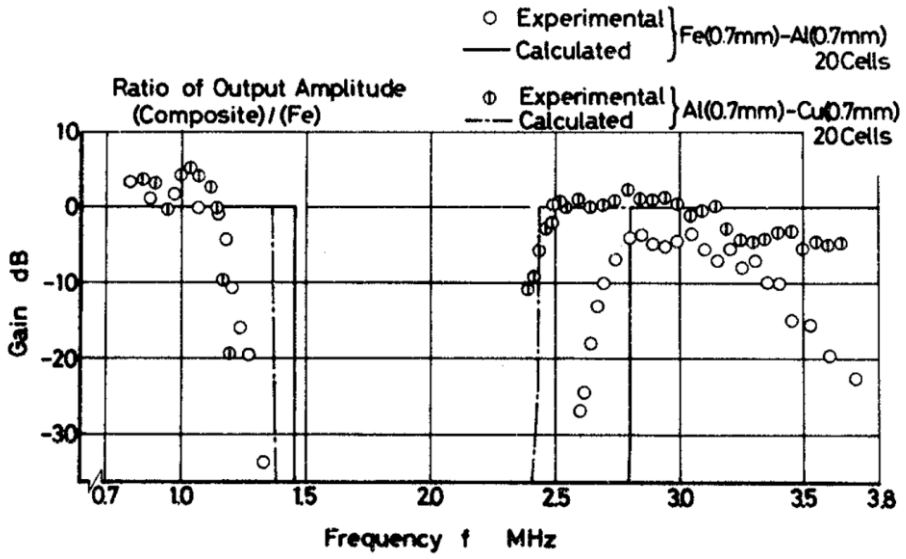

(A)

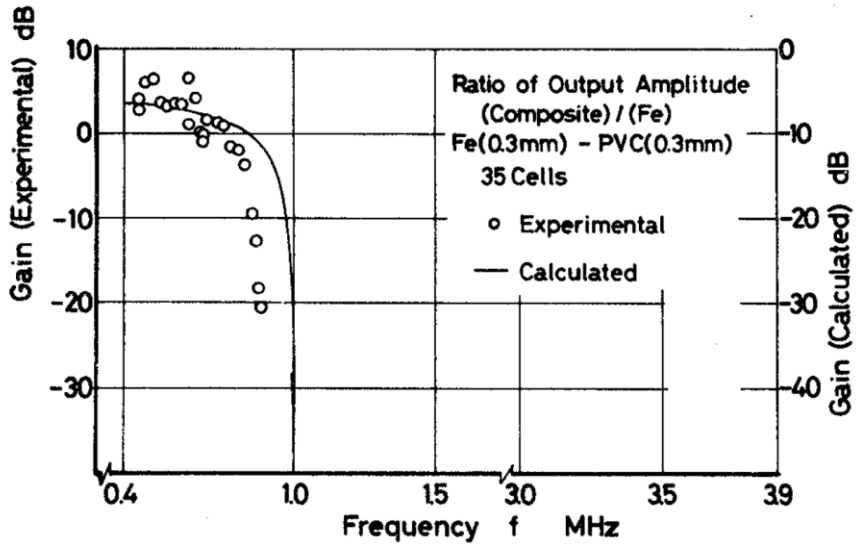

(B)

Figure 26. Attenuation of (a) Elastic/Elastic and (b) Elastic/Viscoelastic Samples [72]

Case 3 (Periodic Quartz Chain)

Periodically arranging a set of sixteen quartz cylinders on an L-shaped ladder, Meidani et al. [73] investigated the band gap property of the 1-D crystal. The cylindrical particles (radius 9 mm and height 18 mm) were alternately placed at a similar angle for the experiment to obtain a 290 mm long crystal. The crystal was attached to a piezoelectric actuator (Piezomechanik, model PSt 150/14/40VS20) on one side and a roller supported block of mass on another side. The actuator was fixed with a rigid wall, while the block of mass was attached to another wall through a spring. The experimental setup is shown in Figure 27a and Figure 27b.

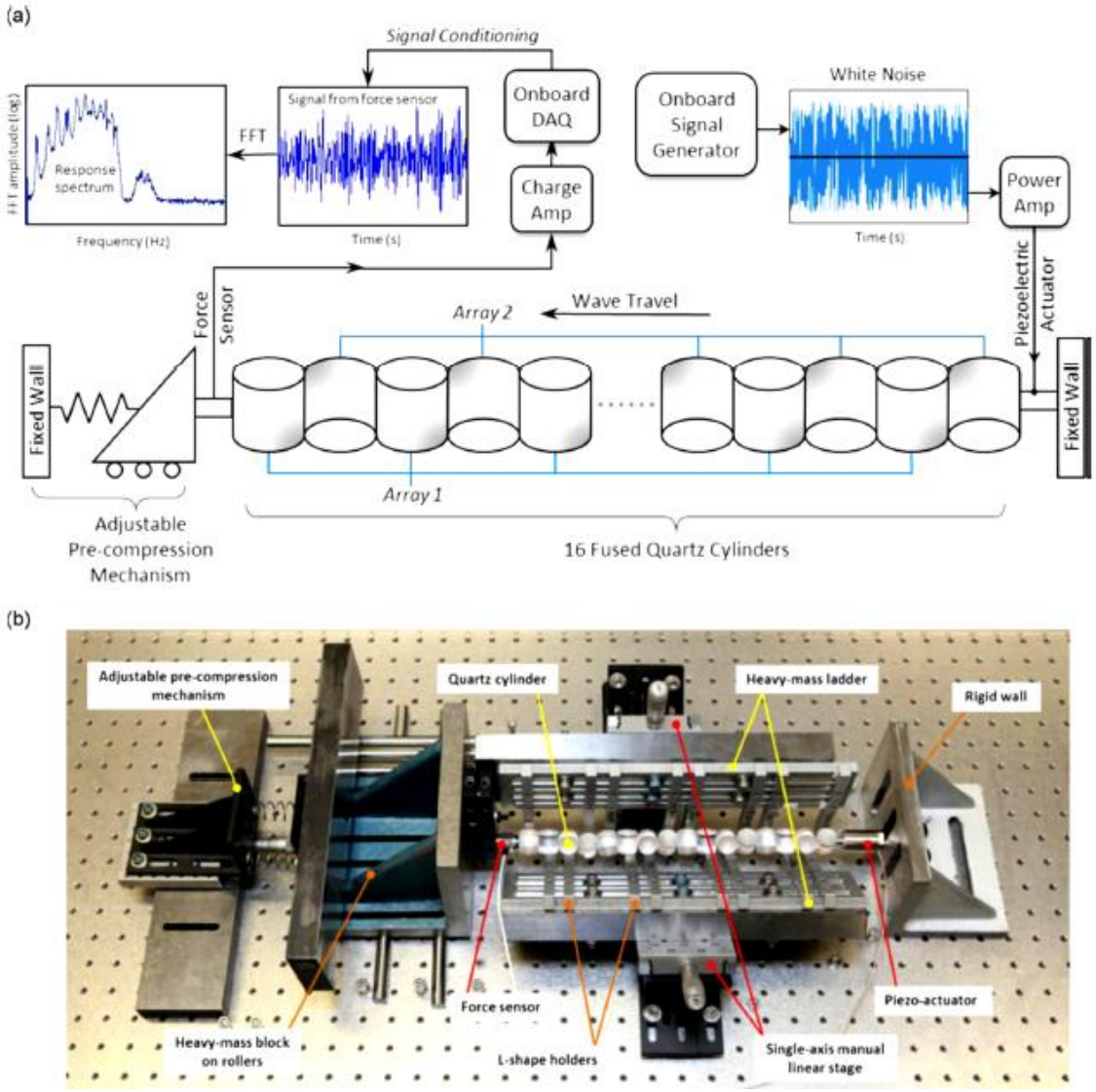

Figure 27. Experimental Setup of Quartz Chain Phononic Crystal [73]

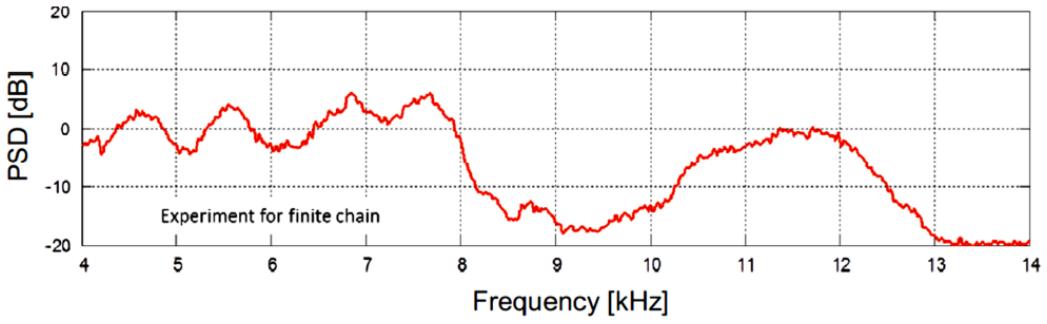

Figure 28. Experimentally Obtained Transmission Spectra of Quartz Chain Crystal [73]

A function generator was used to apply white noise excitation of the piezoelectric actuator. The quartz chain crystal response was measured by a force sensor (PCB, model 208-C01) which was fixed to a heavy-mass block. The transmission spectra from the experiment show a band gap between f = 8.0-11.0 kHz in Figure 28.

Case 4 (Elastic/ Viscoelastic Layers)

In another study, Martínez et al. [74] used a multilayer lead/epoxy sample with nylon to demonstrate the band gap in response to a longitudinal wave. Lead and epoxy layers were glued together Although the lead and epoxy were elastic in nature, nylon imparted the viscoelastic property in the experiment. The lead/epoxy specimen was placed between two semi-circles of nylon (Figure 29). The properties of the materials are shown in Table 6 and the specimen description in Table 7.

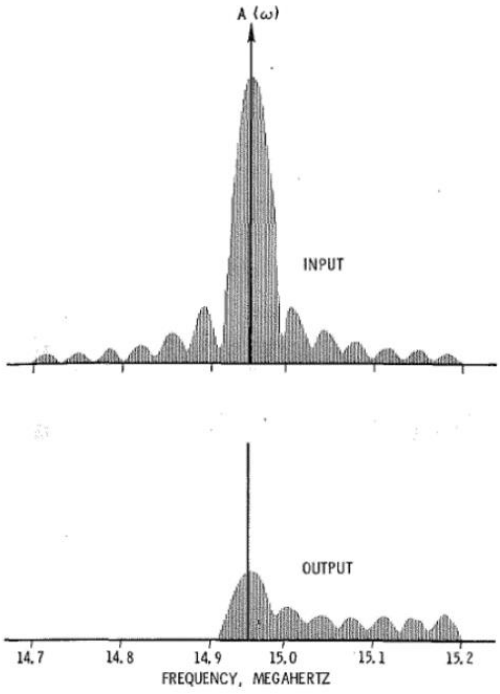

Figure 29. Sample Spectral Analysis of Input and Output Pulses [74]

Table 6. Properties of Materials in Experiments by Martínez et al. [74]

Material	ρ (kg m^{-3})	c_l (m s^{-1})	c_t (m s^{-1})
Pb	10760	1960	850
Epoxy	1140	2770	1300
Nylon	1110	2600	1100

Table 7. Specimen Description of Experiments by Martínez et al. [74]

Materials	Thickness of Each Layer	Number of Cells	Overall Thickness
Lead and Epoxy	0.04” (1 mm)	6	0.63” (16 mm)

The objective of their study was to determine the omnidirectional elastic band gap. This is defined as the band gap of the phononic crystal irrespective of the incident angle of the wave. In general, an omnidirectional lattice band gap is difficult to find. In Figure 30, both the sagittal and transverse planes did not share a common band gap. However, if a suitable medium could be used for the incidence and transmission of the wave on the PC, the omnidirectional band gap could be achieved. In the Martínez et al. [75] experiment, nylon semi-circles worked as the medium. If the longitudinal phase velocity of nylon is $C_{l,Ny}$, then only the region above the line $L_{l,Ny}$ ($=C_{l,Ny}K_x$) in Figure 30 can be incident on the PC of lead/epoxy. Therefore, between the frequencies 273-371 kHz (Dash line in Figure 30) a band gap could be found irrespective of the incident angle.

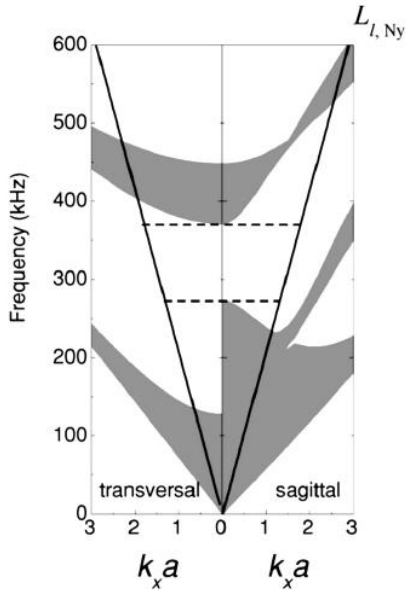

Figure 30. Omnidirectional Band gap (Horizontal Dash Lines) Obtained Using Viscoelastic Nylon Medium [74]

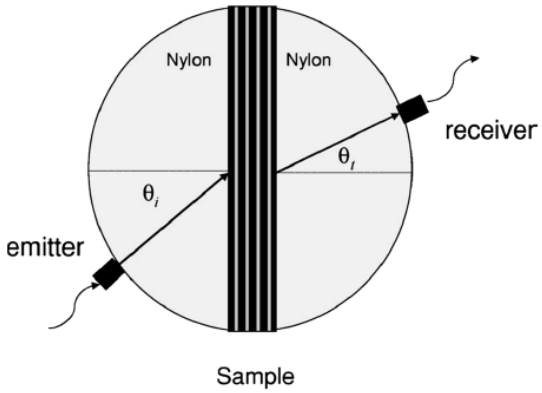

Figure 31. Schematic Experimental Setup from Martínez et al. [74]

Two ultrasonic wave pulsers and a receiver transducer were used in the experiment. The longitudinal wave was generated at one piece of nylon using a transducer (emitter), and the response was recorded on another transducer (receiver) which was placed on the second nylon piece. The schematic of the experiment is shown in Figure 31. The applied longitudinal wave underwent mode conversion while passing through the sample and resulted in two waves, longitudinal and transverse. The receiver could collect both the waves. Different pulsing and receiving angles were

used in this study.

The band gaps obtained from the experiments are shown in Figure 32.

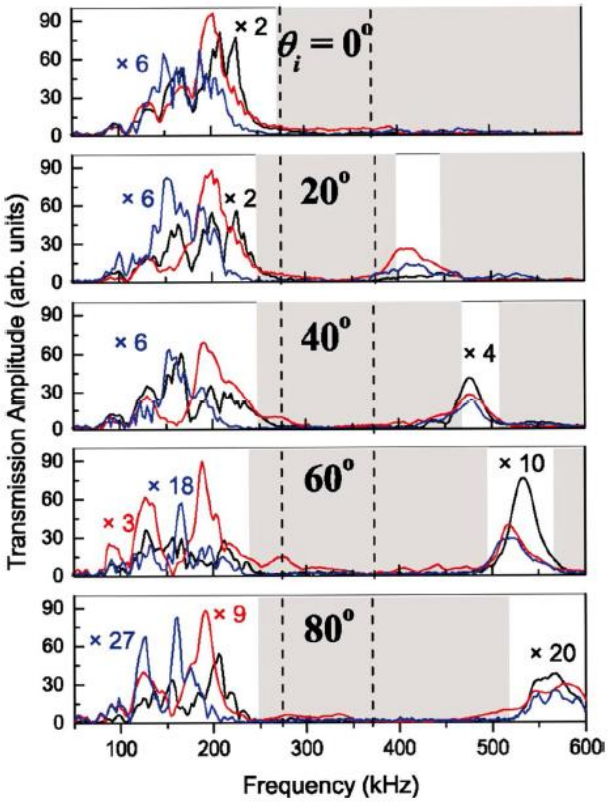

Figure 32. Frequency Content Showing Band gap in Study by Martínez et al. [74]

Two-Dimensional Crystal

Case 1 (Lead Coated by Rubber)

The research was performed on two-dimensional locally resonant phononic crystals by Yu et al. [75] on thin plates of a lead-epoxy composite (Figure 33). An 8×8-unit cell configuration was used for the plate. The two lead-epoxy combinations used were a 1 mm thick 100 mm×100 mm plastic plate with 64 circular holes containing 6mm thick square Pb blocks. As shown in Figure 33, the two combinations were as follows: (a) the Pb was coated on two sides by rubber and (b) the Pb was coated on all sides by rubber.

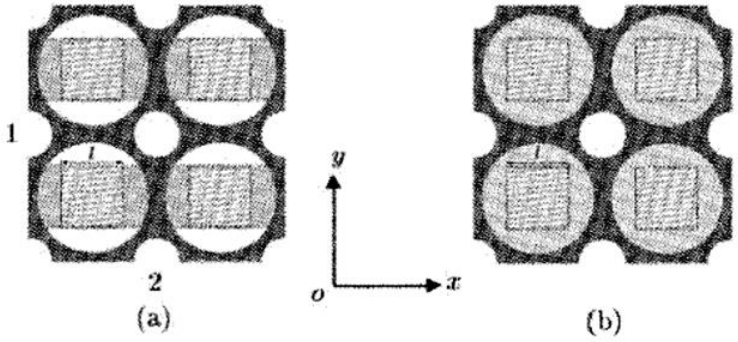

Figure 33. Locally Resonant Photonic Crystal (LRPC) Specimen by Yu et al. [75]

Using a white noise generator, the specimen was excited between 5 Hz to 3000 Hz. The transmitted vibration was measured with an accelerometer at the other side of the specimen. Then the transmission FRF (Frequency Response Function) was measured with B&K 4507 accelerometers. The obtained results were compared with a FEM study. Figure 34 shows the experimental frequency band gap between 950-2750 Hz due to the incident wave along the x-direction. The numerical result was found to be in good agreement with the experimental result.

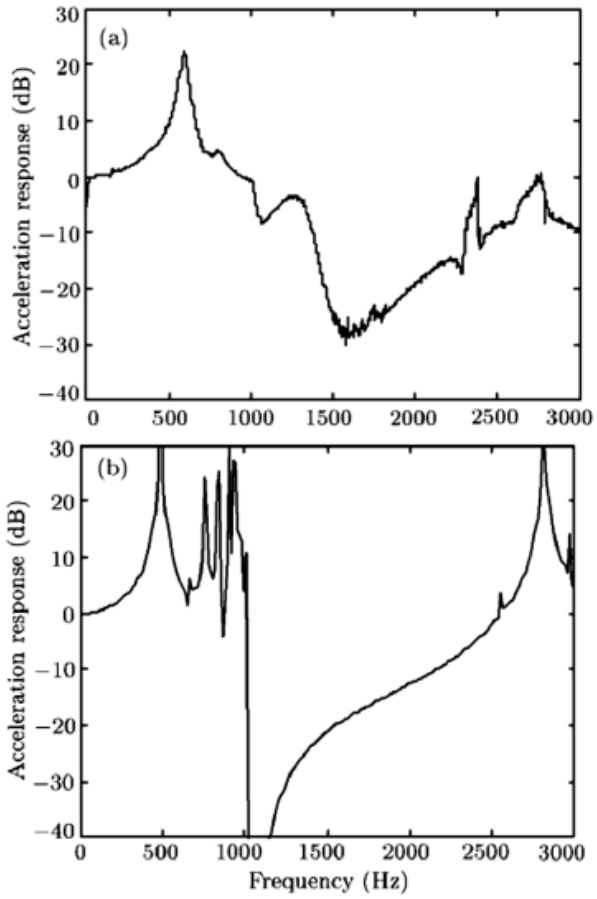

Figure 34. (a) Experimental and (b) Theoretical FRF for the Second Combination of LRPC Yu et al. [75]

Case 2 (Nylon with Air Hole)

The spectral property of a 2-D phononic crystal was investigated by Pachiu [76] to find the nonlinear dispersion effect. The crystal was prepared using SLS technology from nylon powder, where the square arrays of air cylinders gave rise to periodic properties. The experimental setup of the study shown in Figure 35 was a crystal (50mm×50mm) with a lattice constant of 3.9 mm.

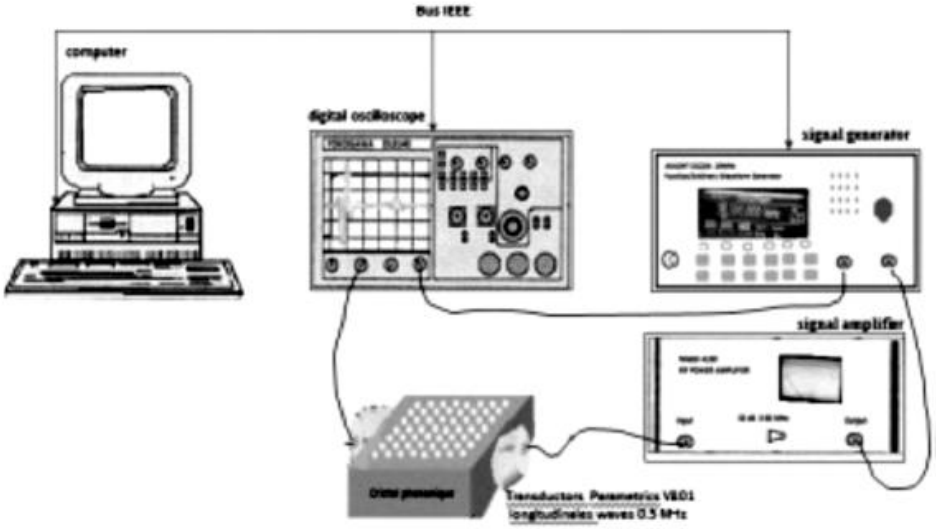

Figure 35. Experimental Setup of a 2-D Nylon Phononic Crystal with Square Array of Air Cylinders Pachiu [76]

A Panametrics V152 piezoelectric transducer (1 MHz central frequency) was used for both generating and receiving signals on two faces of the crystal. Figure 36 shows that the second harmonic generation of the signal was found in the experiment. Because, if an input signal with central frequency f belonged to a band gap zone, a transmitted signal was found at 2f. The authors attributed this phenomenon to the granular structure of the nylon powder.

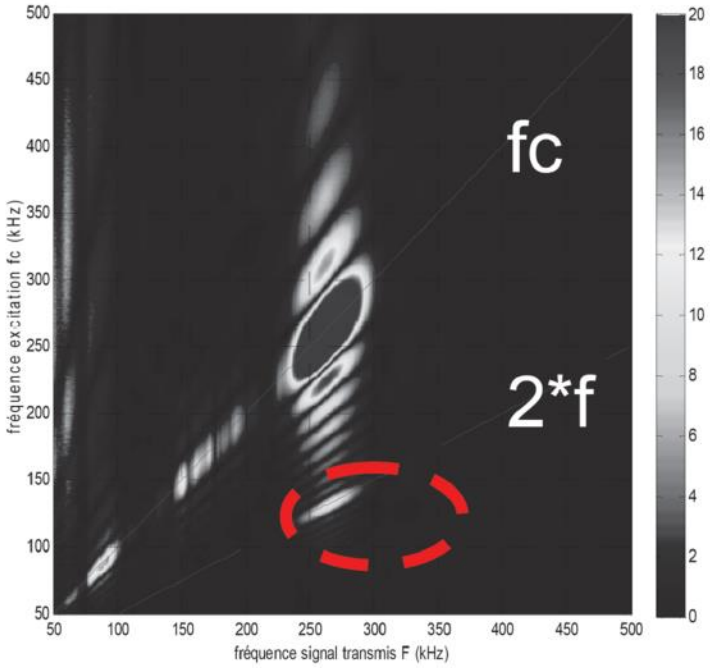

Figure 36. Second Harmonic Generation Results for a 2-D Phononic Crystal Pachiu [76]

Case 3 (Hexagonal Aluminum Cell)

A wavefield reconstruction of the elastic wave using a two-dimensional PC was performed by Celli and Gonella [77]. The laser vibrometry technique was applied for the detection of in-plane and out of plane movements at different nodes of the crystal. A hexagonal lattice structure made of aluminum with unit cell dimensions of 31.2 cm×30 cm was used for the study. A total of 20×18 similar unit cells was combined to obtain the crystal. The crystal was clamped at the bottom and loaded at the top using a transducer as shown in

Figure 37(b). A total of 5 cycles of sinusoidal bursts modulated by a Hann-window was used as a forcing signal.

The response of the crystal was determined by a 3D Laser Doppler Vibrometer (3D-SLDV). This vibrometer system used three scanning heads (

Figure 37(a)) which also contained rotating mirrors. The mirrors directed the laser beam to each patch. The PSV software was used for combining the three laser beams by video triangulation options. In this way, 100 readings were taken at each selected node on the vibrometer. The velocity-time histories at all grid points were used for reconstructing the wavefield on the entire crystal.

In the post-processing phase, displacement was determined from the velocity readings, and color maps were obtained by interpolating the snapshots at each point. An FE model was created for simulating the experiment. Figure 38 presents one of the comparisons of the numerical and experimental results from the study by Celli and Gonella [77].

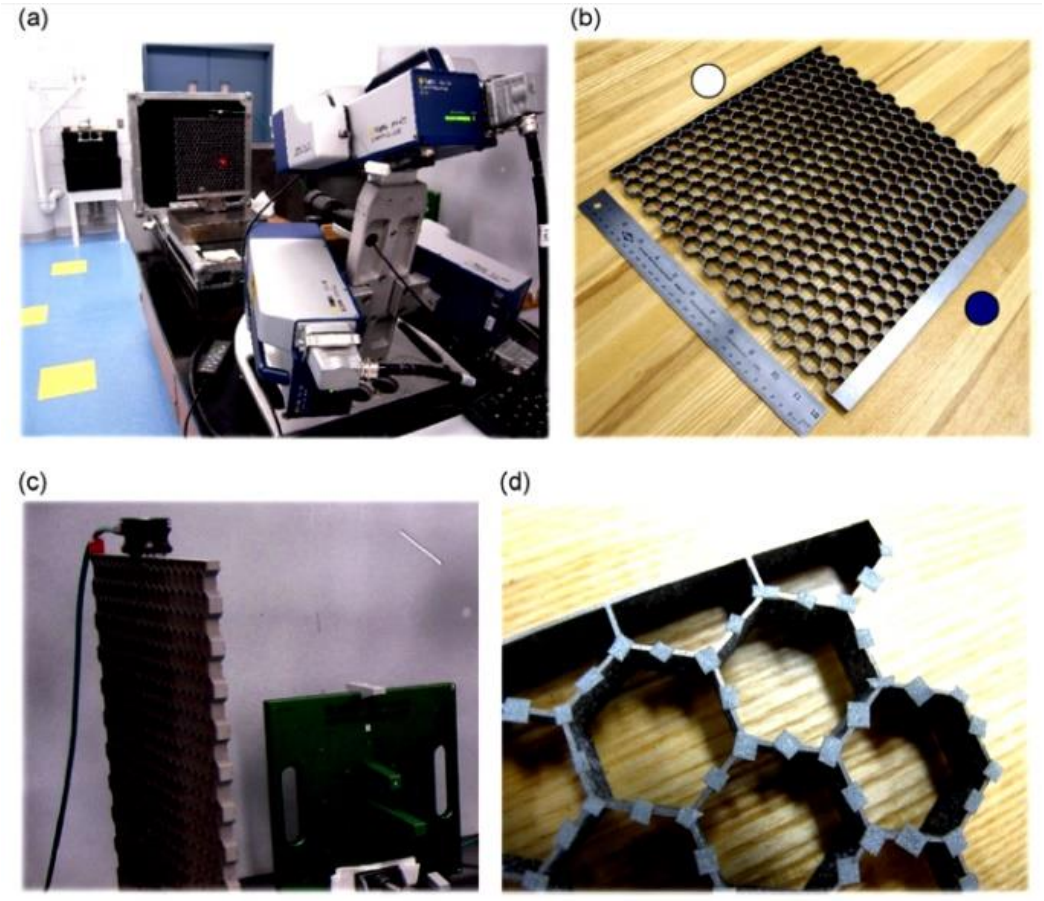

Figure 37. (a) Experimental Setup (b) The White Circle Showing the Loading Location and Blue Circle Showing Clamping Location (c) Detail of Transducer

Location (d) Reflective Tape Patches on Different Nodes of the Crystal [77]

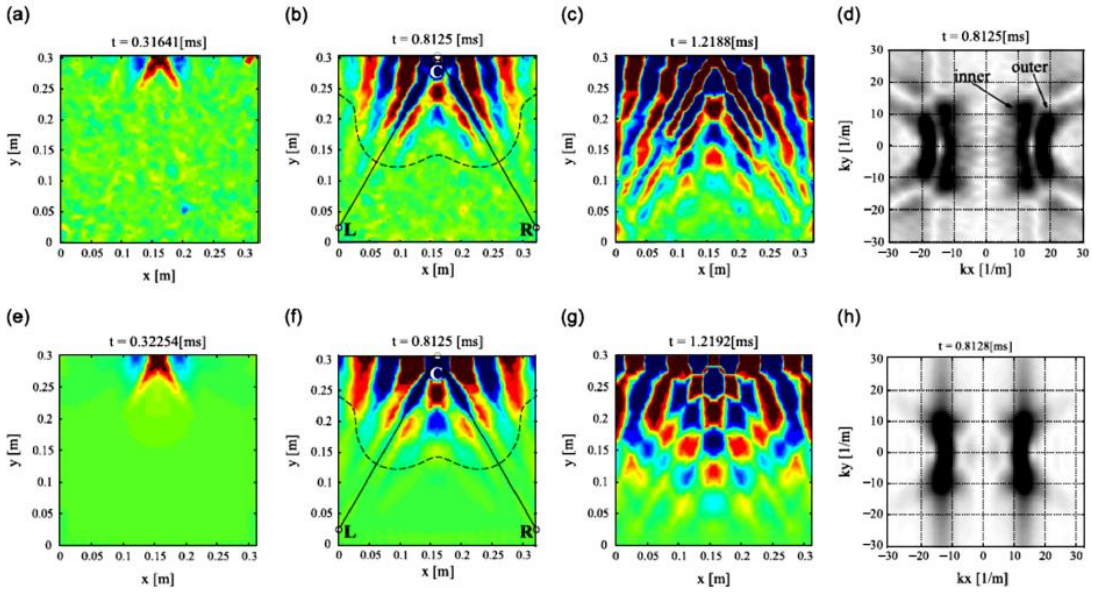

Figure 38. Comparison of Experimental (a-d) and Numerical (e-h) Wavefields [77]

Case 4 (High-Q filters)

Topology optimization of a waveguide-cavity structure in phononic crystals for designing narrowband filters under given operating frequencies was presented in the Dong et al. study [78]. The cavity typology was optimized to have high symmetric resonance; thus, this crystal could be used as a filter. The optimization of the cavity in 2D PnCs was made by perforating holes in the elastic matrix. (Figure 39)

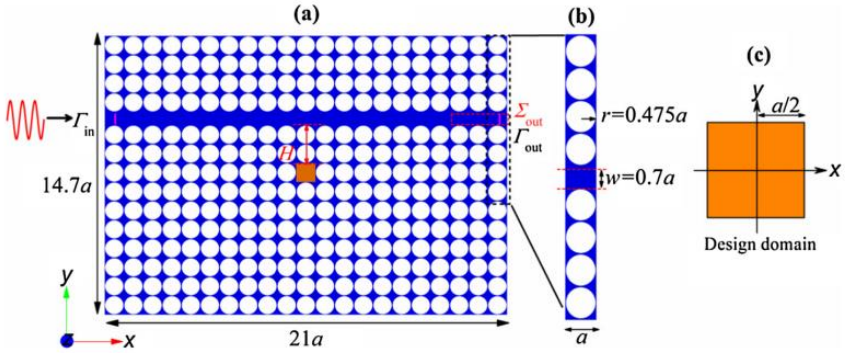

Figure 39. A PnC drop filter with a W1 waveguide and a single defect cavity

Three-Dimensional Crystal

Case 1 (3-D Steel Balls)

A hexagonal closed pack (hcp) arrangement was used for creating a 3-D phononic crystal by Merkel et al. [79] to study the acoustic transfer function (ATF). The crystal of unit cell 8×8×8 mm^3 was excited by a piezoelectric transducer from the bottom, and the vibration response of the crystal was determined through a laser vibrometer as shown in Figure 40.

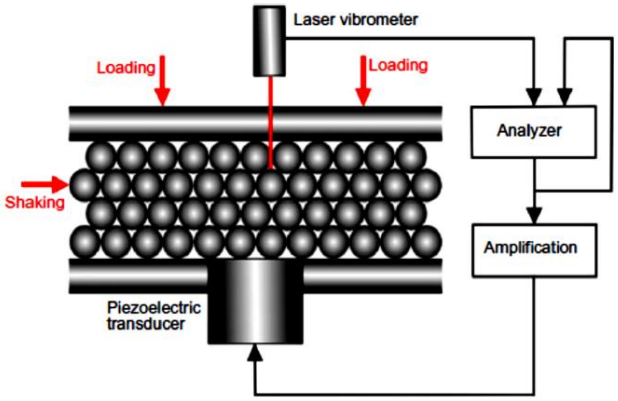

Figure 40. Schematic of Experimental Setup by Merkel et al. [79]

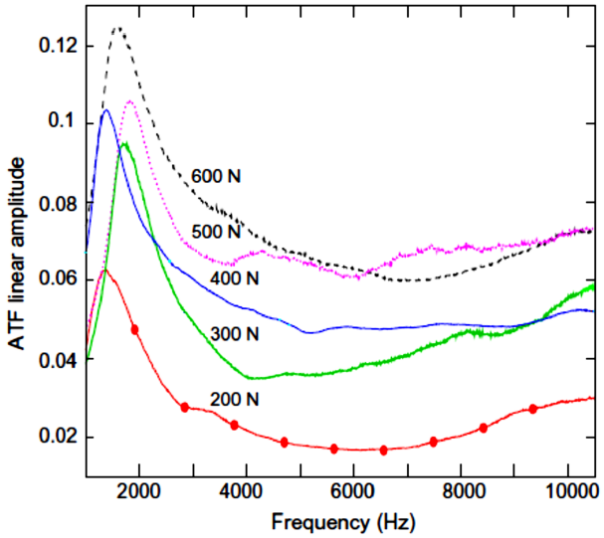

Figure 41. Evaluation of Resonance Frequency of the 3-D Granular Crystal [79]

The vibrometer was focused on a single ball of the top layer of a steel hcp crystal. The whole crystal was put inside a container with an external loading mechanism at the top. The crystal was experimented on by varying the load amplitude. The objective of the study was to determine the effect of the external loading on resonance

characteristics of the crystal which represents the natural frequency of the system. For different load conditions up to 10 kHz frequency the occurrence of resonance is shown in Figure 41.

Case 2 (3-D Steel Balls)

In order to show the evidence of rotational elastic waves in the Cosserat theory, Merkel and Tournat [80] carried out an experiment on a 3-D granular PC. Cosserat's theory predicts the contribution of rotation in different elastic wave modes. The theory predicts the existence of:

- Two pure longitudinal modes LA and LO,
- Two pure rotational modes R_1 and R_2 and
- Four coupled transverse and rotational modes RT_1, TR_1, RT_2, and TR_2.

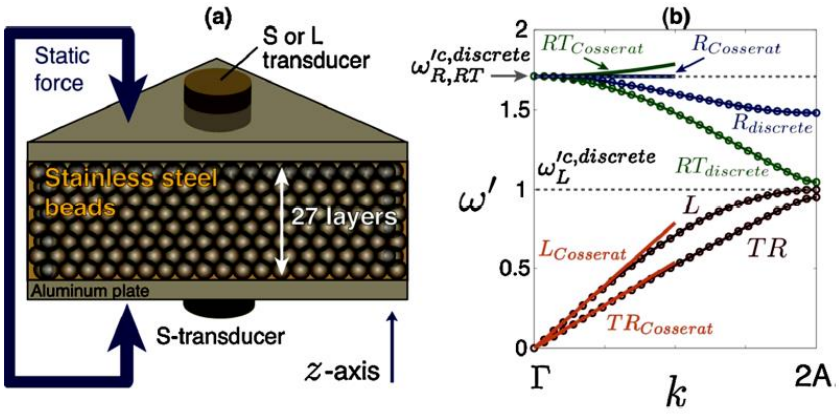

Figure 42. (a) Schematics of Experiment Setup (b) Theoretical Dispersion Modes [80]

The 3-D granular PC was arranged in the hexagonal closed packed (hcp) structure of steel balls (2 mm diameter) in a frame. The PC was excited from the bottom along the Z-axis by a shear piezoelectric transducer, and transmitted waves (0-200kHz) were obtained using two different transducers from the top (Figure 42a; Figure 42b). The receiving transducers are:

- L-receiver: a compressional transducer (sensitive only to the longitudinal mode L)

- S-receiver: a shear transducer (sensitive to shear modes (TR and RT) and longitudinal mode L).

Figure 43 shows the comparison of theoretical and experimental modes showing the evidence of rotational effects. In the case of the L-receiver in Figure 43, the RT mode was not captured since the transducer could only detect the longitudinal mode.

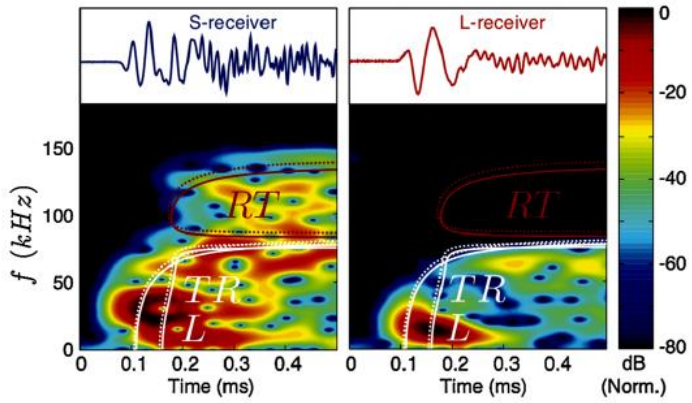

Figure 43. Received Signals from S and L Receivers (Top). The Spectrogram of Signal with Theoretical L, RT and TR Curves (Bottom) [80]

Table 8 summarizes the keys features of the Transducers experiments of metamaterials in the presented literature review.

Table 8. Summary of the listed experiments using Transducers

Serial	Specimen Description	Specimen Dimension	Experiment Frequency Range	Excitation System's Frequency	Excitation System's Displacement	Receiver
1	Steel-Copper Layer	7 mm	MHz			
2	Steel-Al-PVC Layer	35 mm	40.0 MHz			Piezoelectric vibrator
3	Quartz Cylindrical Discrete Crystal	290 mm	14.0 kHz	15.0 kHz (Piezomechanik: PSt 150/14/40VS20)	55 µm	Force sensor (PCB 208-C01)
4	Lead-Epoxy	8 mm	600 kHz	50.0 MHz	1-9 µm Range	Ultrasonic wave pulser

Serial	Specimen Description	Specimen Dimension	Experiment Frequency Range	Excitation System's Frequency	Excitation System's Displacement	Receiver
	Layer			(Panametrics: 5077-PR)		and receiver transducer (5077-PR Panametrics)
5	Rubber Coated Lead 2D Crystal	100×100 mm^2	3.0 kHz			Accelerometers (B*&K4057)
6	2-D Nylon with Air Hole	50×50 mm^2	0.5 MHz	1.0 MHz (Panametrics: V152)	1-9 μm Range	Panametrics V152 piezoelectric transducer
7	Hexagonal Aluminum	31.2×30 cm^2	3.1 kHz			3-D Laser Doppler vibrometer
8	3-D Steel Balls	8×8×8 mm^3 Unit Cell	10 kHz			Laser vibrometer
9	3-D Steel Balls	2×2×2 mm^3 Unit Cell	200 kHz			

2.2.3.3 Large Amplitude Excitation Based on Impact

One dimensional crystal

Case 1 (SHPB System)

Feng and Liu conducted two experimental studies on 1-D periodic composites by adopting a steel-based SHPB system to study the effect of initial stress [81] and confining pressure [82] on the band gap of 1D MM. The effect of initial stress was evaluated using periodic composites of steel-epoxy and aluminum-epoxy. The experimental setup of the test is shown in

Figure 44, and the transmission spectra obtained from the experiments are shown in

Figure 45. On the other hand, for different confining pressure on a steel-epoxy composite, the evolution of the transmission spectra is presented in Figure 46. Note that all the numerical and analytical results in these works were based only on the elastic property of epoxy.

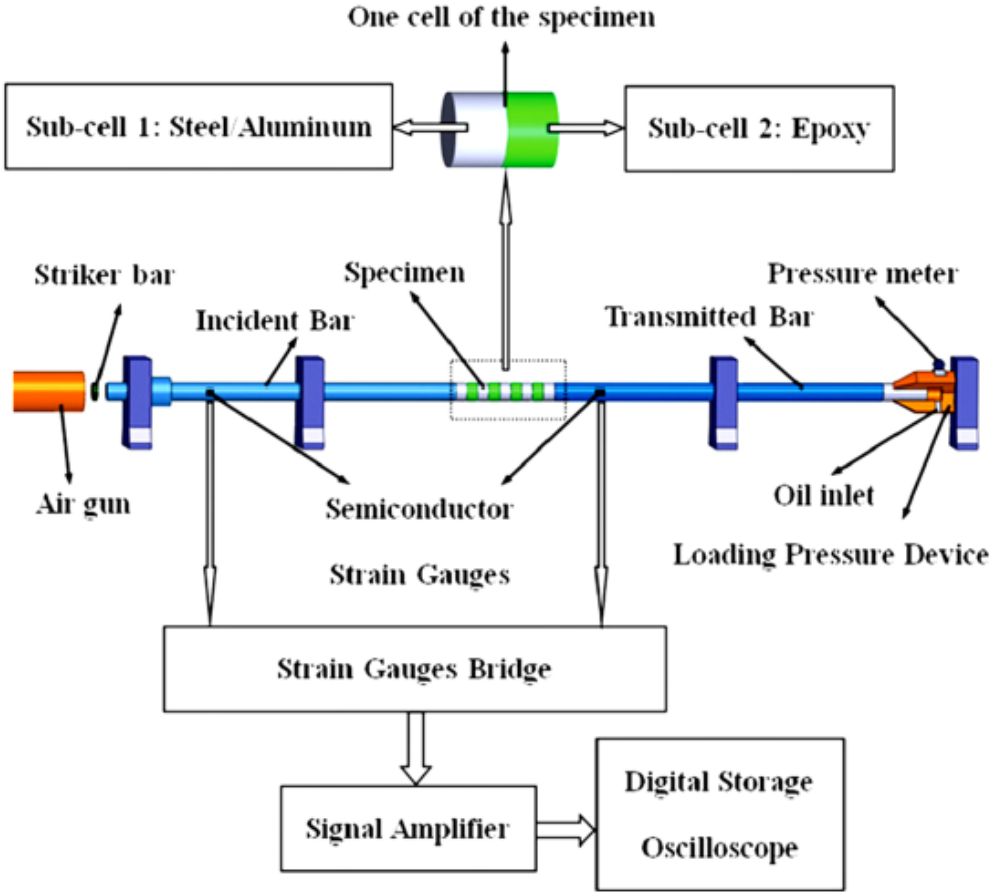

Figure 44. Schematic of SHPB Test for 1D phononic Crystal [81]

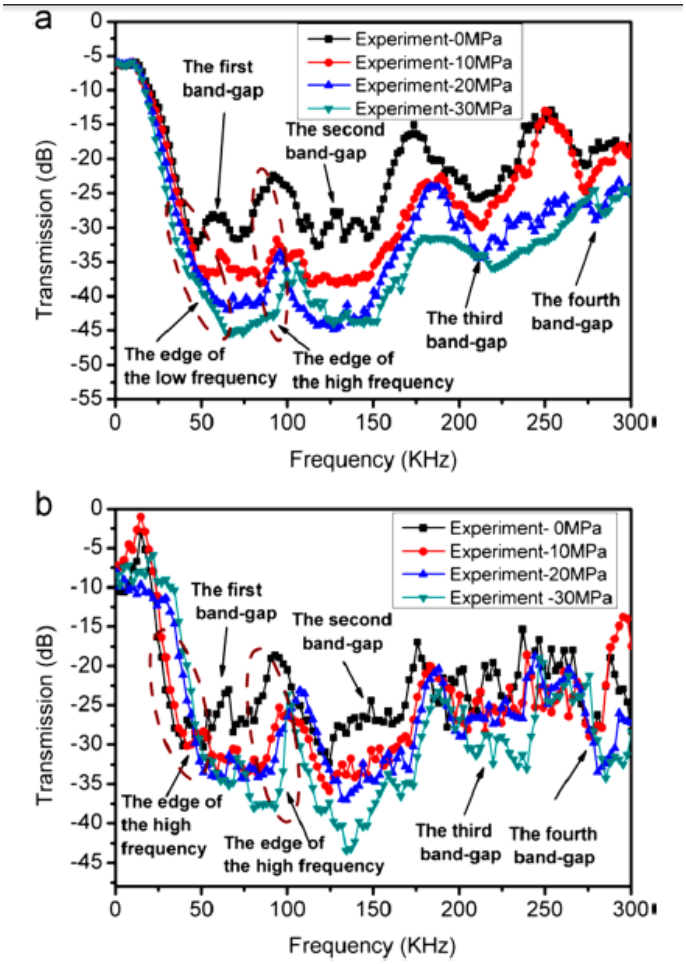

Figure 45. Transmission property of (a) Steel/Epoxy and (b) Aluminum/Epoxy with Different Initial Stresses [81]

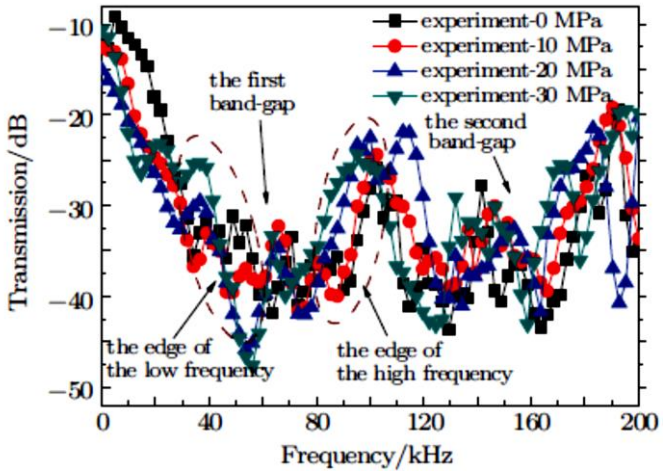

Figure 46. Change in Transmission Spectra of Layered Steel-Epoxy Crystal Due to Different Confining Pressure [82]

Case 2 (Nonlinear wave in the discrete periodic chain)

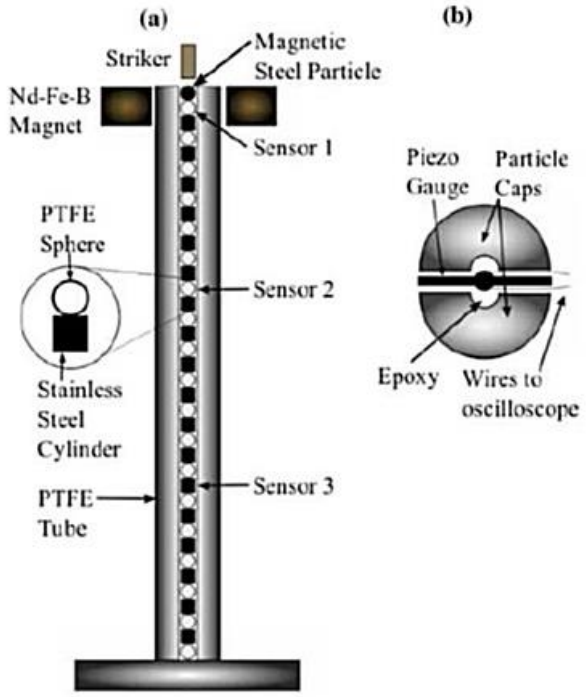

Figure 47. (a) Schematic of the experimental setup of diatomic crystal in the study of Herbold et al. [83] showing the 1D crystal enclosed in PTFE tube and striker (b) force sensor embedded in the PTFE sphere

Different types of nonlinear waves such as quasi-harmonic, solitary, and shock waves were generated in the discrete periodic chain using impact tests by Herbold et al. [83]. This study's objective was to generate linear, weakly nonlinear, and strongly nonlinear waves in a diatomic periodic chain composed of a PTFE sphere and steel cylinder. The total height of each unit cell was 7.88 mm, and the entire crystal was placed within a PTFE tube. The impact was created at the top of the crystal by using an Al2O3 cylindrical striker as shown in

Figure 47. The force in several PTFE spheres was obtained by embedding piezoelectric sensors. Moreover, the force on the wall was also recorded by a sensor. The entire 1D crystal was subjected to a pre-compression, and different types of waves were created by varying the mass of the Al2O3 striker (e.g., 0.61 gm, 1.22 gm, 2.75

gm, and 17.81 gm). Figure 48 shows a comparison of experimental and numerical results of the nonlinear wave at the PTFE sphere of the 13th cell and the wall.

The study showed that due to the nonlinear effect, the wave propagated within the band gap frequency range of the corresponding linear system. Moreover, a few other studies were conducted in similar experimental settings where various types of waves were created in discrete chains [84,85].

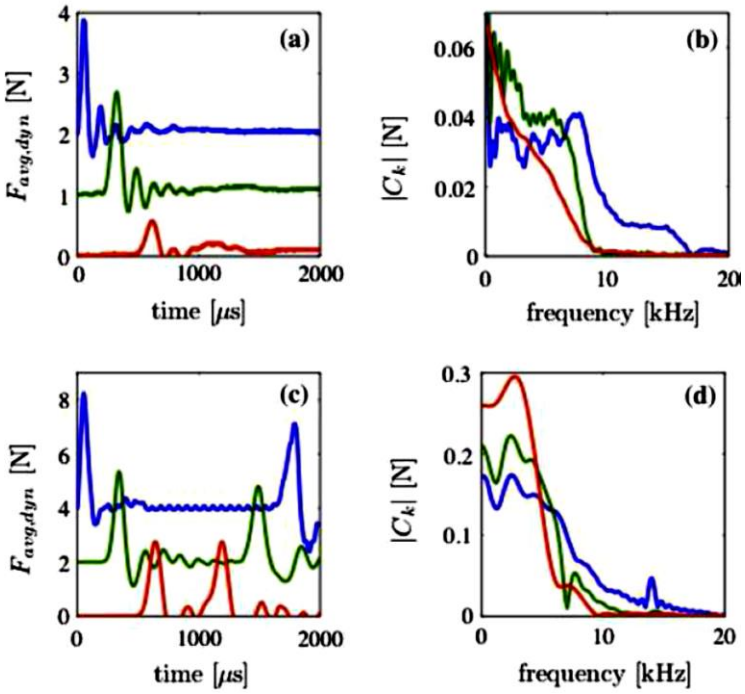

Figure 48. (a) Experimental wave signal generated by 2.75 gm striker at 13th cell (blue) and the wall (red); (b) Fourier spectrum of the experimental signals; (c) Numerically calculated force signals at 13th cell (blue) and the wall; (d) Fourier spectrum of the numerical signals [83]

Case 3 (amplitude-dependent band gap in the discrete periodic chain)

Yang and Dario [86] experimented on discrete periodic chains to find the amplitude-dependent band gap properties of discrete periodic chains. The periodic chain of unit length 28.63 mm consisted of spherical and cylindrical steel particles. The evolution of the linear band gap to nonlinear solitary waves in the crystal was studied by varying

the geometric configuration and impact condition. Two types of excitation systems, namely piezoelectric actuator, and impact strikers were used in the study. The actuator was exclusively used to generate a linear wave. On the other hand, a spherical aluminum striker and different sizes of cylindrical steel strikers were employed for the impact tests. Moreover, two types of configuration (straight and curved) of the periodic chain were used which is shown in

Figure 49.

The crystal was subjected to static pre-compression F_o during the study. By varying the striker sizes, impact forces F_d ranging between 50-1000 N were applied at the top of the crystal. It was found that, due to an increase of the striking force, the band gap starts to shift to a lower frequency range. Figure 50 shows that the band gaps eventually disappear at a high ratio of F_d/F_o.

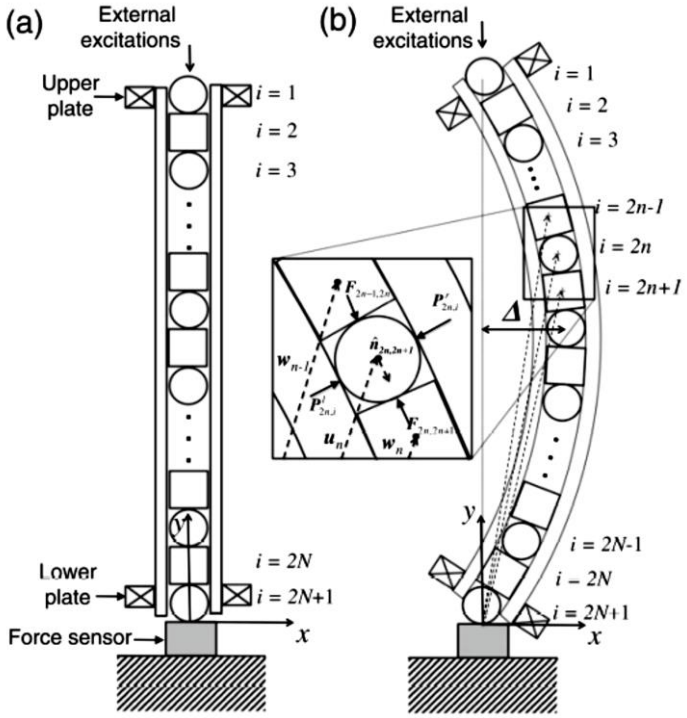

Figure 49. Experimental setup of diatomic crystal in (a) straight configuration and (b) curved configuration in the study of Yang and Dario [86]

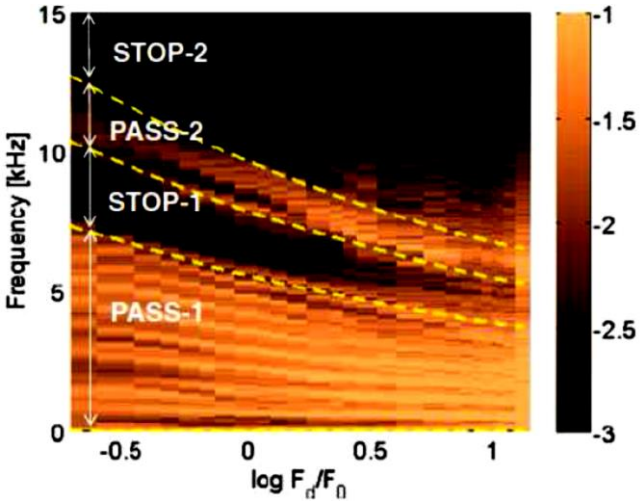

Figure 50. Power spectral density from an experiment showing the effect of nonlinearity on band gap of diatomic crystal. The black zone represents the band gap which disappears at a higher value of F_d/F_o [86]

Two-dimensional crystal

Case 1 (2D granular system)

Nonlinear wave propagation in the 2D granular crystal was investigated by Yang and Sutton [87]. The particularity of this research is that it was performed to show the importance of rotational dynamics between granular particles. Two types of crystals, a straight granular chain and the 2D granular system were considered. The 2D crystal was arranged in hexagonal packing which consisted of 19.05mm diameter steel spheres as shown in

Figure 51. The impact force on the crystal was applied by similar spheres where the striker was released from a higher ramp. The force at every three particles was measured using embedded sensors.

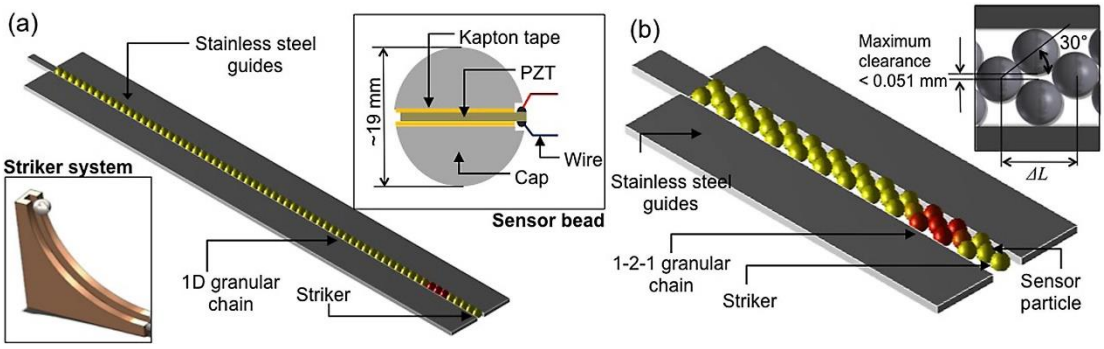

Figure 51. Schematics of the experimental setup of (a) linear 1D chain and (b) 2D hexagonal granular crystal used by Yang and Sutton [87]

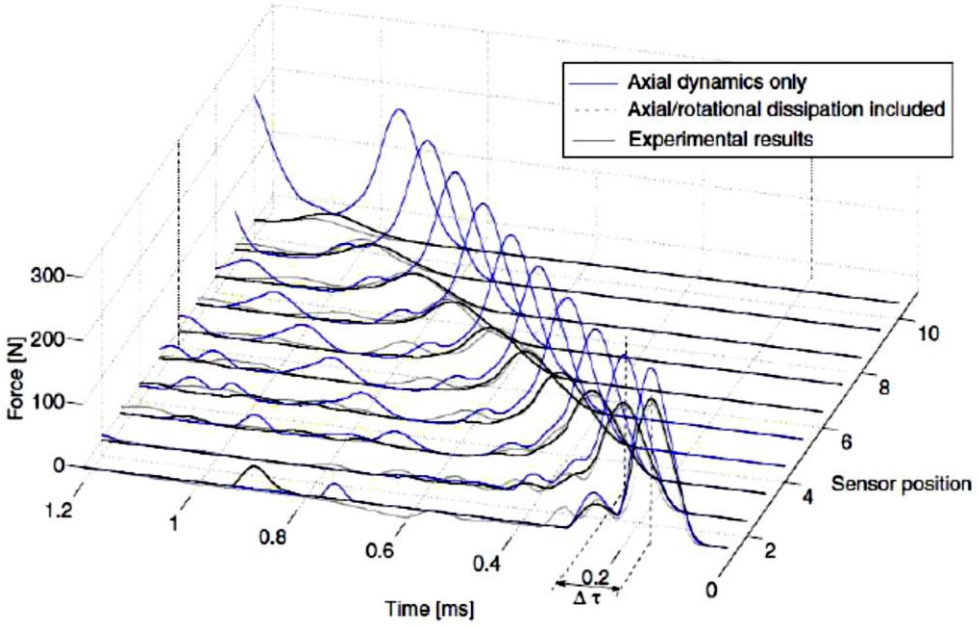

Figure 52. Comparison of temporal profiles obtained from numerical model considering axial dynamics (solid blue lines), a numerical model based on axial-rotational interaction (dotted gray lines), and experimental result from force sensors (solid gray lines) [87]

A numerical model was created based on Hertz-Mindlin's contact to capture both axial and rotational interactions between the particles. Rotational motion in the 2D crystal was introduced by the distribution of the impact force on the ±30^{o} inclined spheres (see

Figure 51b). Due to this configuration, the particles were subjected to both axial and

rotational interaction. Two numerical models were compared with the experimental result, where only the axial dynamics were considered for the first model, and both axial-rotational interactions were included in the other model. The temporal force profiles in several sensors are shown in Figure 52. Here, blue lines denote the numerical model with only axial dynamics, the dotted gray lines represent a numerical model which considers the axial-rotational interaction, and the experimental result is shown by solid gray lines. The result proved that the inclusion of rotational interaction resembles more the experimental result.

CHAPTER 3: DISPERSION RELATION OF VISCOELASTIC MULTILAYERED COMPOSITE

3.1 Introduction

Although spectral band gaps can be induced through mechanical joints, e.g., in helical waveguides [88], conventional elastic structural materials (e.g., metals) typically have narrow spectral band gaps in the high-frequency range [63,89]. Therefore, the use of viscoelastic materials is crucial to lowering the band gap frequencies. The band gap frequencies of typical phononic crystals (PCs) are of the order of the ratio v/a, where v is the wave speed in the medium and a is the lattice constant related to the thickness of the lattice structure [90].

Numerous researchers have observed that viscoelasticity not only attenuates wave transmission but also modifies the band gap frequencies which are substantially displaced and widened [20,21,91,92]. For matrices (i.e., an array of PCs) made of conventional structural materials such as metals, the band gap structures for low frequencies would require impractical meter-scale macrostructures. Smaller microstructures (e.g., millimeter-scale) can only be achieved by using compliant matrix materials with very low elastic moduli, such as elastomers (i.e., polymers with viscoelastic properties). Researchers have considered the viscoelasticity of these polymers since their damping attenuation affects the overall periodic composite vibration attenuation. Tanaka and Kon-No [39] used the polymer complex moduli to compute the dispersion relation of viscoelastic-elastic layered composites. Other numerical methods have attempted to determine the complex dispersion relation of viscoelastic composites such as the transfer matrix method [40].

This chapter presents the analytical dispersion relation of an arbitrary multilayered

crystal using the transfer matrix method. Due to the assumption of elastic behavior of the crystal, the results from this chapter serve as a limited reference for the viscoelastic time-domain and frequency domain simulations in chapter 4. The code written for the transfer matrix also serves as a control specimens' topology design tool in the next chapter.

3.2 Dispersion relation for Phononic Crystals

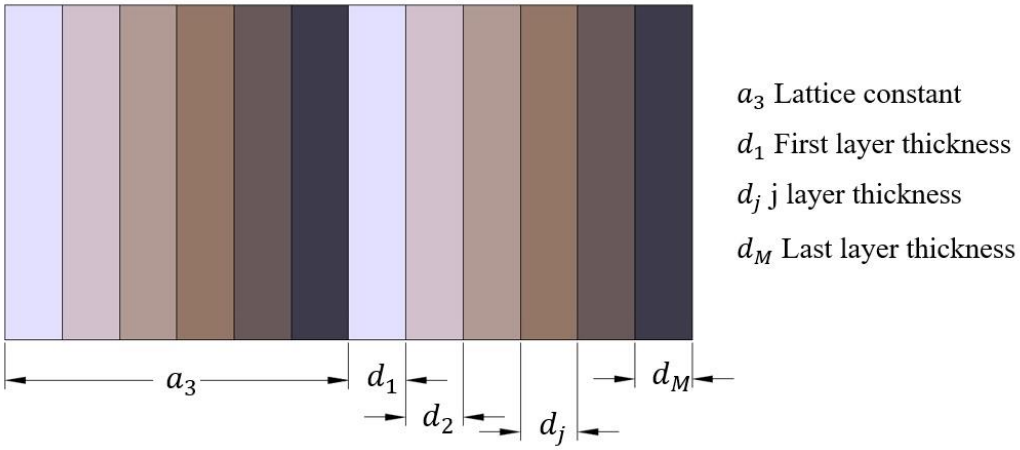

Figure 53. Infinitely periodic multilayered composite

In this section, the focus is on the study of the plane wave on infinitely periodic multilayered composites in the x_3 direction (see Figure 53). According to the Bloch periodic condition, the displacement field $u(x)$ of an r – periodic composite due to plane wave propagation is:

$$u(x+1) = u(x)e^{i\kappa r} \quad (1)$$

Where κ is the wave vector.

For a one-dimensional layered composite with M layers per unit cell, the j-th layer would have a density ρ_j and a thickness d_j. The lattice constant is then $a_3 = \sum_{j=1}^{M} d_j$. When the MM is subjected to a harmonic wave with a ω frequency, the displacement and the stress fields in $x_1 - x_3$ plane for the n-th unit cell at the j-th layer are:

$$u_{3,j,n}(x_{3,j,n}, t) = [P_{F,j,n}e^{-\frac{i\omega x_{3,j,n}}{c_{p,j}}} + P_{B,j,n}e^{\frac{i\omega x_{3,j,n}}{c_{p,j}}}]e^{-i\omega t} \quad (2)$$

$$u_{1,j,n}(x_{3,j,n},t) = [Q_{F,j,n}e^{-\frac{i\omega x_{3,j,n}}{c_{s,j}}} + Q_{B,j,n}e^{\frac{i\omega x_{3,j,n}}{c_{s,j}}}]e^{-i\omega t} \quad (3)$$

Where $c_{p,j}$ and $c_{s,j}$ are the pressure and shear waves of the j-th layer and $P_{F,j,n}$, $P_{B,j,n}$, $Q_{F,j,n}$ and $Q_{B,j,n}$ are unknown coefficients. Note that the pressure and shear waves are decoupled in the displacement and stress fields. Since the derivation of the pressure and shear dispersion relations are similar, only the calculation for the pressure wave is presented here. Due to the continuity of the stress and displacement fields, the following boundary conditions are applied at the interface between j-th and $j+1$-th layers of the n-th unit cell.

$$[u_{1,j,n}]_{x_{3,j,n=d_j}} = [u_{1,j+1,n}]_{x_{3,j+1,n=0}},$$

$$[u_{3,j,n}]_{x_{3,j,n=d_j}} = [u_{3,j+1,n}]_{x_{3,j+1,n=0}},$$

$$[\sigma_{31,j,n}]_{x_{3,j,n=d_j}} = [\sigma_{31,j+1,n}]_{x_{3,j+1,n=0}},$$

$$[\sigma_{33,j,n}]_{x_{3,j,n=d_j}} = [\sigma_{33,j+1,n}]_{x_{3,j+1,n=0}} \quad (4)$$

After applying the continuity boundary conditions successively at each interface, the transfer matrix T_p which relates the first interface of n-th and $n+1$-th unit cells can be established as:

$$W_{p,1,n+1} = T_p W_{p,1,n} \quad (5)$$

Where

$$W_{p,1,n} = \begin{bmatrix} P_{F,1,n} \\ P_{B,1,n} \end{bmatrix} \text{ and } W_{p,1,n+1} = \begin{bmatrix} P_{F,1,n+1} \\ P_{B,1,n+1} \end{bmatrix}$$

$$T_p = R_{p,1}^{-1}\left(R_{p,M}D_{p,M}R_{p,M}^{-1}\right)\ldots\left(R_{p,2}D_{p,2}R_{p,2}^{-1}\right)R_{p,1}D_{p,1}$$

$$= R_{p,1}^{-1}\left(\prod_{j=2}^{M} R_{p,M+2-j}D_{p,M+2-j}R_{p,M+2-j}^{-1}\right)R_{p,1}D_{p,1}$$

$$R_{p,j} = \begin{bmatrix} 1 & 1 \\ -\omega\rho_j c_{p,j} & \omega\rho_j c_{p,j} \end{bmatrix}, D_{p,j} = \begin{bmatrix} e^{-\frac{i\omega d_j}{c_{p,j}}} & 0 \\ 0 & e^{\frac{i\omega d_j}{c_{p,j}}} \end{bmatrix} \quad (6)$$

Moreover, according to the Bloch periodic boundary condition (Equation 1), another relationship between the coefficient vectors can be written as:

$$W_{p,1,n+1} = e^{i\kappa_3 a_3} W_{p,1,n} \quad (7)$$

Combining Equations (5) and (7), the eigenvalue problem of the 1D MM is:

$$T_p W_{p,n} = e^{i\kappa_3 a_3}\, W_{p,n} \quad (8)$$

When solving the characteristic polynomial equation of the eigenvalue problem, the dispersion relation of plane pressure wave propagation perpendicular to the layers is:

$$\cos(\kappa_3 a_3) = \frac{tr(T_p)}{2} \quad (9)$$

Where $tr(T_p)$ represent the trace of the matrix. For a two-layered periodic MM, the dispersion relation becomes [38]:

$$\cos(\kappa_3 a_3) = \cos(\frac{\omega d_1}{c_{p,1}}) \cos\left(\frac{\omega d_2}{c_{p,2}}\right) - \frac{1}{2}\left(\frac{\rho_1 c_{p,1}}{\rho_2 c_{p,2}} + \frac{\rho_2 c_{p,2}}{\rho_1 c_{p,2}}\right) \sin(\frac{\omega d_1}{c_{p,1}}) \sin(\frac{\omega d_2}{c_{p,2}}) \quad (10)$$

3.3 Geometry and Materials of Viscoelastic-Elastic Composite

The samples used for the application of the previous section methodology were bilayered phononic crystals composed of Aluminum alloy (6061-T6) and viscoelastic material layers. The two viscoelastic materials used were Elite Double 32 from Zhermack, a vinylsiloxane, and Hapflex 560 from Hapco Inc., a hybrid elastomeric polymer alloy. All the material properties are listed in Table 9. The thicknesses of the layers for an infinitely periodic, bilayered phononic crystal are detailed in

Table 10. A MATLAB code is written to execute the dispersion relation calculation described in section 3.2.

Table 9. Elastic Properties of the Materials

Properties	Elite Double-32	Hapflex-560	Aluminum alloy 6061-T6
Elastic Modulus (MPa)	0.83	9.58	68900

Density (kg/m^3)	1196	1060	2700

Table 10. Geometry of composites

Phononic Crystal		Thickness of layers	
		Aluminum alloy	Polymer
Elite double 32	510ED32	5 mm	10 mm
	55ED32	5 mm	5 mm
	520ED32	5 mm	20 mm
	530ED32	5 mm	30 mm
	1010ED32	10 mm	10 mm
Hapflex 560	510H560	5 mm	10 mm
	55H560	5 mm	5 mm
	520H560	5 mm	20 mm
	530H560	5 mm	30 mm
	1010H560	10 mm	10 mm

3.4 Dispersion relation results

The results of treating the viscoelastic materials as an elastic material are shown in the dispersion relation of the MMs in

Table 10, using equation 10 and the equivalent transversal equation in Figure 54 to Figure 63.

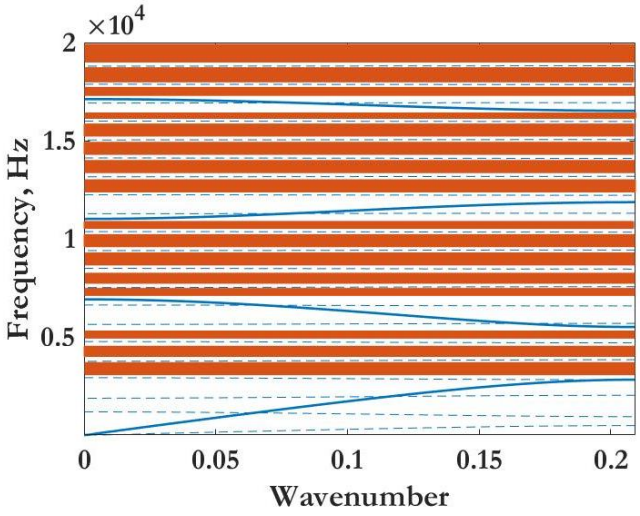

Figure 54. Dispersion relation of a MM specimen consisting of 5 mm Aluminum and 10 mm Elite Double 32

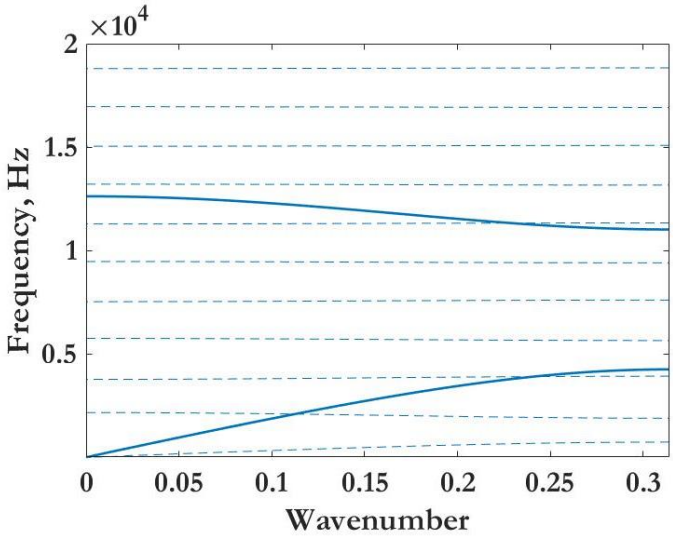

Figure 55. Dispersion relation of a MM specimen consisting of 5 mm Aluminum and 5 mm Elite Double 32

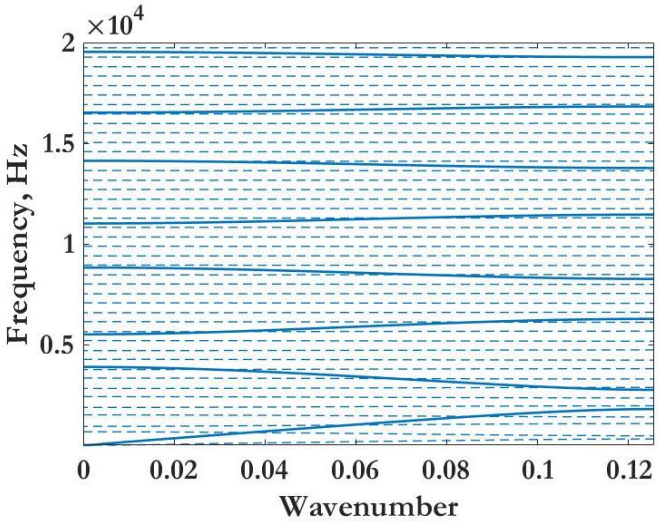

Figure 56. Dispersion relation of a MM specimen consisting of 5 mm Aluminum and 20 mm Elite Double 32

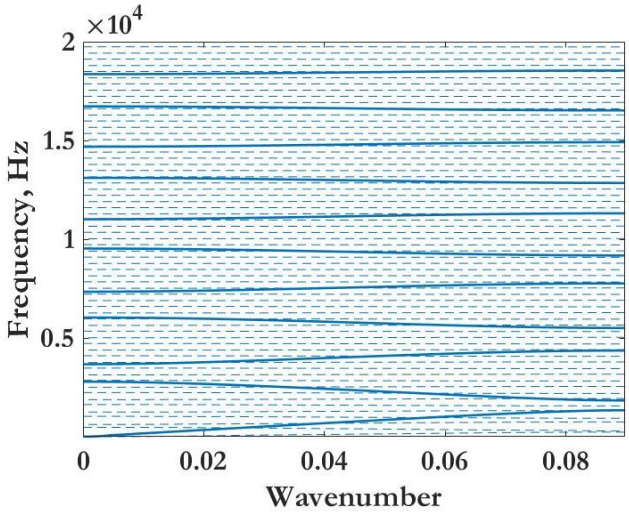

Figure 57. Dispersion relation of a MM specimen consisting of 5 mm Aluminum and 30 mm Elite Double 32

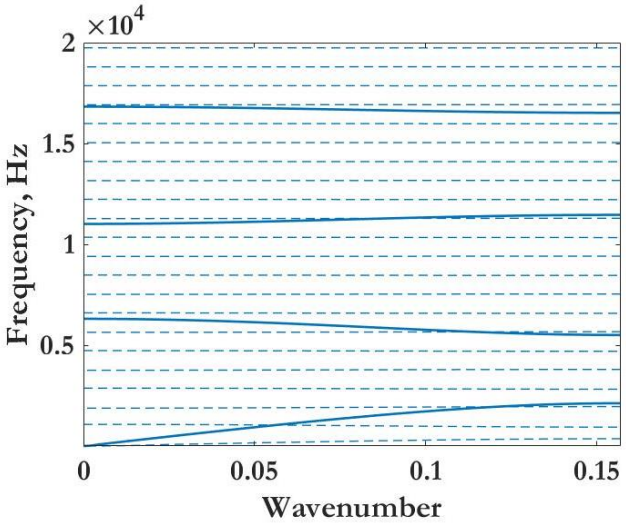

Figure 58. Dispersion relation of a MM specimen consisting of 10 mm Aluminum and 10 mm Elite Double 32

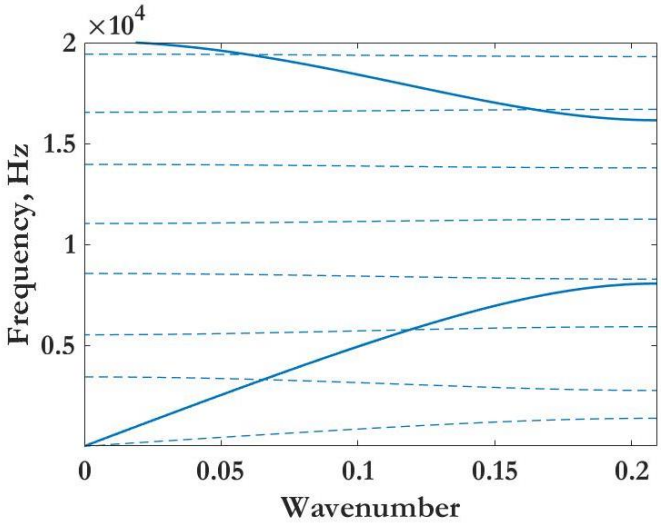

Figure 59. Dispersion relation of a MM specimen consisting of 5 mm Aluminum and 10 mm Hapflex 560

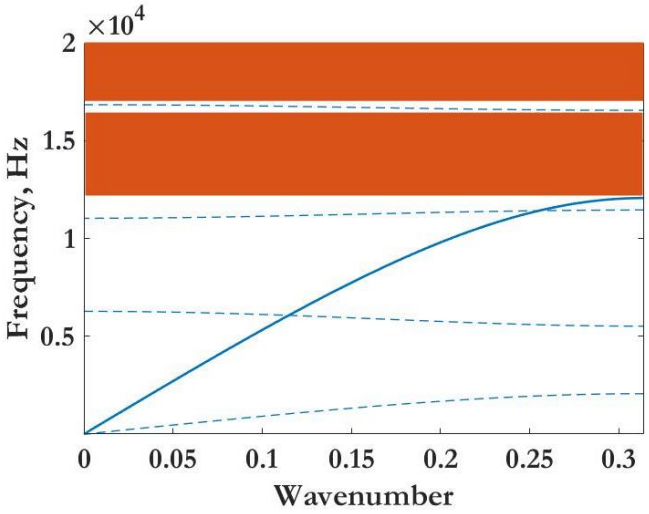

Figure 60. Dispersion relation of a MM specimen consisting of 5 mm Aluminum and 5 mm Hapflex 560

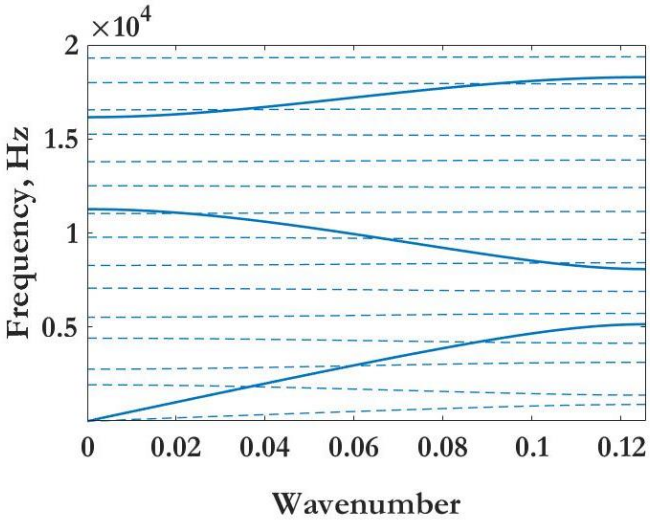

Figure 61. Dispersion relation of a MM specimen consisting of 5 mm Aluminum and 20 mm Hapflex 560

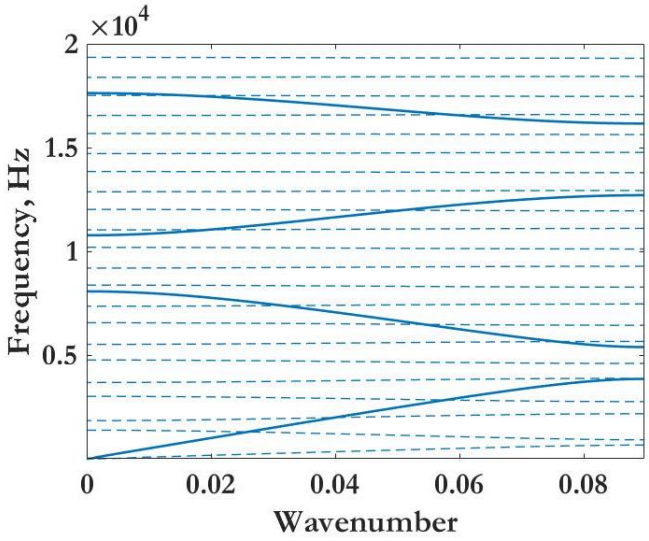

Figure 62. Dispersion relation of a MM specimen consisting of 5 mm Aluminum and 30 mm Hapflex 560

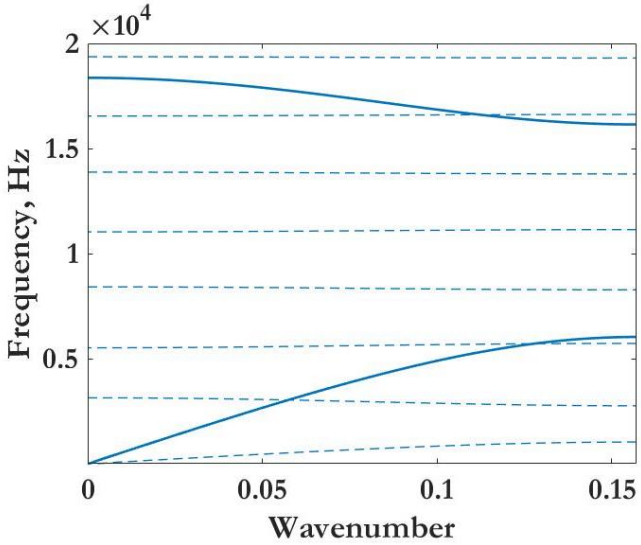

Figure 63. Dispersion relation of a MM specimen consisting of 10 mm Aluminum and 10 mm Hapflex 560

3.5 Discussion

Figure 54 to Figure 63 represent different phononic dispersion relations for wave propagation through infinitely bilayered phononic crystals. The longitudinal and transversal dispersions are presented by a solid line and a dotted line, respectively. In Figure 54, the orange bands represent the band gaps. In the same figure, the ranges from 2801 Hz to 5521 Hz, 7041-10960 Hz, 11840-16560 Hz and 17200-20000 Hz are

considered longitudinal band gaps for an infinite periodic material composed of 5 mm of Aluminum alloy and 10 mm of Elite Double 32. When comparing the first stop bands of the specimens 510ED32 and 510H560, it is noted that Elite double 32 combined with aluminum allowed better attenuation at low-frequency ranges. This was due to the impedance mismatch between the aluminum alloy and the silicone rubber (Elite double 32). The polymeric materials were used in the periodic structure primarily for their low stiffness. As a result, the metamaterials produced from a combination of polymer and metal achieved high impedance mismatches, which in turn gave a large band gap property in the low-frequency range.

3.6 Conclusion

In this chapter, the analytical dispersion relation of an arbitrary multilayered crystal was computed using the transfer matrix method assuming that the layers had elastic behavior. First, the plane wave on the sagittal direction was investigated using Bloch's periodic condition to obtain the plane wave propagation relation. The formulation was then applied to a bilayered phononic crystal composed of Aluminum alloy (6061-T6) and polymer layers (Elite Double 32, Hapflex 560, Hapco) with different geometries. The dispersion relation was plotted to show potential analytical pass and stop bands. Viscoelastic materials with a low modulus of elasticity increased the performance of viscoelastic phononic crystals in low frequency range vibration attenuation. The hypothesis of the method that the materials were elastic did not cover the inherent damping of the viscoelastic materials. This aspect is explored in the next chapter.

CHAPTER 4: OPTIMIZATION OF VISCOELASTIC METAMATERIALS FOR VIBRATION ATTENUATION PROPERTIES

4.1 Introduction

Extreme applications in construction and other domains have created a high demand for engineered materials with enhanced mechanical properties such as high energy absorption [93,94], vibration control [95,96] and acoustic shielding [97,98]. Mechanical metamaterials (MMs) incorporating viscoelastic constituents provide promising solutions to extreme loading problems. The impetus to incorporate viscoelastic constituents in MMs stems mainly from their properties, such as strong energy absorption, inherent damping, and low elastic modulus. However, viscoelastic materials exhibit significantly high damping at high frequencies (above 20 kHz) [99], which is beyond the audio frequency range (20 Hz – 20 kHz) and well beyond the human range of sensitivity to sound (1 to 4 kHz) [100]. Incorporating viscoelastic materials in one-dimensional (1D) MMs in a bilayered or multilayered fashion with periodic variations can simultaneously lower the spectral band gap and introduce damping that is inherent to the viscoelastic component of the MM. Resulting in lower vibration transmission in the lower frequency range which is within the range of higher human sensitivity to sound and vibration.

Although spectral band gaps can be induced through mechanical joints, e.g. in helical waveguides [88], conventional elastic structural materials (e.g., metals) typically have narrow spectral band gaps in the high-frequency range [63,89]. Therefore, the use of viscoelastic materials is crucial to lowering the band gap frequencies. The band gap frequencies of typical phononic crystals (PCs) are of the order of the ratio v/a, where v is the wave speed in the medium and a is the lattice constant related to the thickness of the lattice structure [90]. Soft Materials are the next generation of smart materials,

and the mechanics of soft smart metamaterials (using soft materials, such as hydrogel, elastomer, SMP…) is an emerging topic in the last decade. Huang et al. [101] discussed recent advances in the understanding of the mechanical behavior of the constitutive models of hydrogels and SMPs. Furthermore, Zheng et al. [102] developed the theory of the fast diffusion of hydrogels under different stimuli. Toward validating this theory, the authors applied three different stimuli: the chemical potential, the temperature, and the hydraulic pressure, respectively. It was found that the theory predicts the dynamic behavior of the diffusion process of hydrogels, especially the type driven by hydraulic pressure.

Numerous researchers have observed that viscoelasticity not only attenuates wave transmission but also modifies the band gap frequencies which are substantially displaced and widened [20,21,91,92]. Arrays of phononic crystal made of metals necessitate quite large dimensions to generate a band gap in low frequency ranges. Smaller microstructures (e.g., millimeter-scale) can only be achieved by using compliant matrix materials with very low elastic moduli, such as elastomers (i.e., polymers with viscoelastic properties).

Although most previous studies have focused on investigating viscoelastic MMs numerically based on the framework of linear viscoelasticity [22,24,92], a few studies have reported experimental investigations of viscoelastic MMs. For example, a number of researchers have used specimen-specific experimental methods such as the bead-chain setting [84], the ultrasonic technique [103], impedance tubes [103,104] and electrodynamic shaker tests [105]. Daraio et al. [84] observed that chains of polytetrafluoroethylene (PTFE) beads with different diameters provide low signal propagation speed due to its exceptionally low Young's modulus and despite the viscoelastic nature of PTFE. Meng et al. [103] reported that an optimized MM slab

can attenuate vibration in the frequency range of 800-2,500 Hz, which illustrates the feasibility of combining several locally resonant acoustic MM layers for the design of anechoic coatings. Shan [66] harnessed multiple folding mechanisms in a periodic triangular elastomeric structure. He studied the effect of buckling and instability of the structure on the vibration attenuation, first by calculating the dispersion of the deformed configuration, then by considering three deformed configurations. Results showed that band gaps can be greatly affected depending on the geometry and the extent of the deformation. A limited number of studies have validated the corresponding numerical developments [68,103]. For example, Merheb et al. [92] utilized the finite difference time domain method to estimate the transmission spectra in the considered PC structure. Comparing the experimental and numerical results revealed that an elastic representation is sufficient to account for the behavior of the PC. Dong et al. [106] developed an optimization algorithm for structural optimization of elastic MMs which consists of an artificial neuronal network (ANN) trained with machine learning technics and optimized by GA. This surrogate algorithm has proven viable for elastic band gap prediction.

The optimization of 1D and two-dimensional (2D) viscoelastic MMs using finite element (FE) modeling has been the focus of many studies [107–110]. For instance, Hussein et al. [107] studied the dispersion in wave transmission by using a multi-objective genetic algorithm to generate a band gap frequency in an optimized 1D crystal topology. Sigmund and Jensen [111] proposed using topology optimization to design periodic materials and structures for obtaining a wave propagation band gap. Infinitely periodic crystals were considered to widen the band gap [108]. All of the aforementioned 1D and 2D topology optimization studies relied only on numerical simulations with no experimental validation. Moreover, the viscoelastic component

of MMs in these studies was modeled using the linear theory of elasticity [37].

This chapter describes how GA was used to optimize the geometry of bilayered MMs. GAs are evolutionary algorithms, which are biologically inspired optimization tools [112]. They are likely to find global optima without getting stuck around local optimal solutions and failing to reach convergence [113]. Besides, GAs apply to problems with linear and nonlinear constraints [114,115].

As mentioned above, several researchers have documented the optimization procedures of MMs. However, these studies have not sufficiently addressed the viscoelastic behavior of MMs and have not validated the optimization results through experimental testing. In this chapter, an automated optimization procedure based on GAs was used to optimize viscoelastic MM crystals to maximize their vibration attenuation capabilities in a specific low-frequency range. A steady-state dynamic analysis was performed to determine the frequency response function (FRF) of the MM crystals. The optimization parameters in this study describe the geometry of the 1D MM crystal, namely the lattice constant and the metal layer thickness. It is well documented that both mass and vibration attenuation are inherently related. Therefore, a multiobjective optimization procedure designed to minimize weight and maximize the vibration attenuation, was proposed in this study. The cost functions to be minimized were the total mass of the specimen and the FRF performance of the MM within a specific low-frequency range. All the numerical models were verified experimentally via an electrodynamic shaker test.

4.2 Experimental shaker tests

4.2.1. Test specimens

MMs comprising multilayered media with periodic variation were used in this study. The thickness of a periodic cell is called the lattice constant – denoted by L in Figure 64. The MM tested in this study was a bilayered crystal composed of metal and

polymer layers. The thickness represented the dimension of a layer in the longitudinal direction. The filling fraction was the ratio between the thicknesses of the constituents of the unit cell (namely a_1/a_2 in Figure 64), where a_1 was the thickness of the metal, and a_2 was the thickness of the polymer.

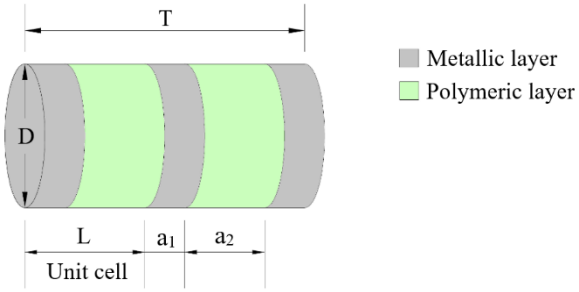

Figure 64. Geometry of a cylindrical MM

Cylindrical specimens were manufactured from layers of a polymer (Elite Double 32, Zhermack), alternating in a periodic arrangement with aluminum alloy layers (6061-T6). It is worth mentioning that MMs are commonly composed of metals and polymers to exploit the high impedance mismatch between these two materials for wave attenuation [116]. The properties of the aluminum alloy used in this study are shown in Table 11. The polymer used in this study was a silicone rubber material and it was chosen because of its low elastic modulus and since it had been effectively used previously in the tuning of vibration band gaps [58,117]. The polymer was prepared by mixing equal volumes of a base and catalyst to obtain a Vinylpolysiloxane. The polymer was then cast in a mold with different thicknesses. The density of the polymer and its Poisson's ratio are also shown in Table 11. Cylindrical aluminum layers were then glued to the polymer with a thin layer of silicone caulking product (Oxime).

The frequency-dependent storage and loss modulus, expressed in equation (11), have been determined through dynamic mechanical analysis (DMA) using an RSA-G2 Solids analyzer from TA instruments by applying infinitesimal strain. Detailed DMA testing results are presented in Appendix A.

$$E = E' + i\,E'' \quad (11)$$

Where E is the modulus of elasticity E' is the storage modulus and E" is the loss modulus.

Figure 65a shows the DMA testing equipment, while Figure 65b shows the obtained frequency-dependent loss and storage moduli. The generalized Maxwell model was used to represent the time-dependent behavior of Elite double 32. To identify the elastic equilibrium modulus E_∞ and Prony series coefficients, a rheological tool kit, IRIS [118] was used. Prony series coefficients of the elite double 32 are presented in Table 12 and the $E_\infty = 1.196\ MPa$.

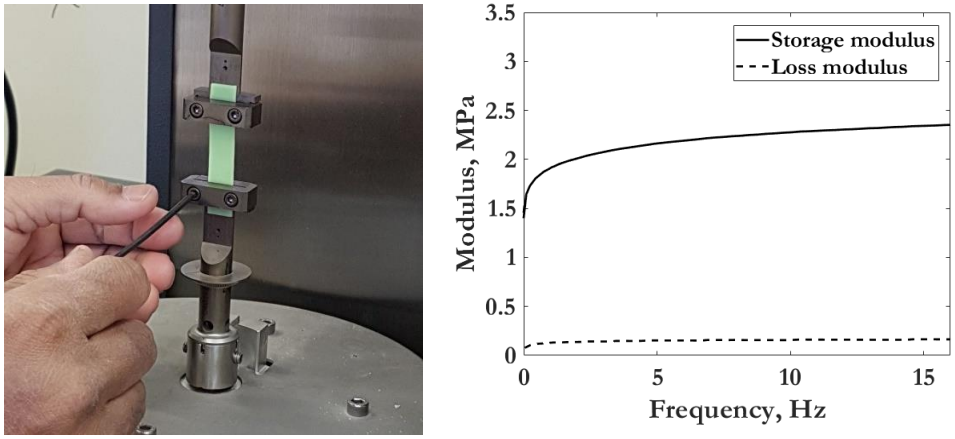

(a) (b)

Figure 65. DMA testing of Elite double 32

Three cylindrical specimens (A, B, and C) with a 40 mm diameter were tested to obtain statistical accuracy and precision and to validate the numerical models as specified in Table 13. The thicknesses were estimated via an analytical method which assumed that the viscoelastic part was linear elastic so as to have an initial estimate of the passbands and stopbands through the considered frequency range (1 to 1200 Hz). The analytical calculation was conducted using the transfer matrix method [119,120].

Table 11. Properties of considered materials

Material	Properties	Values
Aluminum	Young's Modulus (GPa)	68.9
	Density (kg/m^3)	2700
	Poisson's ratio	0.33
Elite Double 32	Density (kg/m^3)	1134
	Poisson's ratio	0.497

Table 12. Prony series coefficients of Elite Double 32 [121]

Branch Number, j	Modulus E_j, MPa	Relaxation Time, s
1	0.477	4.99 × 10-8
2	0.328	4.83 × 10-7
3	0.221	3.55 × 10-6
4	0.157	1.72 × 10-5
5	0.113	6.04 × 10-5
6	0.127	2.28 × 10-4
7	0.114	1.33 × 10-3
8	0.077	9.07 × 10-3
9	0.059	6.42 × 10-2
10	0.043	4.89 × 10-1

Table 13. Geometry of the tested specimens

Specimen Name	Thickness of components		Number of layers	
	Aluminum alloy	Polymer	Aluminum alloy	Polymer
A	10 mm	10 mm	8	7
B	5 mm	20 mm	6	5
C	5 mm	30 mm	5	4

4.2.2 Experimental setup

An experimental set-up consisting of an electrodynamic shaker (Type 4809, Brüel & Kjær) was used to monitor the dynamic response of a MM crystal subjected to longitudinal vibration as shown in Figure 66. The signal was generated by a power amplifier (Type 2718, Brüel & Kjær). The output and input signals were recorded with a miniature accelerometer (Type 4394 piezoelectric CCLD accelerometer, Brüel & Kjær) and a force transducer (Type 8230-001, Brüel & Kjær), respectively. The force transducer and accelerometer measured the input force applied to the specimen and the output acceleration signal, respectively. The test set-up was placed on a passive optical table (Model T46H-PTP602, Thorlabs) to isolate it from ambient vibrations (Figure 66b). The specimens were placed on a circular base connected to the force transducer and were attached to an accelerometer at the top, as shown in Figure 67. Additional viscoelastic phononic crystals test results are shown in Appendix B.

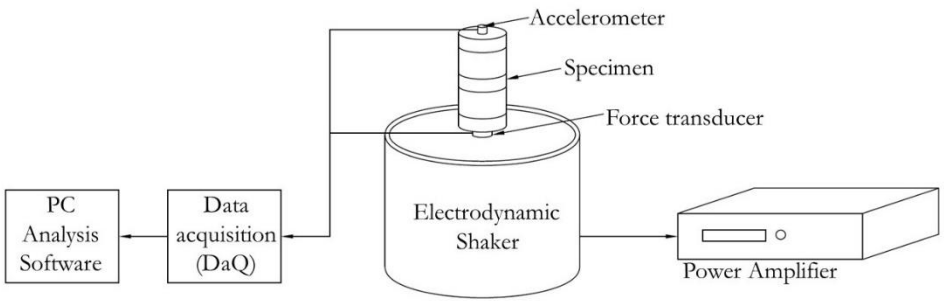

a) Schematic of the electrodynamic shaker test

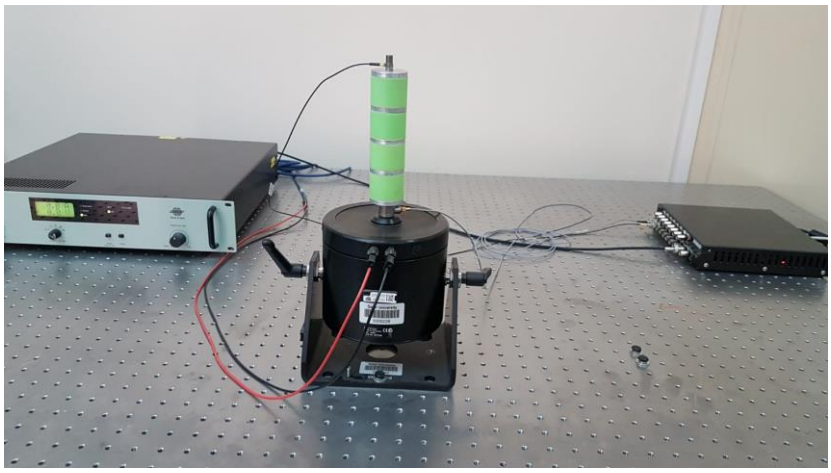

b) Set-up placed on an optical table (specimen C is shown in the photo)

Figure 66. Experimental set-up of the electrodynamic shaker test

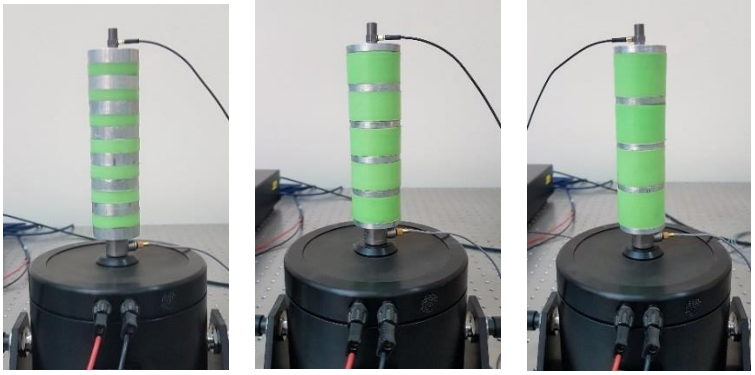

(a) Specimen A (b) Specimen B (c) Specimen C

Figure 67. Vibration shaker experiment set-up for Specimens A, B, and C

4.2.3 Experimental results

The vibration transmission test was performed by applying a sine sweep signal (chirp) to the specimen, ranging from 1 to 1200 Hz. The frequency response functions were determined from the Fourier transform ratio of the output acceleration and the input force of the signal. The FRF for Specimens A, B, and C are shown in Figure 68. The drop in the frequency response shown in Figure 68 represents the attenuation effect, which occurs at different frequencies depending on the specimen's geometry.

As illustrated in Figure 68a, starting from a frequency of 750 Hz, the FRF has dropped, signaling the start of the low vibration transmission zone for Specimen A. The observed low vibration transmission zone continues to 1200 Hz. For Specimen B, a low vibration transmission zone starting from 600 to 1200 Hz was observed. Specimen C exhibited a low vibration transmission zone between 700 and 1200 Hz. The attenuation behavior observed in these specimens is caused by the Bragg scattering effect that occurs when interposing two materials with mismatching impedances and by the inherent damping properties of the viscoelastic material [37].

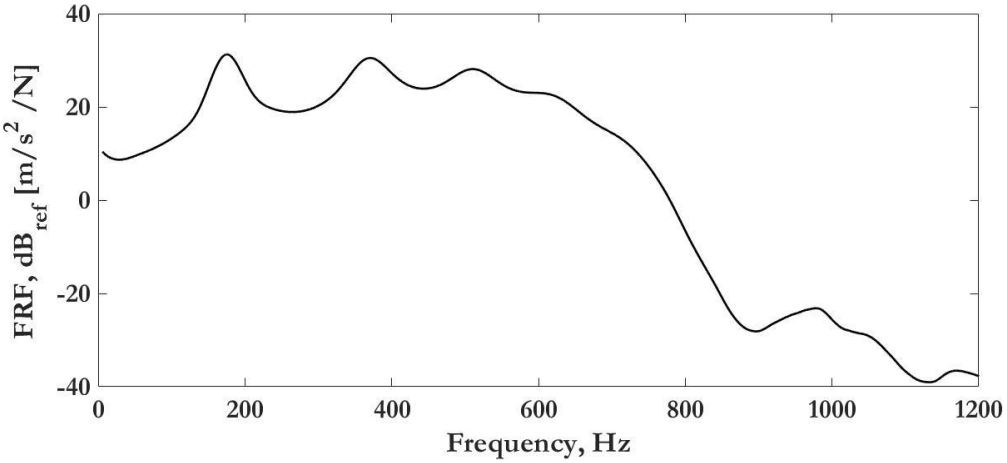

a) Specimen A

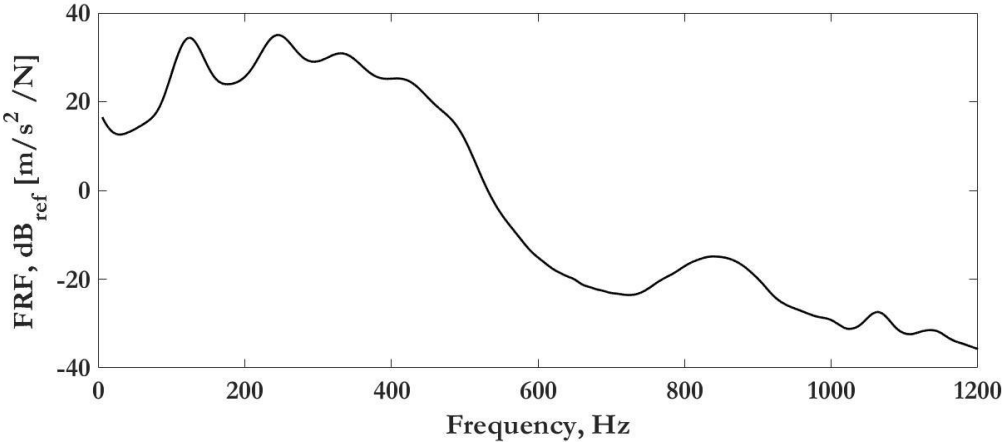

b) Specimen B

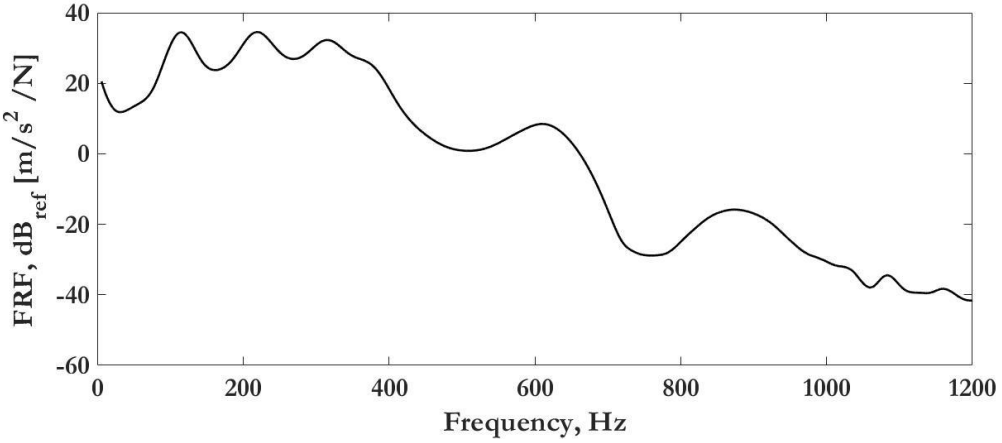

c) Specimen C

Figure 68. Frequency response function of specimens A, B, and C

The vibration attenuation behavior shown in the experimental results confirms that

using viscoelastic materials as a component in MMs helps to lower and widen the low vibration transmission frequency zone. Specimens A, B, and C have filling fractions of 1, 0.25, and 0.16, respectively. The earliest low transmission zone is observed in the FRF of Specimen B with a 0.25 filling fraction. This behavior can be clarified by examining the wavelength in the layered materials at the low transmission zone's starting frequency. Bragg-type band gaps typically occur at wavelengths of the order of multiples of unit cell length [122]. The wavelength depends on the phase velocities of the two constituting materials and the wave frequency [123]. At a certain frequency, the wavelength is comparable to the lattice constant L, leading to a frequency band where waves cease to propagate. The experimental results are used in the following section to validate the FE model.

4.3 Numerical modeling

Three axisymmetric FE models representing the three MM specimens were developed in Abaqus [124], as illustrated in Figure 69. Axisymmetric models were used in this chapter to make the analysis and the subsequent optimization iterations computationally feasible. Moreover, axisymmetric analysis has been successfully used to accurately model MM structures [22,121]. The three FE models were used to obtain the harmonic response of the viscoelastic MM specimens to harmonic excitation in the longitudinal direction. All three axisymmetric models had a width of 20 mm (the radius of the cylindrical specimen).

A steady-state harmonic analysis was performed within 1 to 1200 Hz. The response of the model was computed in the frequency domain under harmonic vertical excitation (mimicking the experimental setup of Section 4.2). The vertical loading was applied at the central input node of the lower layer, as illustrated in Figure 69. The vertical acceleration response was computed at the upper central node of the

upper layer, as also illustrated in Figure 69.

The specimen is represented as a free model at both ends subjected to an oscillatory chirp force at one end (the input node in Figure 69). This investigation aimed to develop a reliable numerical alternative to laboratory testing, which could be used in the optimization process. The axisymmetric element CAX8RH (an eight-node biquadratic axisymmetric quadrilateral hybrid element) was chosen with a 1.25 mm mesh for both materials (i.e., metal and polymer). A mesh refinement study confirmed that the 1.25 mm mesh size was sufficiently small to accurately model the dynamics of the model as illustrated in Figure 70. The linear elastic model was considered for the aluminum alloy, while the viscoelastic material model in Abaqus [124] was adopted to simulate the frequency-dependent behavior of the polymer in small steady-state harmonic oscillations. The dissipative part of the material's behavior was defined by providing the real and imaginary parts of the frequency-dependent shear and bulk modulus. The moduli were defined as functions of the frequency by a Prony series expression for the shear and bulk relaxation moduli, as discussed earlier in Section 4.2.1.

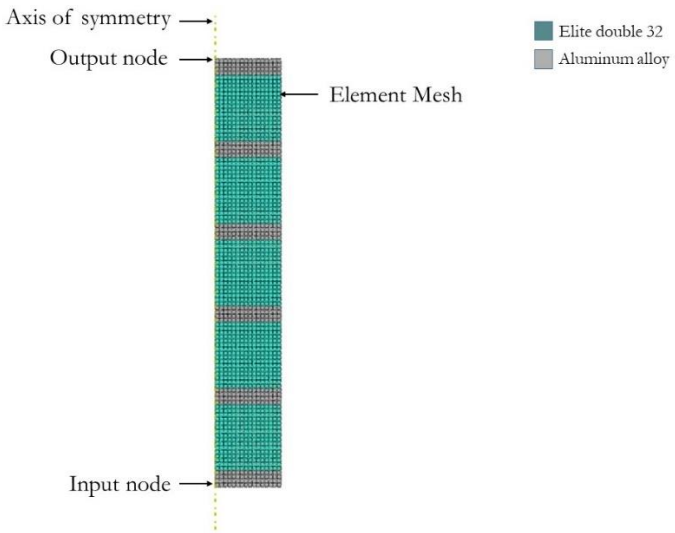

Figure 69. MM axisymmetric specimen FE model, specimen B

The experimental FRFs for Specimens A, B, and C were compared to the numerically predicted FRFs in Figure 71. For the three specimens, there was good agreement between the experimental and numerical FRFs, especially in the range of 1-900 Hz. Moreover, the numerical results corresponded well with the vibration attenuation behavior of the experimental results. This provided confidence to proceed with the optimization of the MM crystal. A MATLAB code was written to generate an FE model (in Abaqus [125]) of the MM from any set of parameters (lattice constant and the metal layer thickness). In addition to the aforementioned optimization parameters (L, a_1), the FE model also included the following parameters to comprehensively describe the specimen: total length, the radius of the specimen and the material properties. Details about the optimization parameters and routines are described in Section 4.4.

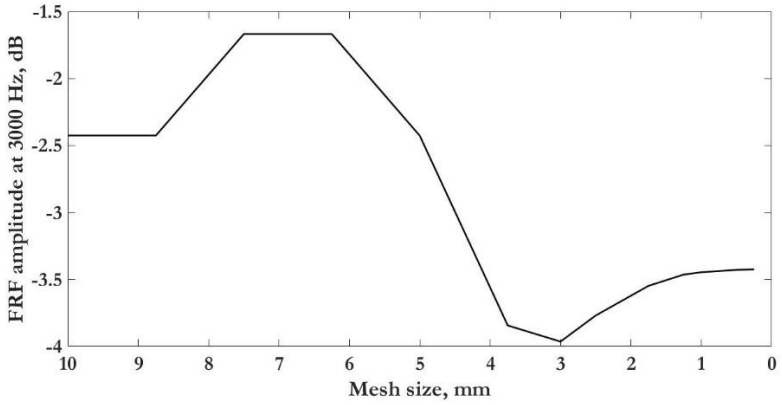

Figure 70. FEM mesh convergence study

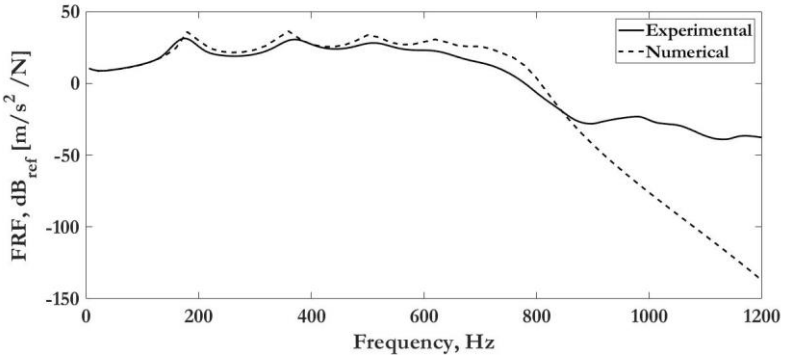

a) Specimen A

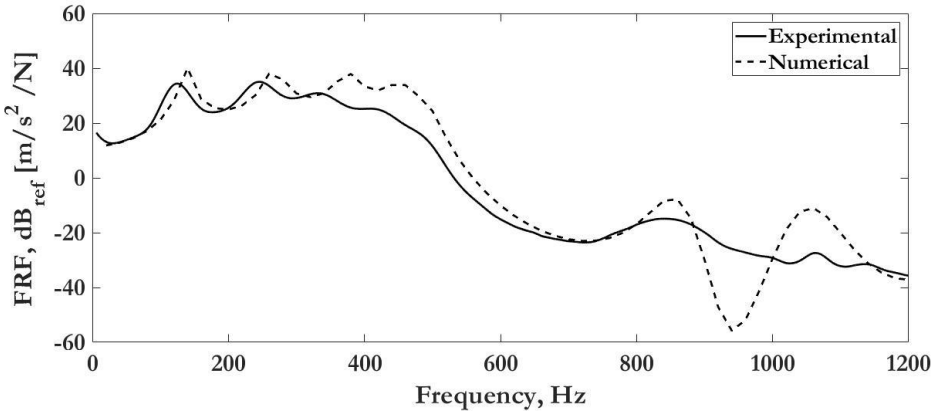

b) Specimen B

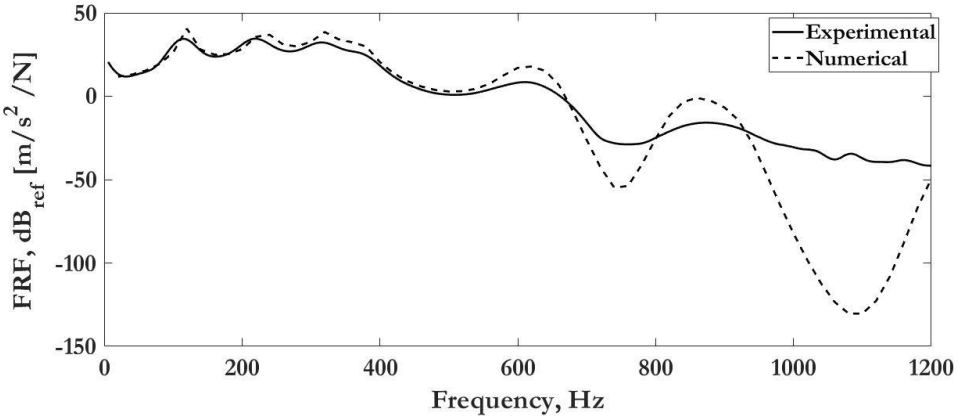

c) Specimen C

Figure 71. Comparison of the numerical and experimental transfer functions of specimens A, B, and C

4.4 The optimization Process

4.4.1 Optimization parameters

For the total thickness of $T = 160$ mm, a cylindrical MM with a diameter of 40 mm was optimized to obtain the minimum longitudinal wave transmission in the low-frequency range of 450-650 Hz. The optimization parameters used in this study were the thickness of the aluminum layer, a_1, and the lattice constant, L (see Figure 64). Different configurations of lattice constants and fraction ratios were possible for the maximum 160 mm thickness.

4.4.2 Optimization algorithm and fitness function

The multiobjective GA optimization presented in this section aimed to maximize the vibration attenuation of viscoelastic MM crystals in the frequency range between 450-650 Hz, while simultaneously minimizing the mass of the MM crystal. The fitness function of the proposed optimization process exhibits two cost functions. The first, C_1, indicates the mass of the MM crystal, and is calculated as follows:

$$C_1 = (n+1)\pi r^2 a_1 \rho_1 + n\pi r^2 (L - a_1)\rho_2 \quad (12)$$

where n is the number of cells, r is the radius of the specimen, and ρ_1 and ρ_2 are the aluminum and rubber densities, respectively (given in Table 11). The second cost C_2 represents the vibration attenuation performance within a specific frequency range. This is evaluated as the numerical integration of the FRF of the MM Crystal in the frequency range of 450-650 Hz.

A MATLAB routine was written to act as the fitness function of this multiobjective optimization process. According to the inputs (i.e., dimensions and construction of the specimen), the routine generates an Abaqus FE model of the corresponding crystal and analyzes it to compute the FRF between the output acceleration and the input force of the signal within the desired frequency range. The cost C_2 is then calculated as the area under the FRF amplitude curve by numerical integration using the trapezoidal rule. The objective of the multiobjective GA is to minimize both C_1 and C_2 within the specified frequency range at different masses. The optimization process is illustrated in Figure 72.

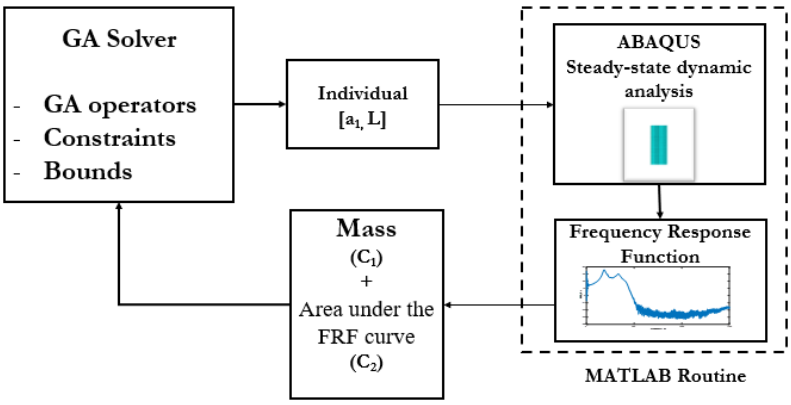

Figure 72. Layout of the optimization algorithm process

The optimization parameters were defined along with their value ranges, nonlinear constraints, and the fitness function that evaluates the individuals. The GA optimization [114] was used here because of its ability to search for the optimum solution from multiple points, thus making it likely to find the global optima without getting stuck around a locally optimal solution. They are also applicable to problems with linear and nonlinear constraints. In this study, two linear constraints, and one nonlinear constraint are described in Equation 13 and Equation 14, respectively.

The upper and lower bounds of the optimization parameters a_1 and L were selected in accordance with the geometry of the MM. The optimal specimen should contain at least two layers of aluminum; the smallest material thickness that can be manufactured is 5 mm. Moreover, a proportion of $n + 1$ aluminum pieces for every n polymer piece was adopted to maintain the MM's periodicity and to ensure that the first and last layers of the specimen were made of aluminum so that the specimen can be installed on the shaker for testing. The following linear constraints were introduced to ensure a minimum aluminum layer thickness of 5 mm and that the maximum unit cell's thickness of the MM was 150 mm (see Figure 64):

$$\begin{bmatrix} 1 & -1 \\ 1 & 1 \end{bmatrix} \begin{bmatrix} L \\ a_1 \end{bmatrix} \leq \begin{bmatrix} 0.005\ \text{m} \\ 0.16\ \text{m} \end{bmatrix} \tag{13}$$

A nonlinear constraint was imposed to ensure that the optimization process yielded a MM crystal that did not exceed the maximum total thickness T. The constraint could be written as follows:

$$(\text{floor}\left[\frac{T-a_1}{\text{L}}\right]) * L + a_1 \leq T\ , \qquad (14)$$

where $floor\left[\frac{T-a_1}{L}\right]$ represents the number of periodic cells that can fit within the maximum total thickness T, making sure that both the first and last layers of the specimen were made of aluminum.

The GA solver available in MATLAB's GA toolbox [125] was used to generate the initial population, evaluate the individuals and apply the genetic operators (selection, crossover, and mutation). The first generation was randomly generated in accordance with the bounds and constraints. The population size was chosen as 50 individuals, for the two parameters. With a large population size, the GA searches the solution space more thoroughly, thereby reducing the chance that the algorithm returns a local rather than a global minimum. However, a large population may not be useful, since it leads to a large probability of finding locally optimal individuals [126].

4.5 Optimization results and discussion

The multiobjective optimization process explained in Section 4.4 was conducted to obtain optimal viscoelastic MMs within the frequency range of 450-650 Hz. The GA process took 139 generations to converge to the results illustrated in Table 14. The optimization was repeated three times with different initial populations, and it converged to the same values every time. The results of this optimization are presented in Figure 73 as a Pareto front. An optimal specimen from the Pareto front is then selected given that it achieves a good vibration attenuation with a relatively low mass. The optimal specimen (red circled in the Pareto front) is composed of a 24 mm layer of the polymer (Elite Double 32) and 24 mm layers of aluminum for two-unit cells.

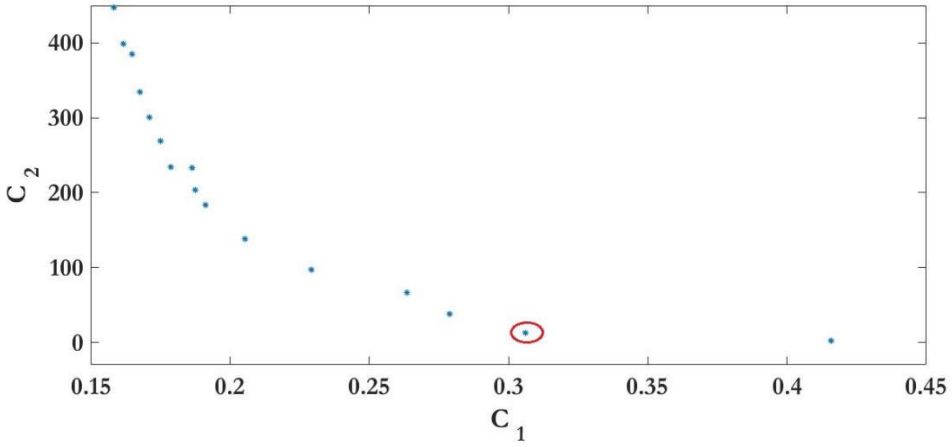

Figure 73. Pareto front for the multiobjective optimizations – the circled point represents the optimal specimen selected

Table 14. Configuration of the optimal specimen

	Aluminum Alloy	Elite Double 32
Layer thickness	23 mm	24 mm
Number of layers	3	2

The optimal specimen was manufactured and tested experimentally using the electrodynamic shaker as shown in

Figure 74.

Figure 75 shows a comparison between the numerical and experimental FRF of the optimal specimen. There is a good agreement between the experimental and numerical results, which demonstrates the validity of this approach. Slight differences might be caused by the manufacturing imperfections relating to how precisely the aluminum was cut, the preparation and uniformity of the polymer's molding.

Observation of the attenuation behavior of the FRF of the optimal specimen shows that the proposed optimization has considerably improved the vibration control capabilities of the MM by tuning its topology within the 450-650 Hz range. Figure 76

shows the experimental FRFs of the (optimal and control) specimens. The transmission behavior of the optimal specimen presents an earlier attenuation at lower frequencies compared to the control specimens, as shown in Figure 76. The optimal specimen performed significantly better than the control specimens in vibration attenuation in the 450-650 Hz range. It is important to note that the optimal sample (0.306 kg) provided a better attenuation performance than specimen A (0.373 kg), despite being much lighter in mass. This highlights the efficiency of the proposed multiobjective optimization process in maximizing vibration suppression while keeping the mass as low as possible.

As stated in section 4.4, the total thickness of any specimen in this study should not have exceeded 160 mm. All specimens compared in Figure 76 satisfied this constraint. The optimal sample had the lowest total thickness with a higher lattice constant. It is important to note that the desired low transmission zone was achieved using the optimal sample with less amount of material.

Figure 77 shows the deformation magnitude of the optimal sample within a transmission zone (Figure 77a) and a low transmission zone (Figure 77b). The response at the top of the specimen within the low transmission zone is significantly lower than that computed at the transmission zone which further demonstrates that the optimized specimen is effective in reducing vibration transmission.

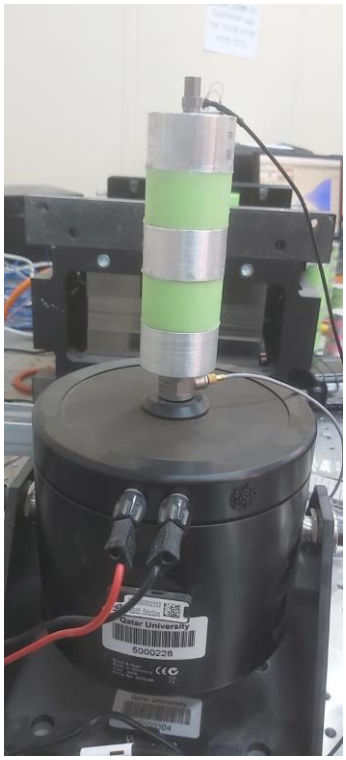

Figure 74. Vibration shaker experiment set-up for the optimal specimen

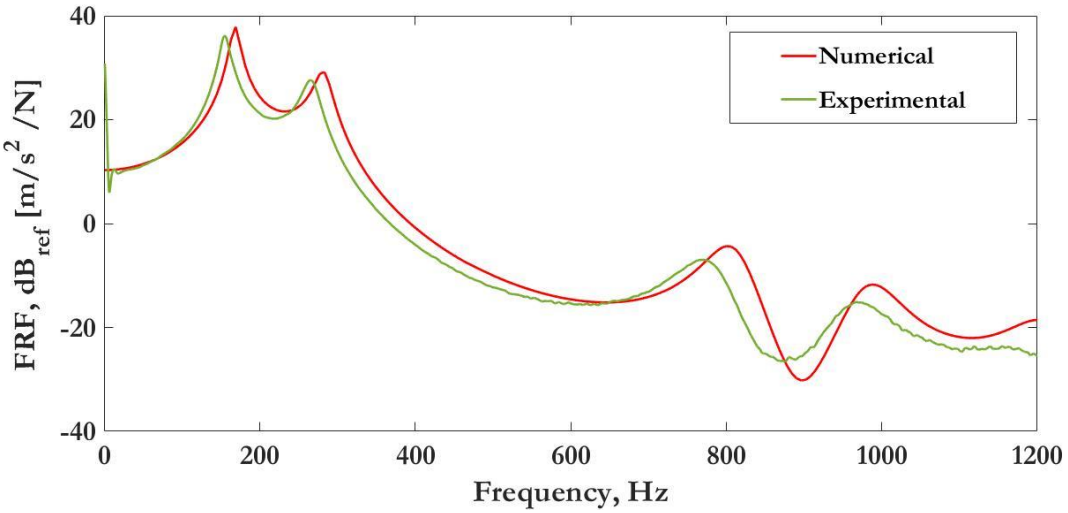

Figure 75 . Comparison of the numerical and experimental transfer function of the optimal specimen

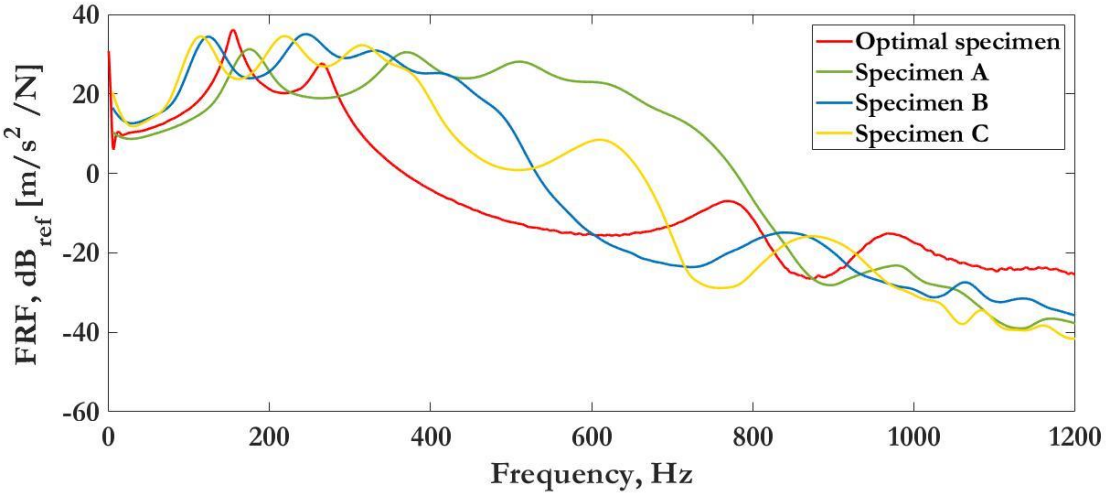

Figure 76. Comparison between the experimental frequency response functions (FRFs) of the optimal and control specimens

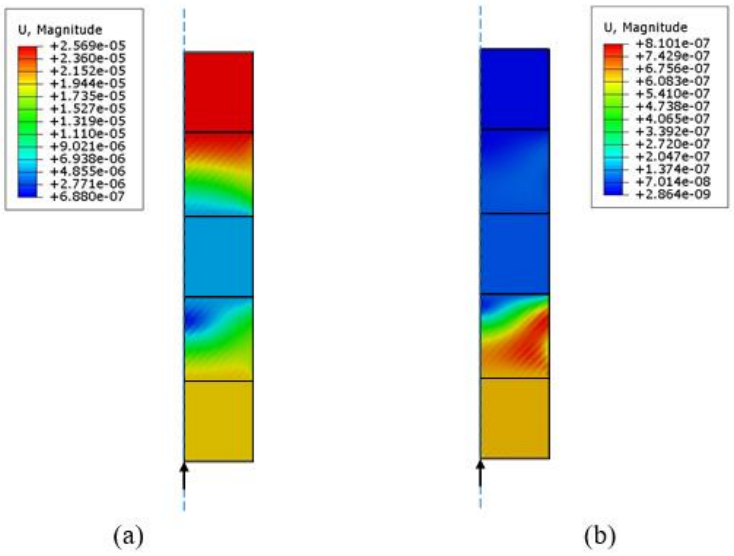

Figure 77. Displacement magnitude (in mm) of the optimal MM under a harmonic load. (a) Within a transmission zone (150 Hz). (b) Within a low transmission zone (600 Hz). The arrow represents the applied load, and the dashed line represents the axis of symmetry of the axisymmetric FE model

4.6 Conclusion

Metamaterials (MMs) are composites that are artificially engineered to have unconventional mechanical properties that stem from their microstructural geometry rather than from their chemical composition. Several studies have shown the effectiveness of viscoelastic MMs in vibration attenuation due to their inherent vibration dissipation properties and the Bragg scattering effect. This chapter has presented a multiobjective optimization based on genetic algorithms (GA) that aims to find a viscoelastic MM crystal with the highest vibration attenuation in a chosen low-frequency range. A multiobjective optimization has allowed consideration of the attenuation due to the MM inertia versus the Bragg scattering effect resulting from the periodicity of the MM. The investigated parameters that influenced wave transmission in a one-dimensional MM crystal included the lattice constant, the number of cells and the layers' thickness. Experimental testing and finite element analysis were used to support the optimization procedure. An electrodynamic shaker was used to measure the vibration transmission of three control specimens and the optimal specimen in the frequency range 1-1200 Hz. The following conclusions can be drawn from this study:

- The FE models developed in this chapter provided a reasonable prediction of vibration attenuation of one-dimensional metamaterials (MM) compared with the experimental results.
- The multiobjective optimization algorithm developed in this chapter successfully generated an optimal specimen whose low transmission zones have been validated numerically and experimentally. Thus, this algorithm could be considered reliable. The validated optimization algorithm could be

used in future research to investigate a wider range of parameters.

- The resulting optimal specimens performed better than the control specimens in their respective frequency ranges without being of massive weight.

Finally, the proposed methodology in this chapter showed a promising potential to be used in investigating the behavior of MMs at higher frequency ranges, given that the proposed model is based on the higher frequency behavior of this material.

CHAPTER 5: PLATE METASTRUCTURE FOR TARGETED LOW-FREQUENCY VIBRATION SUPPRESSION

5.1 Introduction

While the Bragg scattering effect in 1D, 2D, and 3D metamaterials explains the occurrence of frequency band gaps in periodically changing materials, the center of the lowest frequency gap is about twice the lattice constant. Thus, the occurrence of the low transmission zone depends on the properties of the constituting material and the structural configuration of the sample. An alternative approach to vibration suppression is using local resonances which was first proposed by Liu [1]. Locally resonant materials or substructures may comprise a matrix and scatterers that resonate and interact with the host structure's long-wavelengths, thus restricting the transmission of the waves along the host structure. The local resonance low-frequency zones depend on the resonant material's natural frequency and design. Different resonant materials have been proposed to achieve this effect. One of these approaches is the use of single degree of freedom (SDOF) oscillators. The inclusion of vibration dissipating components to a host structure permits the reduction of vibration transmission within the desired frequency range while ensuring the continued performance of the host structure's original function.

Many studies used SDOF oscillators for attenuating vibration in beams [127–129]. Those studies have shown that SDOF oscillators indeed contribute to vibration attenuation and that the low transmission zone depends on the resonating frequency of the inserted oscillator. Recently, zigzag inserts gained interest in the field of passive structural vibration attenuation. For example, Hobeck and Inman [130] demonstrated experimentally that cantilevered zigzag structures have lower natural frequencies. The low transmission zone generated by zigzag inserts occurs in the low-frequency range

which might apply to ambient vibration reduction. Besides, Essink et al. [131] and Karami and Inman [132] have proposed structures with zigzag inserts for energy harvesting. More recently, Abdeldjaber et al. [133] proposed a closed-form approach to optimize the vibration attenuation of a zigzag metastructure. Numerical work on modeling the zigzag inserts assumes that the zigzag inserts are cantilevered with no interaction with the host structure. There is a lack of experimental results studying the geometric nonlinearity on zigzag metastructures and focusing on vibration attenuation with minimum intervention on the host structure.

In this chapter, the aim is to develop a genetic algorithm optimization of zigzag inserts for an optimal zigzag mass and stiffness and location in two types of thin cantilever plates. The objective of the optimization is to incorporate optimal inserts to attenuate vibration in a specific frequency range and consequently transform the resonance frequency band around the plate natural frequency to a low transmission zone. The effectiveness of the proposed optimization is demonstrated numerically and experimentally.

5.2 Experimental testing

Experiments were performed on thin Aluminum plates with embedded zigzags (Figure 78). A LaserJet Cutting Machine was used to cut the zigzags out of the plate. A tip mass was placed at the free end of the zigzag. The plates were clamped to a horizontal direction shaker which would excite the plate at its base in the direction perpendicular to its plane. An APS 400 exciter was used due to its suitability for low-frequency investigations and placed over a passive optical table (Model T46H-PTP602, Thorlabs) to be isolated from ambient vibrations. Two accelerometers were used to record the input and output signals, namely a miniature accelerometer (Type 4394 piezoelectric CCLD accelerometer, Brüel & Kjær) and a Piezoelectric

Accelerometer, TEDS (Type 8344, Brüel & Kjær), respectively. The input and the output accelerometers were placed on points i and j of the plate, respectively (Figure 79). A swept sine signal ranging from 1 to 100 Hz was introduced and the base of the plate and the frequency response function (FRF) was determined from the Fourier transform ratio of the output and the input acceleration signal. A schematic on the experimental setup is in Figure 80.

Two types of aluminum plates were considered for optimization namely plate P1 and P2. Details on plates P1 and P2 geometries are found in Table 15. Two control plates (R1, R2) with randomly placed zigzags and tip masses weights (Table 15) were tested along with P1 and P2 for vibration transmission. The tested specimens are shown in Figure 81 and the zigzag dimensions are detailed in Table 16 and Figure 82.

Figure 78. Experimental shaker setup of the Aluminum plate with cutout zigzag

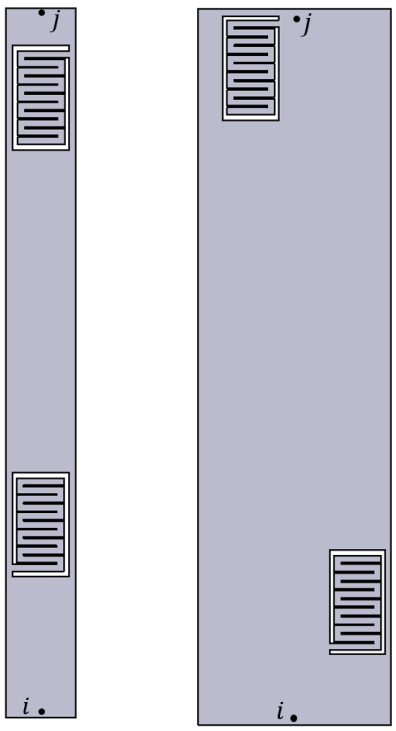

Figure 79. Aluminum plate with cutout zigzags

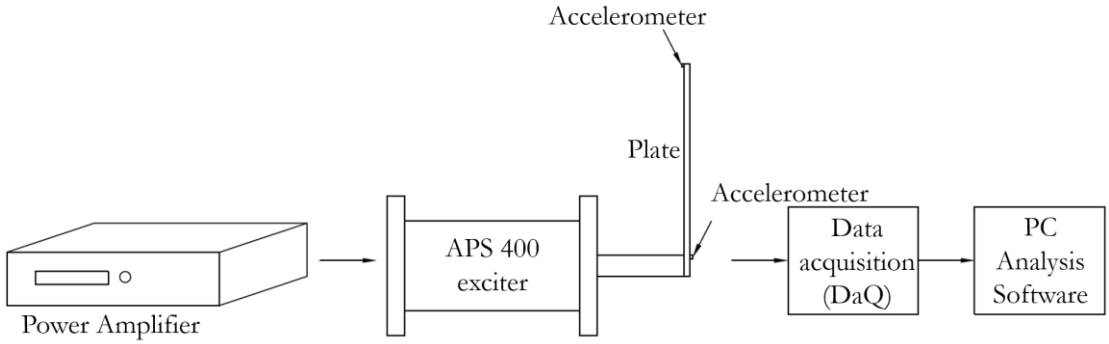

Figure 80. Schematic of the Plate shaker test

Table 15. Testing matrix

Specimen name	Plate Size H*W*T (mm)	Cutout zigzag location (mm)		Tip masses (g)
		Zigzag 1	Zigzag 2	
Case 1				
P1	500x49x3	-		-
R1	500x49x3	99.10		400
Case 2				
P2	500x135x3	-		-
R2	500x135x3	(91.9, 9.3)		(17.3, 382.1)

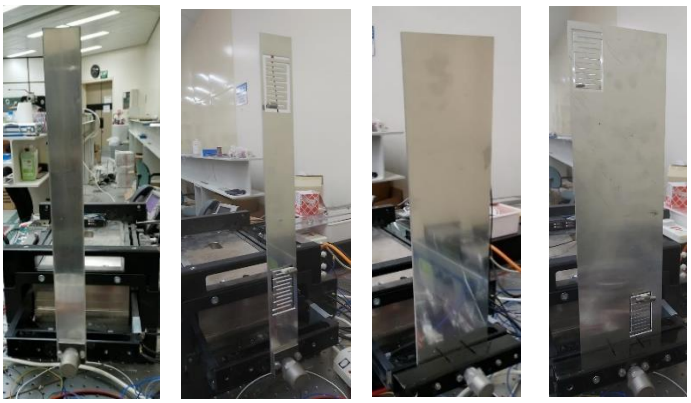

(A) (B) (C) (D)

Figure 81. Plate Specimens

Table 16. Zigzag dimensions

Zigzag parameters	Values
α-beam length	28 mm
α-beam width	5 mm
β-beam length	6.1 mm
β-beam width	5 mm
Number of α-beams	11

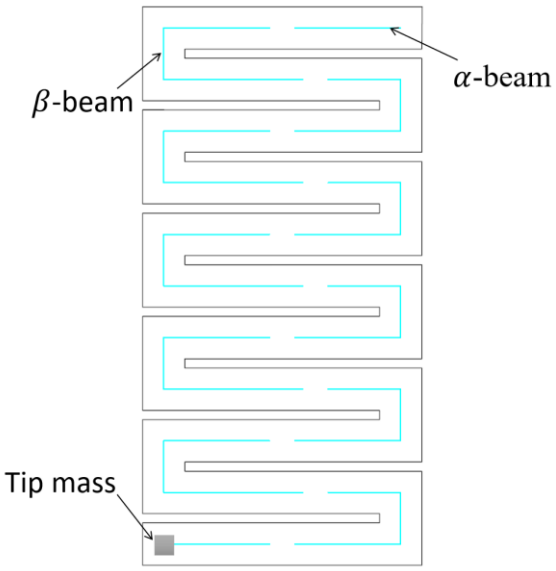

Figure 82. Description of the zigzag geometry

The FRFs of the specimens P1, R1, P2, R2 were plotted in Figure 83 (A-D), respectively. Figure 83A shows that first two flexural modes of P1 are around 10 and 67 Hz. Plate R1 were obtained by cutting out two zigzags (at random locations) in P1 and adding tip masses to the free ends of the zigzags. Results demonstrate that the first two flexural modes of R1 are around 6.5 and 64 Hz, which is slightly lower that their corresponding counterparts in P1 as shown in Figure 83B. This is expected due to the reduction in mass and stiffness resulting from cutting out material to construct the zigzags. Two peaks around 48 and 57 Hz emerged in R1 (Figure 83B); these two peaks correspond to the two random cut zigzags allowing the formation of a low transmission zone around 52 Hz. In Figure 83C the first two flexural modes of P2 are around 10 and 69 Hz. Plate R2 was obtained by cutting out two zigzags (at random locations) in P2 and adding tip masses to the free ends of the zigzags. Results show that the first flexural mode of R2 is around 6.5 Hz, which is similar to its corresponding counterpart in P2 as shown in Figure 83D. This is due to the large size of the plate compared to the cut zigzags. Two peaks around 43 and 72 Hz emerged in R2 (Figure 83D); these two peaks correspond to the two random cut zigzags allowing

the formation of two narrow low transmission zones around 43 and 72 Hz. Adding two zigzags with masses allowed maintenance of a minimum intervention to the host structure, however to obtain a low transmission frequency zone using two zigzags required optimization on the position of the zigzags and their tip masses. Experimental results of the two random plates with zigzags show that two zigzag cutouts can develop low transmission zones in the low-frequency zone without significantly affecting the stiffness and mass of the host plate.

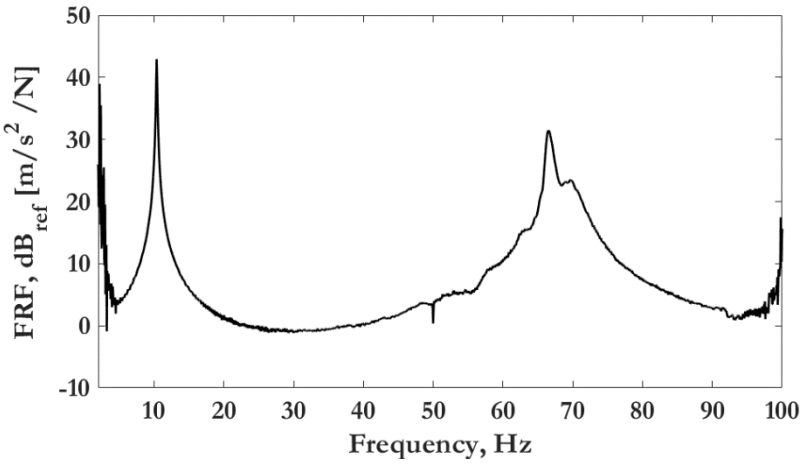

(A)

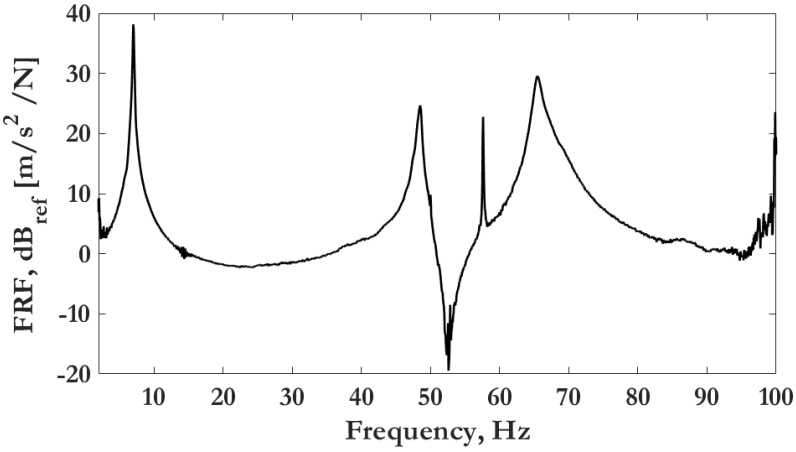

(B)

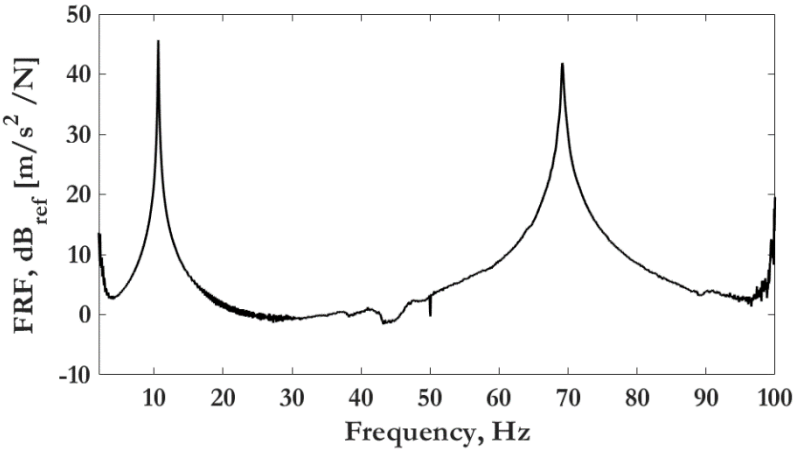

(C)

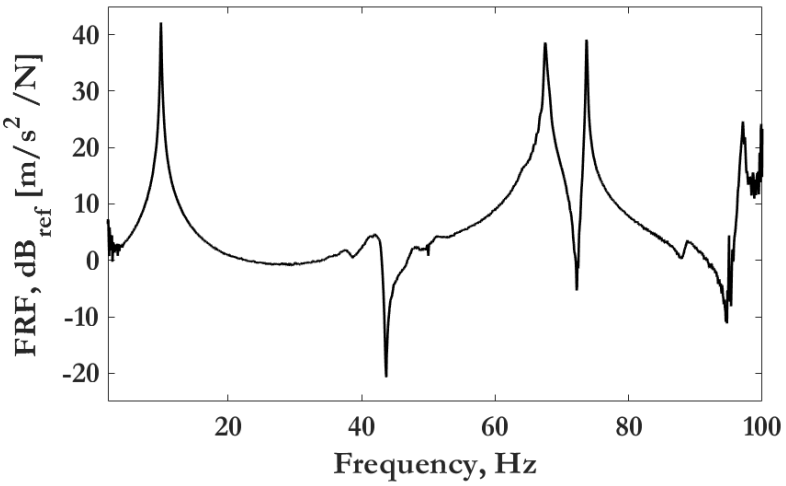

(D)

Figure 83. Experimental Frequency response function for Case1: (A) Plain plate P1 (B) Random plate R1, Case 2: (C) Plain Plate P2 (D) Random plate R2

5.3. Numerical modeling

Multiple FE models representing the different plates in this chapter have been developed in Ansys [134], as illustrated in Figure 84. The FE simulations were used to obtain the frequency response function of the aluminum plates by subsequently running a modal analysis rather than a harmonic analysis on the 1-100 Hz frequency range. The response of the model was computed in the frequency domain under harmonic excitation, mimicking the experimental setup described in section 5.2. The output was calculated at j the upper central node as illustrated in Figure 79. The lower

side of the plate was subjected to a fixed boundary condition. This simulation developed a reliable numerical solution that could be used in the optimization process. The model was meshed with element SHELL281 with eight nodes with six degrees of freedom at each node. A mesh convergence study was performed and appropriate refinements around the zigzags were implemented. The linear elastic model was considered for the aluminum plate with elastic modulus of 72 GPa and a 2700 kg/m^3 density.

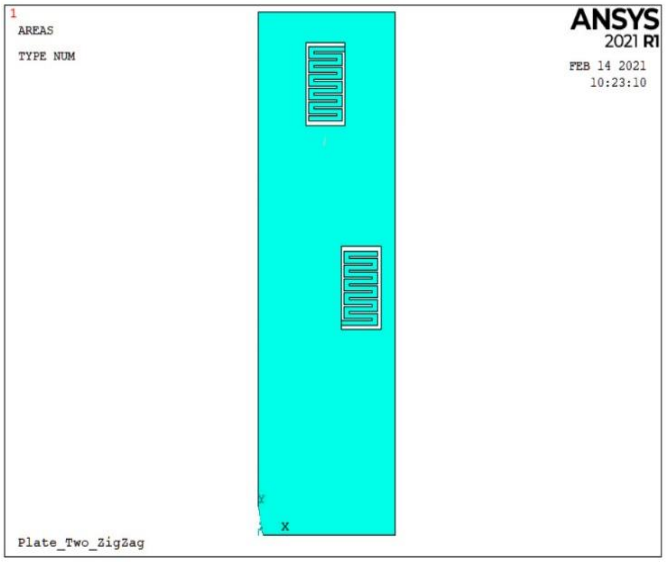

Figure 84. Plate with zigzag cutouts FE model

The numerical FRFs of specimens A to D are plotted in Figure 85. There is good agreement between the experimental FRFs and the numerical FRFs in Figure 85. The numerical results obtained in this section provided confidence to proceed with the optimization of the plate with zigzag cutouts. A MATLAB code was then written to generate an FE model (in Ansys) of the plate from any set of parameters (position of the zigzag and the tip mass). Other parameters we kept constant in the FE model such as the geometry of the plate and the material properties. The optimization parameters and codes are described in section 5.4.

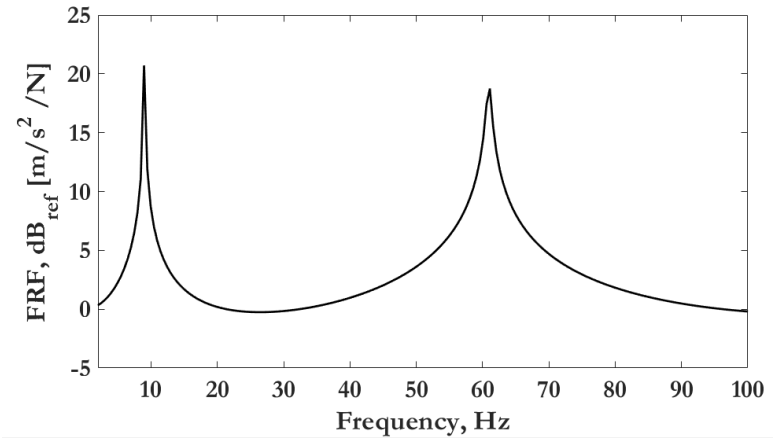
FRF, dB ref [m/s 2 /N]
Frequency, Hz

(A)

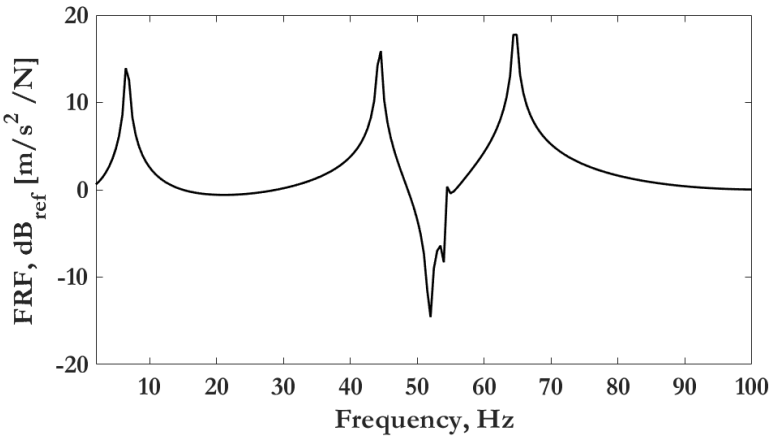
FRF, dB ref [m/s 2 /N]
Frequency, Hz

(B)

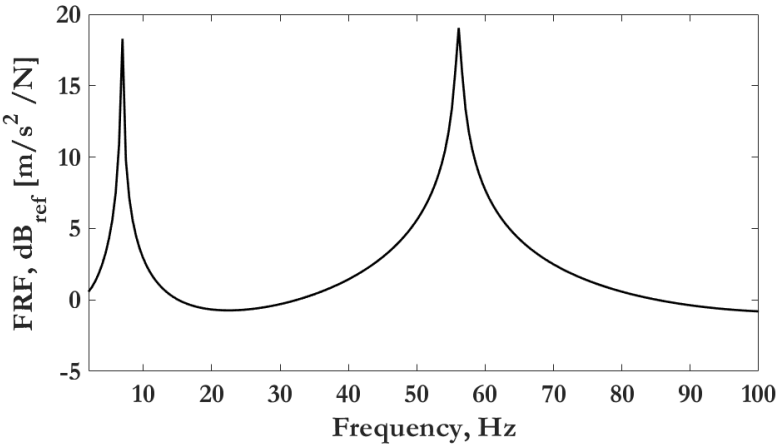
FRF, dB ref [m/s 2 /N]
Frequency, Hz

(C)

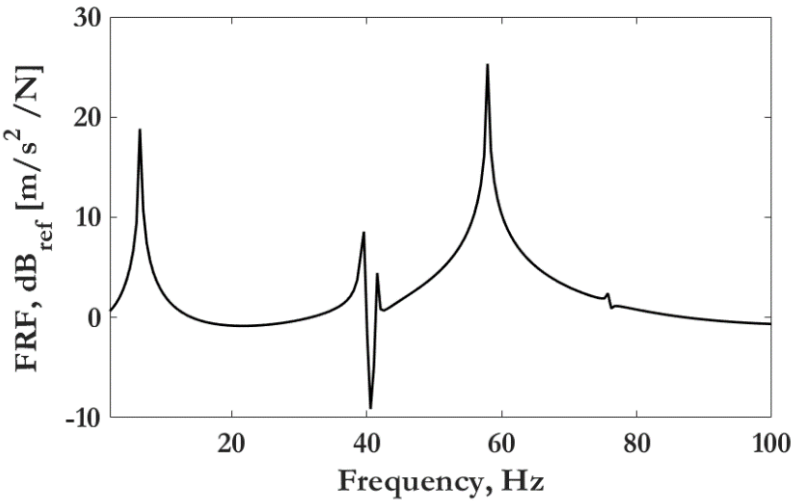

(D)

Figure 85. Numerical Frequency response functions for specimens for Case1: (A) Plain plate P1 (B) Random plate R1, Case 2: (C) Plain Plate P2 (D) Random plate R2

5.4 Optimization process

5.4.1 Optimization parameters

Two optimizations were run for two plates P1 and P2, these two cases were called case 1 and case 2, respectively. The plates in cases 1 and 2 were optimized to minimize wave transmission in the low-frequency range of 60-80 Hz due to their resonance at this range as shown in Figure 83 (A and C). The optimization parameters for both cases were the location of the zigzags and the weight of the tip masses. The location of the zigzag was determined by (x, y) where x and y were the coordinates of the lower-left side of the zigzag opening as illustrated in Figure 86. The optimization parameters were:

- y_1, m_1, y_2, m_2 for the case 1 optimization
- $x_1, y_1, m_1, x_2, y_2, m_2$ for the case 2 optimization.

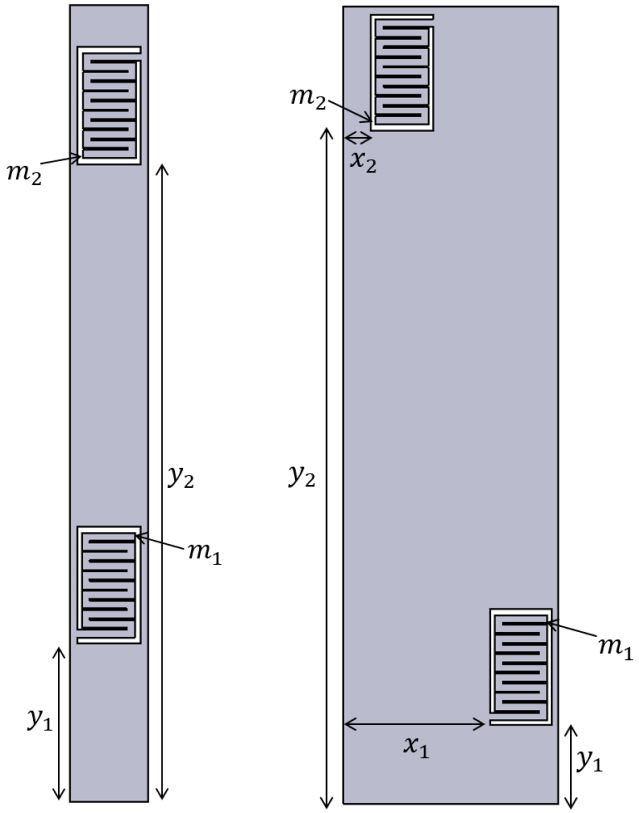

Figure 86. Optimization parameters (a) case 1 (b) case 2

5.4.2 Optimization algorithm and Fitness function

A Genetic algorithm (GA) optimization was performed in this study to minimize vibration transmission in the two cases of thin aluminum plates for the 60-80 Hz frequency range. The fitness value of the proposed optimization was the RMS of the 60-80 Hz FRF of the specimen. The closer the RMS was to zero the better vibration attenuation performance of the specimen. A MATLAB routine was written to act as a fitness function of the optimization. This routine generated an Ansys FE model of a plate with zigzags and returns the FRF between the output and input acceleration within the desired frequency range. The fitness value was the RMS of the FRF in the 60-80 Hz frequency range. The population size selected for this optimization was 20. The optimization process is detailed in Figure 87.

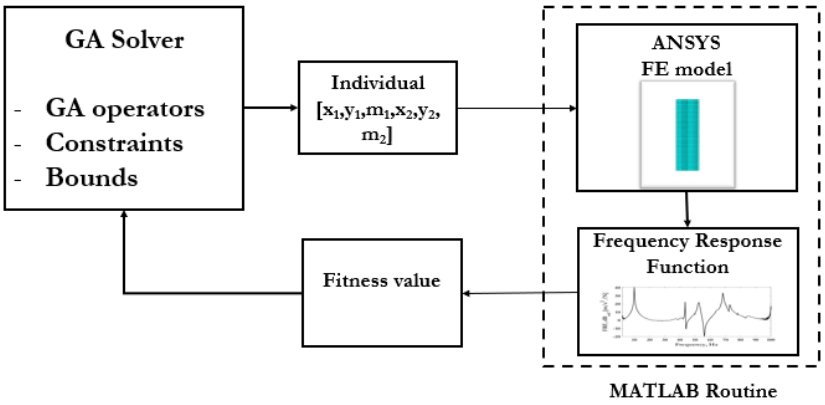

Figure 87. Layout of the optimization process

In this optimization, two linear constraints were imposed to the optimization. The first constraint ensured that the zigzag remained within the plate dimensions without being less than 2 mm distant from its edges for waterjet cutting feasibility. The second constraint ensured that the two zigzags did not interlope on each other's and remain 2 mm distant in both orthogonal directions. The tip masses were limited to 20 g for the masses volume to remain on the tip of the zigzag. These constraints are written in Equations 4.1 and 4.2.

$$\begin{bmatrix} 0.002 \\ 0.002 \\ 0.002 \\ 0.002 \\ 0 \\ 0 \end{bmatrix} \leq \begin{bmatrix} x_1 \\ x_2 \\ y_1 \\ y_2 \\ m_1 \\ m_2 \end{bmatrix} \leq \begin{bmatrix} W - w_z - 0.002 \\ W - w_z - 0.002 \\ H - h_z - 0.002 \\ H - h_z - 0.002 \\ 20 \\ 20 \end{bmatrix} \tag{15}$$

$$\begin{bmatrix} |x_1 - x_2| \\ |y_1 - y_2| \end{bmatrix} \leq \begin{bmatrix} w_z + 0.002 \\ h_z + 0.002 \end{bmatrix} \tag{16}$$

Where W is the total width of the plate, w_z is the width of the zigzag opening, H is the total height of the plate, h_z is the height of the zigzag opening.

5.5 Optimization results and discussion

5.5.1 Case 1 Plate

The first GA optimization runs for the 500*49*3 mm plate were conducted to get the

optimal plate within the 60-80 Hz frequency range. The optimization took 27 generations to converge to the optimal specimen illustrated in Figure 88 and detailed in Table 17. The optimal specimen was a plate with two zigzags around its middle section with 3.9 g and 13.4 g tip masses.

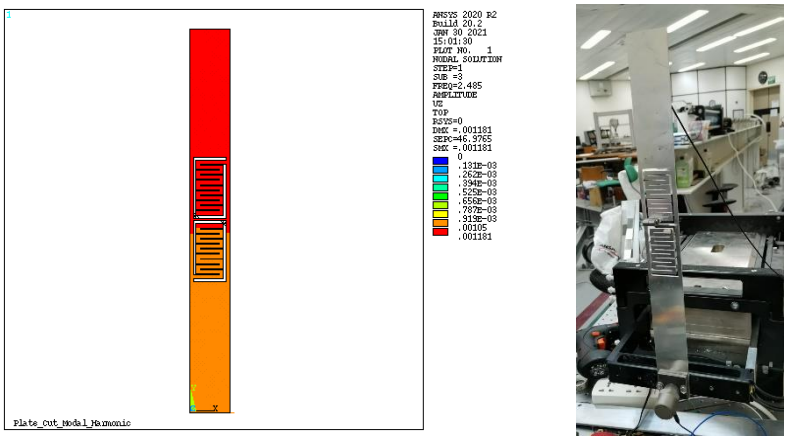

(a) (b)

Figure 88. Optimal specimen O1

Table 17. First optimization results

Optimization parameters	Optimal values
y_1	0.1588 m
y_2	0.2319 m
m_1	0.0039 kg
m_2	0.0134 kg

The optimal specimen O1 was prepared and tested in the experimental conditions described in section 5.2. Figure 89 shows the numerical and experimental FRFs comparison between the optimal specimen O1 and the plain plate P1. In the 60-80 Hz range, there is a clear low transmission zone replacing what was a resonance zone in the corresponding plain plate. The use of the Ansys finite element model in the optimization yielded an optimal specimen (O1) with satisfactory experimental FRF. The optimization of the case 1 plate is reliable.

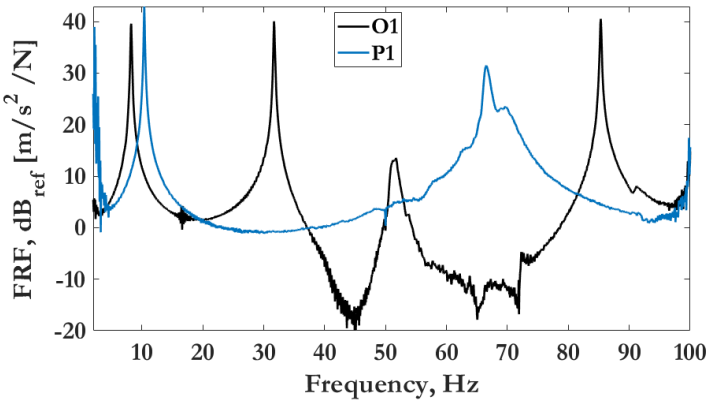

(A)

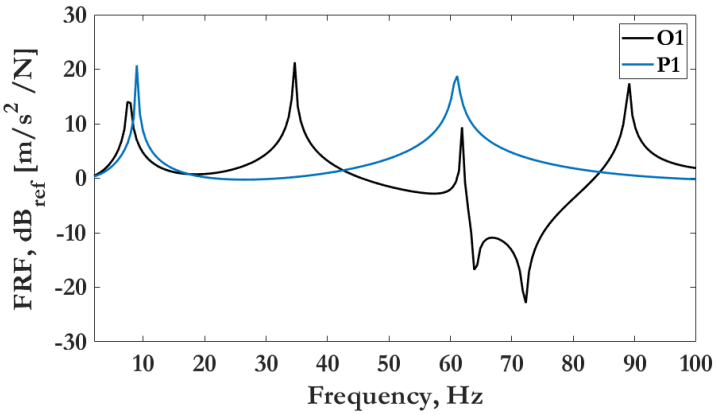

(B)

Figure 89. Comparison between the FRFs of the optimal specimen O1 and the corresponding plain plate P1 (A) Experimental (B) Numerical

5.5.2 Case 2 Plate

The second GA optimization for the 500*135*3 mm plate was conducted to get the optimal plate within the 60-80 Hz frequency range. The optimization took 36 generations to converge to the optimal specimen illustrated in Figure 90 and detailed in Table 18. The optimal specimen was a plate with two zigzags with 4 g and 7.3 g tip masses.

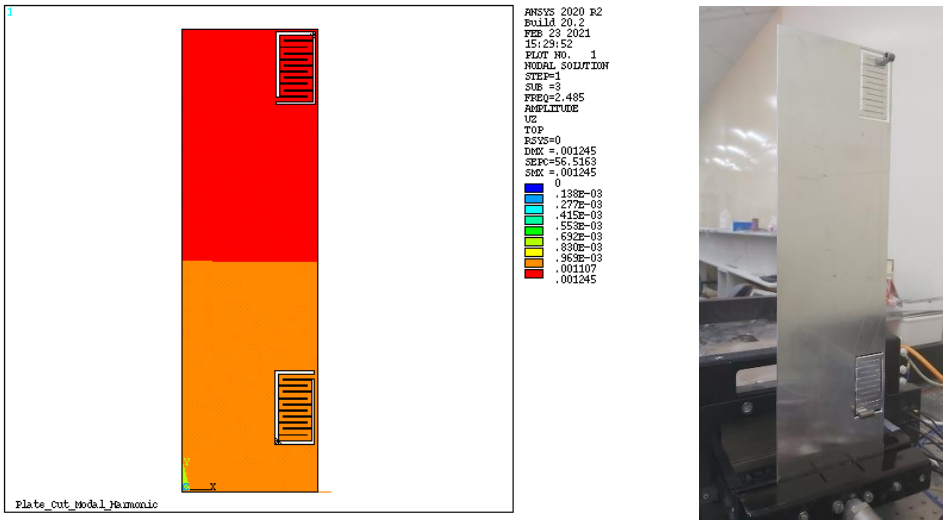

(a) (b)

Figure 90. Optimal specimen O2

Table 18. Second optimization results

Optimization parameters	Optimal values
x_1	0.093 m
x_2	0.093 m
y_1	0.385 m
y_2	0.0472 m
m_1	0.004 kg
m_2	0.0073 kg

The optimal specimen O2 was prepared and tested in the experimental conditions described in section 5.2. Figure 91 shows the numerical and experimental FRFs comparison between the optimal specimen O2 and the plain plate P2. Observing the 60-80 Hz range in Figure 91, two narrow low transmission zones appear around 60 and 70 Hz, replacing the high transmission zone in the corresponding plain plate. The use of the Ansys finite element model in the optimization yielded an optimal specimen (O2) with a satisfactory experimental FRF. The optimization of the case 2 plate is

reliable.

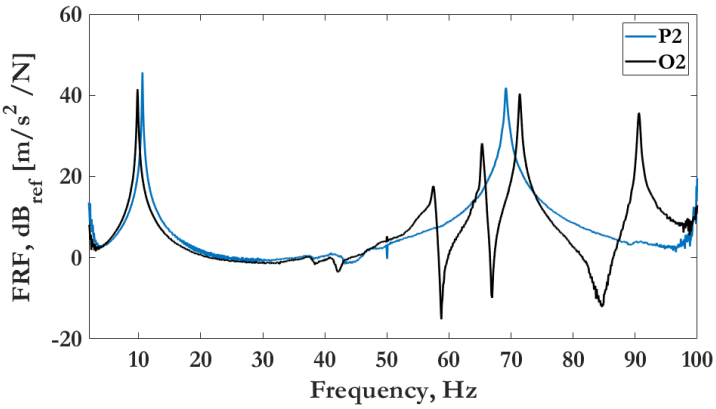

(A)

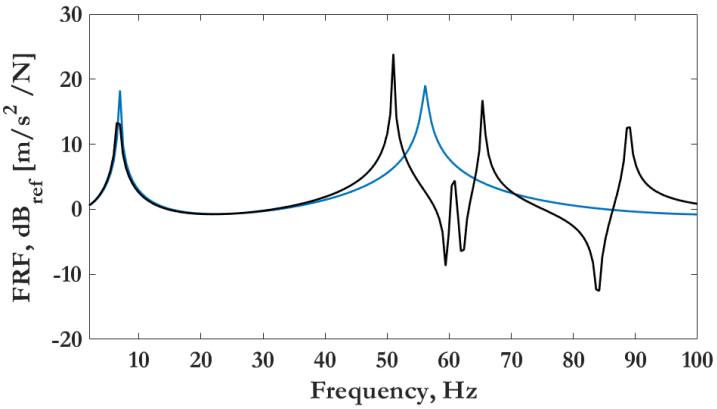

(B)

Figure 91. Comparison between the FRFs of the optimal specimen O2 and the corresponding plain plate P2 (A) Experimental (B) Numerical

5.6 Conclusion

For two-dimensional mechanical metamaterials, one of the most common vibration attenuation mechanisms is local resonance, where the resonant components in a host structure interact with the long wavelength traveling wave leading to wave transmission restrictions. In this study, zigzags resonating on an aluminum plate host structure were proposed to generate targeted low transmission zones with a minimum of structural intervention. Plain plates and plates with randomly located zigzags were tested experimentally using a vibration exciter and accelerometers. The comparison

between the plates with randomly located zigzags frequency responses and the corresponding plain plates showed that two zigzag cutouts could generate low transmission zones. When modeling the control specimens numerically, it was observed that there was a good agreement with the experimental FRF. The numerical model was then used as a fitness function for two genetic algorithm optimizations, the first with four parameters and the second with six parameters. The two optimal specimens obtained showed low transmission behavior in the targeted frequency range and a good agreement with the corresponding FRFs. Observing the comparison between the experimental FRFs of the optimal specimens showed that the optimization was reliable and could be used as a tool to tune the plate matching its structural dynamic service needs.

CHAPTER 6: WAVE PROPAGATION IN PERIODIC VISCOELASTIC COMPOSITE

6.1 Introduction

The importance of material behavior under dynamic loading conditions has prompted considerable effort towards the development of experimental equipment capable of deforming a vast array of smart materials at elevated strain rates. The shock tube is the ancestor of the Split Hopkinson Pressure Bar (SHPB). A shock tube is a simple device capable of producing a compressive loading pulse with a very short rise time, which is typically used to simulate blast waves. This compressive loading pulse is delivered in the form of a shock wave, which is a highly compressed volume of gas traveling with great speed. Shock tubes appear in both compression-driven and blast-driven varieties, producing shock waves through either a pressure differential or the detonation of a small explosive charge, respectively. A shock tube consists of a sealed tube at one end and separated into two sections by a thin layer of material. The sealed section is filled with pressurized air in the case of using the pressure-driven device, or some combustible gas in the case of using the blast-driven shock tube. Historically, these devices have seen great versatility in terms of use, having been used in the study of diverse areas including combustion, aerodynamic properties at high velocities, shock wave characteristics, and the response of structures and materials to blast loading.

The shock tube has been present in the scientific community for over a century. French scientist Paul Vielle is credited with the first use of a shock tube in 1899 while studying combustion and detonation in tubes [135,136]. This early shock tube utilized a small tube, approximately 22 mm in diameter, which held explosive gasses in a short chamber separated from the remainder of the 6-m long tube by a thin layer of

cellophane. The Cranz-Schardin camera, invented in 1929 [137], was used by Schardin in further experiments with blast-driven shock tubes in 1932 [138], utilizing the high-speed camera with imaging techniques to observe shock waves.

Shortly after World War II, Payman and Shepherd [139] developed a compression-driven shock tube in response to concerns regarding landmines in the UK. This apparatus required that one segment of the tube, sealed from the remainder with a thin sheet of copper, be pressurized until the copper ruptured. The pressure differential between the pressurized section and the remainder of the tube, which existed at atmospheric pressure, would then compress the inert gasses into a shock wave while driving them out of the tube. The compression-driven shock tube offers obvious benefits in terms of safety and ease of use and produces pressure pulses with much longer durations than those typically produced by actual explosions [138]. As a result, shock tubes utilized for material characterization are very often of the compression-driven type. The term “shock tube” also became prevalent in the years following WWII. With the first symposium on shock tubes, held in 1957 by the U.S. Navy and Air Force, the development of shock tubes had begun to mature [140].

Due to the increasing prevalence of blast-related damage and injuries in recent years, the shock tube apparatus has seen a substantial escalation in popularity as a means of investigating this phenomenon [67, 70]. Contemporary work exemplifies the capabilities of the shock tube as a preferred apparatus for examining the behavior of a wide variety of materials subjected to a number of dynamic loading stress states. This work ranges from metals subjected to bi-axial tension [141] to high-pressure blast testing of armor and combat material [142]. This versatility and capability regarding material testing, combined with the inherent safety of the device compared to the blast-driven counterpart, makes the compression-driven shock tube ideal for a

research environment. As such, this device was selected as an essential item for the dynamic material behavior research facility.

The Split Hopkinson Pressure Bar (SHPB), also known as Kolsky bar, was one of the first experiments established to conduct high strain rate testing and has since become one of the most widely used experimental methods for observing dynamic material behavior.

The development of the Split Hopkinson Pressure Bar (SHPB) apparatus began unknowingly, with numerous experiments performed by John Hopkinson in the early 1870s, in which he examined stress waves in iron wires [142,143]. Bertram Hopkinson, son of John Hopkinson, continued this research, and by 1914 the Hopkinson pressure bar technique was born [144]. This technique was devised as a means of measuring the pressure produced at the end of a cylindrical bar, typically imposed by the impact of a bullet or the detonation of gun cotton [145]. Many years later, in 1949, H. Kolsky developed an experiment capable of extracting the stresses and strains present in a thin specimen placed between two long cylindrical bars. This would mark the first appearance of the split Hopkinson bar as known today, also referred to interchangeably as the Kolsky bar [146]. Specimen loading was accomplished by introducing a compressive wave at the end of one bar, referred to as the incident bar, typically by the detonation of a small explosive charge. This compressive wave propagates toward the specimen, where some portion is conducted through the specimen and into the second bar, known as the transmitter bar, while the remainder is reflected away from the specimen and back into the incident bar in the form of a tensile wave.

Kolsky was able to show that the portion of the compressive strain wave passing through the specimen and into the transmitter bar, identified as the transmitted wave,

was proportional to the stress in the specimen. Similarly, Kolsky found that strain in the specimen was proportional to the portion of the compressive strain wave that is reflected, aptly referred to as the reflected wave. Typically, these waves are observed by way of strain gauges placed on the incident and transmitter bars. The bars on either side of the specimen therefore not only act to load the specimen but also become transducers for the stress and strain in the specimen.

6.2 Development of the SHPB

The conventional SHBP consists of a striker and its launching device, an incident bar, and a transmission bar (Figure 92). The bars have the same diameter and type of material and should remain elastic throughout the test so that stress waves could be measured from surface strains [147]. The bars would be aligned and free to move in the strike line axis. In order to have significant radial and shear stresses, the length to diameter ratio of these bars ought to be approximately twenty. Additionally, the striker length should be at most half of the incident bar to avoid wave overlapping at the radial reading location. Besides, to avoid wave overlapping at the strain gauge location, the incident bar is at least twice the length of the striker.

In this study, a SHPB setup was developed to determine the amplitude-dependent wave motion behavior of viscoelastic phononic crystals. For this, an SHPB apparatus was built in the Structure Laboratory at Qatar University.

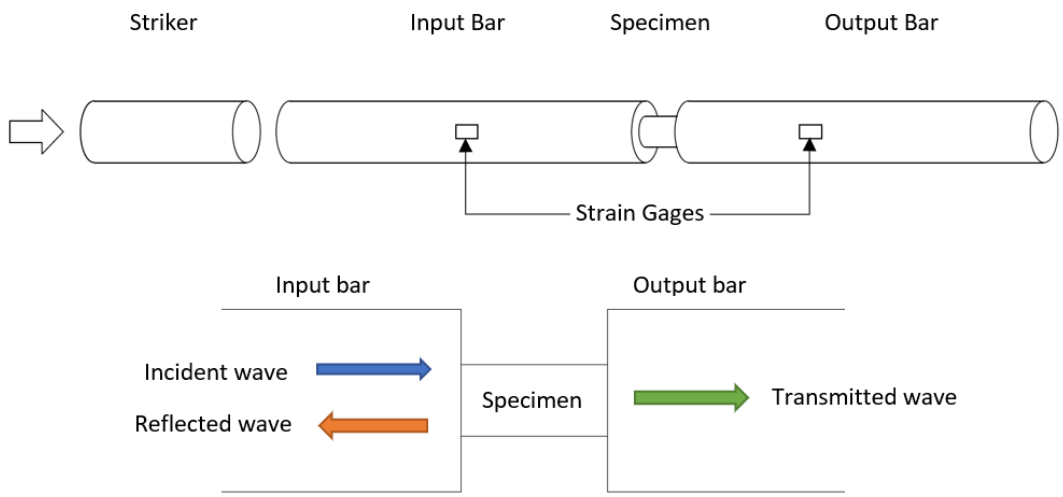

Figure 92. Simple presentation of SHPB set-up

6.2.1 Selection of Bar Material

Because the SHBP system is composed of input and output bars, it was important to choose the right material according to its impedance. For elastic SHPB, 6061-T6 aluminum alloy bars were selected to test high impedance materials. For low impedance materials, a wide range of polymeric bar materials were studied to determine which were appropriate for the polymeric SHPB setup. Table 19 compares the impedance of different polymeric bars having the same cross-sectional area.

Table 19. Comparison of polymeric materials

Polymeric Material	Modulus (N/m^2)	Density (kg/m^3)	Wave Velocity (m/s)	Impedance (Density*Velocity) ($kg/(m^2.s)$)
PTFE	4.6E8	2200	457.26	1.01E6
LDPE	3.7E8	920	634.17	5.83E5
UHMWPE	5.5E8	950	760.89	7.23E5
HDPE	7E8	950	858.40	8.15E5
NYLON 66	1.5E9	1140	1147.08	1.31E6
ABS	1.4E9	1040	1160.24	1.21E6
PC	2.4E9	1200	1414.21	1.7E6
ABS	2.5E9	1020	1565.56	1.6E6
PVC	3.4E9	1330	1598.87	2.13E6

Three materials Nylon-66, UHMWPE, and PTFE were selected, based on the gap in impedance value between them. According to the literature [148], the stress-strain curves of these polymeric materials have been plotted in

Figure 93 and

Figure 94 along with their initial elastic modulus. The stress-strain curves of these polymers are presented at low and high strain percentages in

Figure 93 and

Figure 94 respectively.

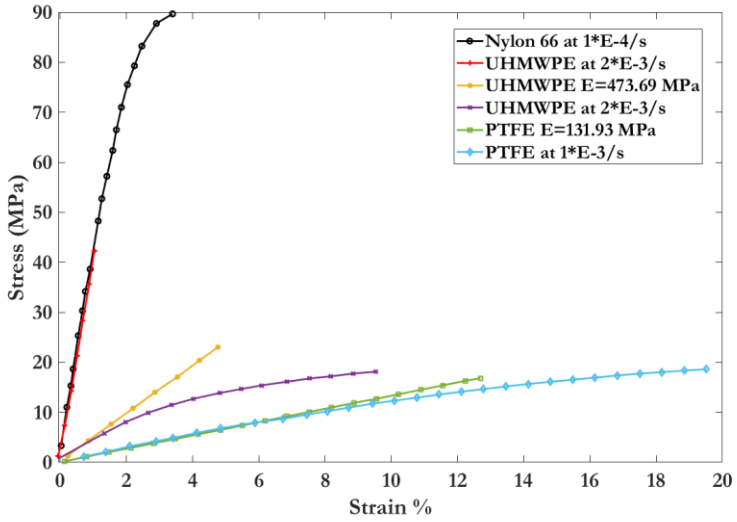

Figure 93. Comparison of Stress-Strain Curves of Polymers at a Low Strain Rate [148]

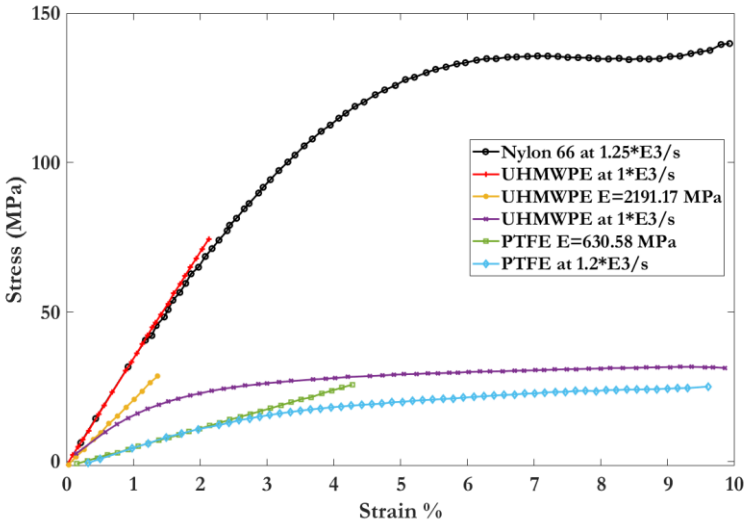

Figure 94. Comparison of Stress-Strain Curves of Polymers at High Strain Rates [148]

When the strain rate varies, the elastic modulus varies as well. According to Figure 93 and Figure 94, the variation is less severe for Nylon-66. Nylon-66 was thus selected for polymeric SHPB.

6.2.2 General Configuration of SHPB System

The experimental set-up for the SHPB was designed with 3.0 m long input and output bars.

Figure 95 shows the setup in the Structure Laboratory at Qatar University. Shaft supports were used for holding the input and output bars. The locations of the shafts were determined from the buckling analysis for the striker generated force. The maximum longitudinal expected forces in the bars were based on the material properties of Nylon-66. The bar system was supported by an I-beam carried by four I-columns. Other components of the SHPB set-up were the specimen casing and rubber wall (Figure 96). The specimen casing was set for containing the crushed specimen fragments during the experiment (Figure 96a) and a rubber wall was placed for restraining the output bar from going out of the system (Figure 96b).

The striker bar (Figure 97) impacted the input bar after being launched by a gas gun. An automated gas launcher SURE-Launch™ from REL Inc was used (Figure 98). This launcher could precisely accelerate a range of striker sizes for tension and compression testing. The diameter of the striker launcher barrel was 2 inches.

Figure 95. SHPB in structure laboratory

(a) (b)

Figure 96. Safety components (a) Specimen casing (b) Momentum trap

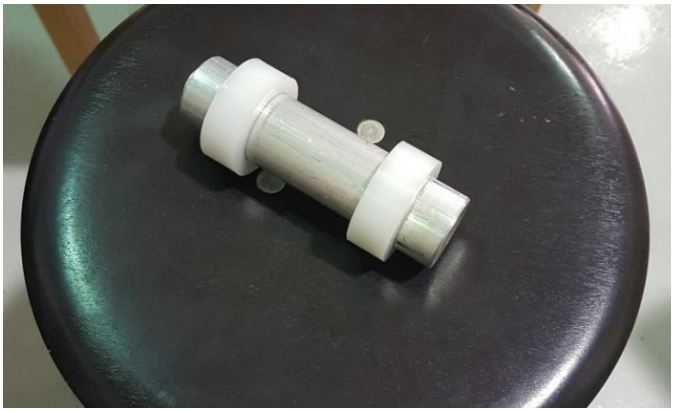

Figure 97. 150 mm Aluminum striker with UHMW Polyethylene rings

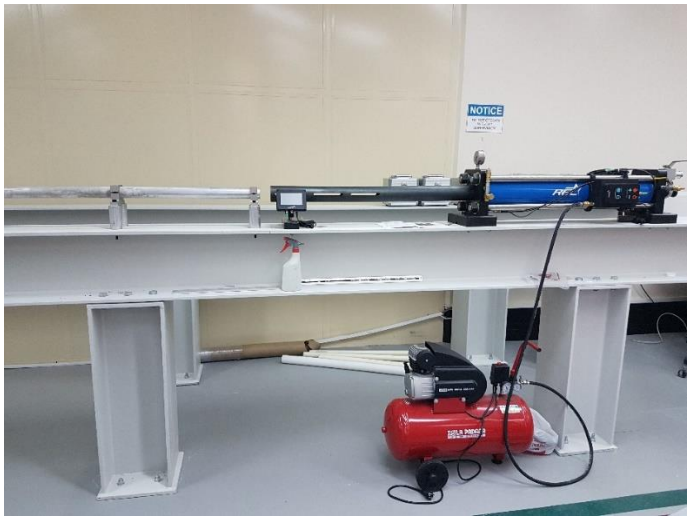

Figure 98. Striker launcher

6.2.2.1 Bar Diameter

The diameter of the Hopkinson bars is the main parameter to design a SHPB apparatus. It relates to the bar's length and the specimen size. The assumption in SHPB for the 1D wave theory is that the length to diameter ratio of each bar should be greater than 20 [149]. The phononic crystals used in this study had a diameter of 40 mm as illustrated in chapter 4. Thus, the Aluminum alloy and Nylon-66 bars dimensions were selected to be 3 meters in length and 50 mm in diameter, which gave a length to diameter ratio of 60.

6.2.2.2 Striker Length

The striker bar hits the input bar, and a wave propagates through the input then the output bar. At the free end of the output bar, the wave reflects back towards the input bar. The time difference between the reading of the incident and reflected signal by the input bar strain gauges is written as follows:

$$\Delta t = 2\,L_s/v_s$$

Where L_s is the striker length and v_s is the striker velocity. To distinguish the incident and reflected signal readings, it is recommended for the striker length to be less than

half the length of the input bar. The ideal incident signal in SHPB is a sharp impulse. Moreover, the incident signal needs to be sufficient to excite the amplitude dependent dynamic behavior of the mechanical metamaterial specimen. A short impulse time can be achieved by adopting a shorter striker. Nonetheless, a shorter striker would have small inertia therefore a higher launching speed. The striker launching speed is typically limited by the specification of a given SHPB striker-launching system. Diversely, a longer striker would generate a high impulse with low launching speeds, but it suffers frequency amplitude drops in the incident wave spectrum [150–152].

6.2.2.3 Accompanying Accessories

- Bar Support

The input and output bars were each held up by six shaft supports. The shaft support had a detachable top for easy replacement of bars and an internal diameter of 50 mm.

Figure 99. Detailed Shaft Support

- Velocity sensor

Along with SURE-Launch™, a speed sensor SURE-Speed™ was used for velocity measurement of striker bars during testing.

Figure 100. Velocity sensor from REL Inc.

- Strain gauge and Data Acquisition

Strain gauges are the standard technique to measure bar strains in SHPB setups. Two strain gauges are usually mounted at symmetrically opposing sides on the surface of each of the input and output bars. The signal from the strain gauges is conditioned with a Wheatstone bridge. Having the voltage output in the order of millivolts, a signal amplifier is necessary to record the signal paired with a high-frequency oscilloscope. The signal recorded in SHPB duration is usually shorter than one millisecond. In this setup, the frequency response of the data acquisition is 1 MHz.

To read the strain on the polymer bars, where the strain was relatively higher, strain gauges with a high strain capacity were selected. An Omega strain gauge KFH series was selected with 120 Ω resistance and 0.8 mm gauge length.

Figure 101 shows the block diagram of the data acquisition set-up of the strain measurements. The top and bottom strain gauges were utilized in the half-bridge electronic configuration for noise and offset signal cancellation caused by the long wires used from the bars connecting the signal conditioning circuit. The differential voltages produced by the two bridges (U_{01} and U_{02}) are relatively small and difficult to be detected and may still include electrical noise, hence, a signal conditioning circuit was required to amplify and filter U_{01} and U_{02} signals resulting in V_{01} and V_{02},

respectively. V_{01} and V_{02} were then converted to a digital signal using the NI ELVIS II^+ Board for a subsequent USB interface in the computer workstation. A LabVIEW graphical program (Appendix C) was created to visualize and record the vibration signals acquired from the input and output bars.

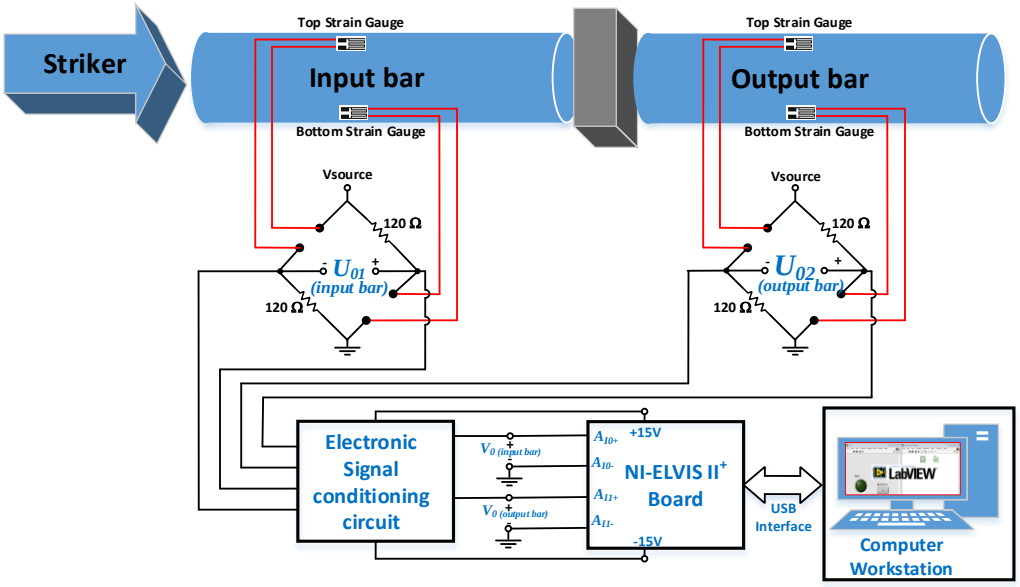

(A)

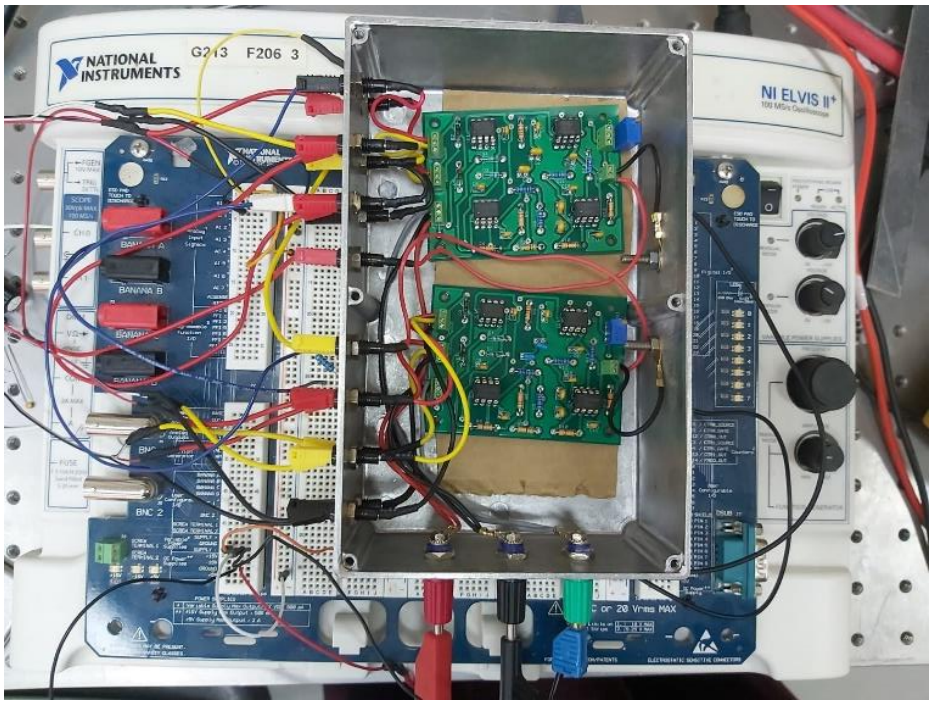

(B)

Figure 101. Data acquisition set-up

6.3 Calibration of the SHPB setup

In this study, the SHPB setup was used to obtain the transmission coefficient of the mechanical metamaterials composed of both elastic and viscoelastic material. The metallic SHPB bar material had significantly high impedance compared to the specimen viscoelastic material. This impedance mismatch between the elastic and viscoelastic materials caused a problem with the signal-to-noise ratio [147,153]. Therefore, both polymeric and metallic SHPB setups were considered.

6.3.1 Bar Alignment Operation

For the SHPB setup, the input bar, the striker, and the output bar ought to be perfectly aligned. For this purpose, the SHPB system was installed on top of a table made of a single I-beam. The gas gun was placed on this same beam to ensure the alignment of its barrel. Low tolerance aluminum shaft supports were used for the input and output bars. Moreover, a high-precision laser beam was used to align all components. Furthermore, the striker impacting end was tapered for a coaxial impact with the input bar (See Figure 103).

Figure 102. Leveling of the Steel I-beam

Figure 103. Tapered Nylon and aluminum striker

Each type of bar purchased had a straightness tolerance determined during manufacturing conditions. The straightness of the bars was necessary for 1D longitudinal wave propagation theory applicability. To reduce the risk of flexural creep in the bars, especially the viscoelastic ones, twelve shaft supports were placed to support the input and output bars. Besides this, the strain in the bars was measured by two strain gauges, one on top and one on the bottom of the bar, to nullify the flexural effect due to reading the strain from the surface of the bar. The resultant reading from diametrically opposite strain gauges in a half-bridge configuration was a clean longitudinal wave. Figure 104 represents the top (o) and bottom (x) strain gauge signal that shows both longitudinal and flexural wave signal. The black line is the resultant longitudinal signal obtained with the half-bridge configuration without flexural waves. One last aspect of the bars' good alignment was the parallelization of the bars' end faces. For this, the input and output bars were placed in direct contact with each other to ensure that the read strain was the same throughout the two bars.

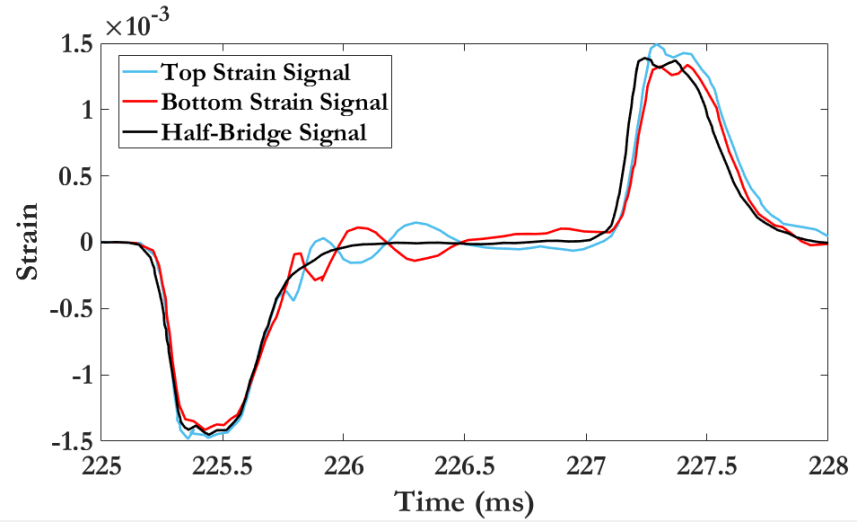

Figure 104. Strain signal from top and bottom strain gauges of the same bar section and the resultant longitudinal wave signal

6.3.2 Propagation Coefficient Calibration

6.3.2.1 Single Bar Impact Test

To calibrate the aluminum and nylon bars, the frequency-dependent propagation coefficient needed to be determined. Metallic bars in SHPB are affected by wave dispersion [153], and the viscoelastic bars have inherent damping. Therefore, calibration of both systems of bars is necessary to determine the signal on both interfaces of the specimen based on readings on the mid-bar surface. The frequency-dependent propagation coefficient of each type of bar: Aluminum and Nylon is determined in this section. The time-domain signal recorded by the strain gauges is converted by Fourier transformation to a frequency domain signal. The rightward traveling wave is defined as $\hat{\varepsilon}_R(x_0,\omega)$ and the leftward traveling wave $\hat{\varepsilon}_L(x_0,\omega)$ where x_0 is a random reference point in the bar. The wave is then:

$$\hat{\varepsilon}(x,\omega) = \hat{\varepsilon}_R(x_0,\omega)e^{-i\kappa_{bar}(\omega)(x-x_0)} + \hat{\varepsilon}_L(x_0,\omega)e^{-i\kappa_{bar}(\omega)(x-x_0)} \quad (17)$$

The propagation coefficient of the SHPB bar $\kappa_{bar}(\omega)$ is a function of the bar's material complex modulus $\hat{E}(\omega)$.

$$\kappa_{bar}^2(\omega) = \frac{\rho\omega^2}{\hat{E}(\omega)} \quad (18)$$

The propagation coefficient is composed of a real κ_{bar}^R and imaginary part κ_{bar}^I representing the wavenumber and the attenuation coefficient, respectively.

$$\kappa_{bar}(\omega) = \kappa_{bar}^R(\omega) + \kappa_{bar}^I(\omega) \quad (19)$$

The identification of the propagation coefficient effort is called the single-bar impact test. Whenever only one bar is hit on one end by a striker the wave travels along the bar (incident wave $\hat{\varepsilon}_{inc}$) and the reflects at its free end (reflected wave $\hat{\varepsilon}_{ref}$). The transfer function [147] is then:

$$H(\omega) = -\frac{\hat{\varepsilon}_{ref}}{\hat{\varepsilon}_{inc}} = e^{-2i\kappa_{bar}(\omega)d} \quad (20)$$

d is the distance between the free end and the strain gauges. The wavenumber and the attenuation coefficient are then:

$$\kappa_{bar}^R(\omega) = -\frac{arg|H(\omega)|}{2d} \quad , \quad \kappa_{bar}^I(\omega) = -\frac{ln|H(\omega)|}{2d} \quad (21)$$

The propagation coefficient can then be used to determine the end of the bar reading based on the strain gauge readings, and consequently, the interfaces of the specimen with the bars in the SHPB test are determined.

The propagation coefficient $\kappa_{bar}(\omega)$ depends on the pulse energy and shape. The pulse energy and shape can be widened by varying the striker sizes and velocities. Comparing the longitudinal phase velocity c_l to the Pochhammer-Chree longitudinal wave equation [154] permits the determination of the valid frequency range of the experimentally recorded $\kappa_{bar}(\omega)$.

$$\frac{2\alpha}{r_b}(\beta^2 + \kappa^2)J_1(\alpha r_b)J_1(\beta r_b) - (\beta^2 - \kappa^2)^2 J_0(\alpha r_b)J_1(\beta r_b) -$$

$$4\kappa^2\alpha\beta J_1(\alpha r_b)J_0(\beta r_b) = 0 \quad (22)$$

The Pochhammer-Chree longitudinal wave equation of a circular bar of r_b radius is calculated according to Equation 22 where α is the pressure wave and β is the shear

wave and J_0 and J_1 are Bessel functions of the first kind. Figure 105 represents the results of the calibration for the nylon bar. A single bar test was conducted for the nylon bar where a 150 mm striker at 5.09 m/s hit the bar on one end, and the other end was free. The first wave in Figure 105(A) is the incident wave, and the second wave is the reflected wave recorded by strain gauges located in the middle of the bar. The signal obtained in Figure 105(A) is converted to a dispersion relation in Figure 105(B) and compared to the corresponding analytical Pochhammer-Chree longitudinal wave equation. Note that the experimental validity of the phase velocity of the nylon bar is up to 12 kHz according to the comparison in Figure 105(B). Moreover, the frequency-dependent attenuation coefficient presented in Figure 105(C) shows a quasi-linear relation in the same validity frequency range.

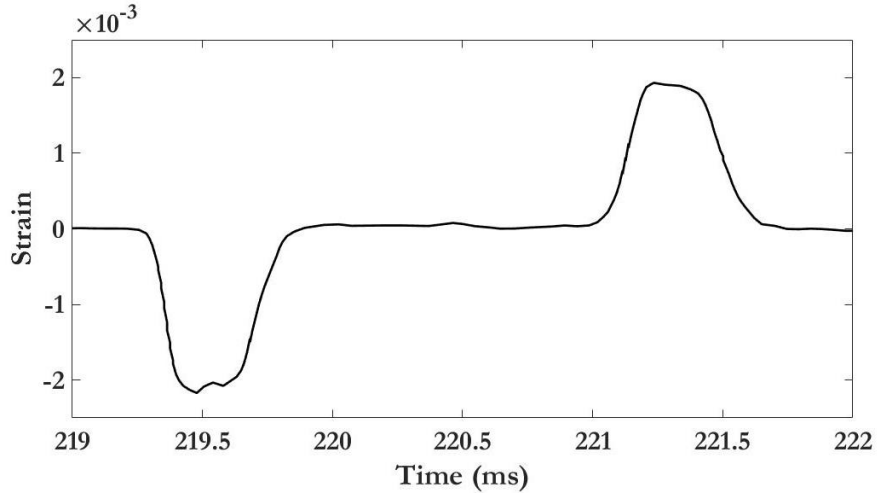

(A)

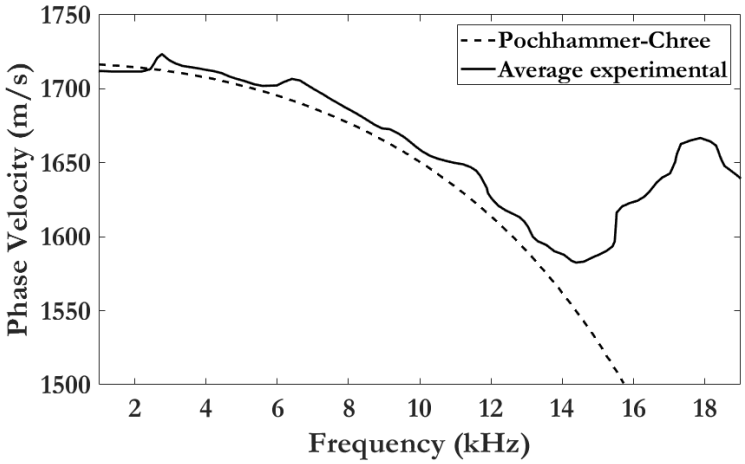

(B)

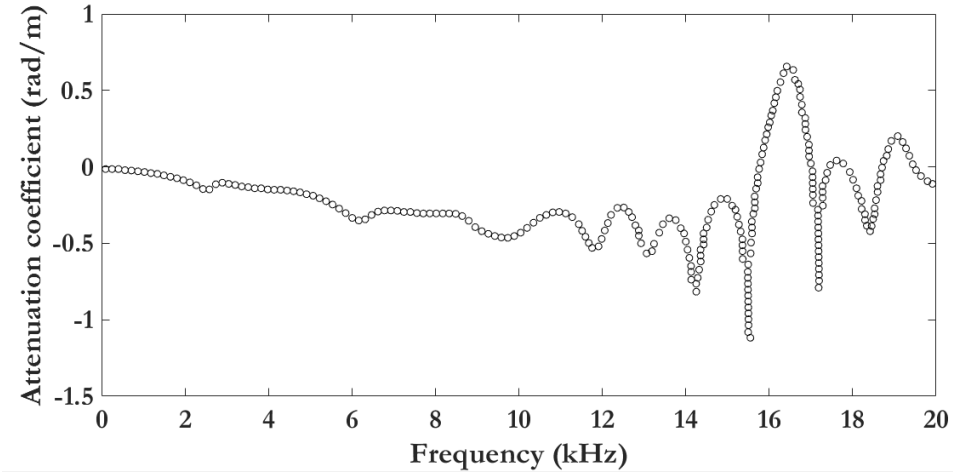

(C)

Figure 105. Single bar test results (A) Incident and reflected wave of a single Nylon bar hit by a 250 mm striker (B) Phase velocity ($c_l = \omega/\kappa$) in function of frequency compared to Pochhammer-Chree analytical results (C) Frequency-dependent attenuation coefficient.

6.3.2.2 Refined Propagation Coefficient

The propagation coefficient, and consequently the phase velocity and the attenuation coefficient, depends on the pulse energy and duration. Thus, single bar tests ought to be run with different lengths and velocities of strikers. The results ought then to be presented in the form of a propagation coefficient spectrum. So, for each SHPB bar

type, the strain at the specimen/bar interface can be inferred by the reading of the strain gauges on the mid bar location. Multiple strikers should be used for multiple single bar tests for each bar material, and the results averaged of the phase velocity and the attenuation coefficient. Thirty single bar tests were therefore run with striker lengths ranging from 50 to 300 mm with speeds up to 20 m/s. Figure 106(A-1) and (B-1) show the propagation coefficient spectrum for both aluminum and nylon bars, respectively. The dashed line represents the average experimental values, and the solid line represents the analytical solution (Equation 22) assuming the material is linear. By comparing the analytical and experimental plots, there is a fair agreement up to 40 kHz for Aluminum alloy bars and up to 10 kHz for nylon bars. At low frequency, the phase velocity of the nylon bar deviates from the Pochhammer-Chree solution due to the viscoelastic effect of the material. In Figure 106(A-2) and Figure 106(B-2), the attenuation coefficient presents a quasi-linear relation with the frequency up to 40 kHz and 11 kHz, respectively. The validity of a SHPB setup consisting of aluminum and nylon bars for determining the transmission properties of MMs specimens is then demonstrated up to 11 kHz.

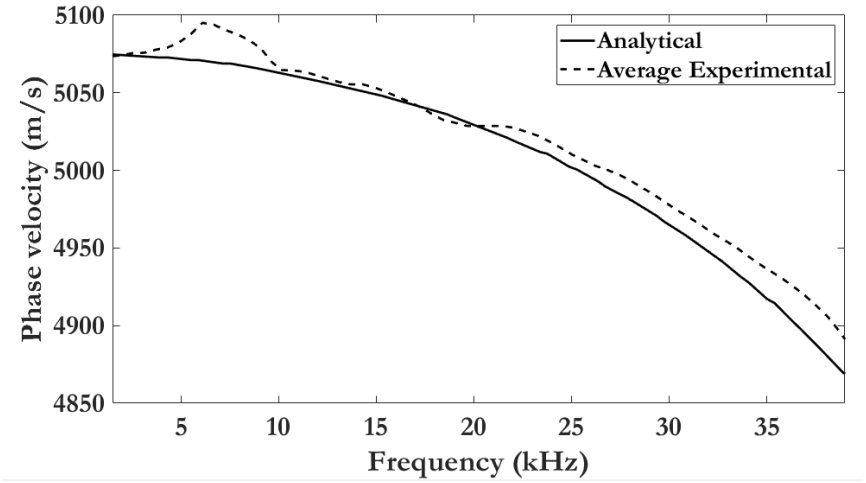

(A-1)

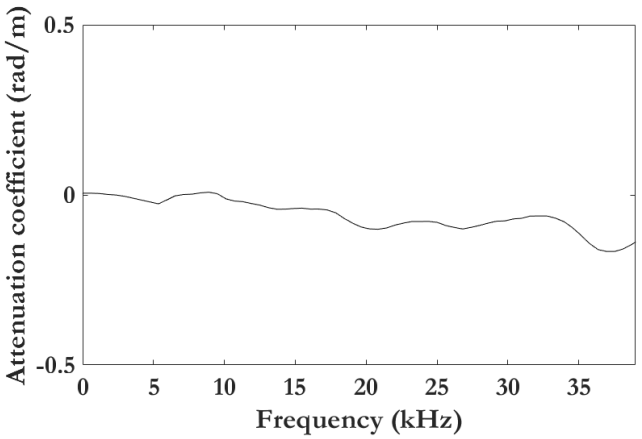

(A-2)

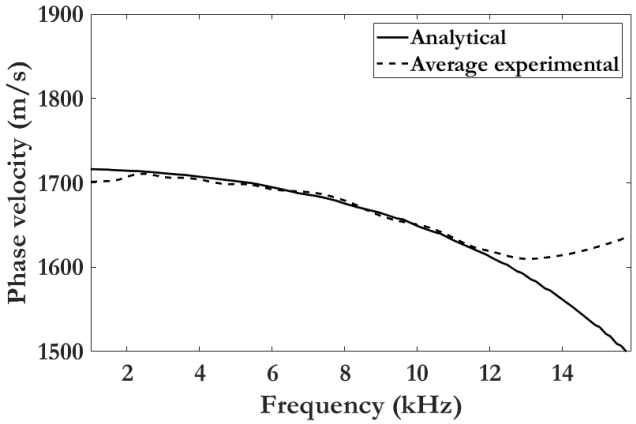

(B-1)

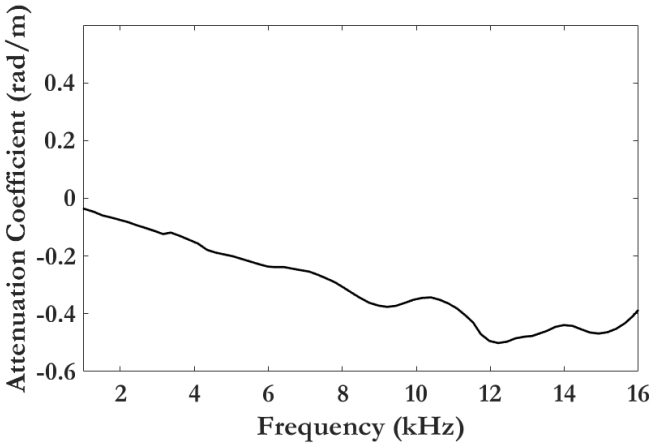

(B-2)

Figure 106. (A-1) Phase velocity of the aluminum bar, (A-2) Attenuation coefficient of the aluminum bar, (B-1) Phase velocity of the nylon bar, (B-2) Attenuation coefficient of the nylon bar

6.3.3 SHPB Bar Alignment Calibration

To check the SHPB bar system alignment, the striker is launched on the incident bar, which is in direct contact with the transmission bar without any specimens in between. The incident pulse should have a trapezoidal shape with a clean baseline. If the striker and the bars are not appropriately aligned, a reflected wave would appear in the incident signal reading. To have both qualitative and quantitative calibrations for the bar alignment, the strain signal for both bars should overlap each other. The strain signal measured at x_{inp} and x_{out}, is called $\varepsilon_{R,inp}(x_{inp},t)$ and $\varepsilon_{R,out}(x_{out},t)$, respectively. At the contact location x_c, the input strain signal $\hat{\varepsilon}_{inp}(x_c,\omega)$ and $\hat{\varepsilon}_{out}(x_c,\omega)$ can be calculated using the following formulas:

$$\hat{\varepsilon}_{inp}(x_c,\omega) = \hat{\varepsilon}_{R,inp}(x_{inp},\omega)e^{-i\kappa_{bar}(\omega)(x_c-x_{inp})}$$

$$\hat{\varepsilon}_{out}(x_c,\omega) = \hat{\varepsilon}_{R,out}(x_{out},\omega)e^{i\kappa_{bar}(\omega)(x_{out}-x_c)} \quad (23)$$

$\hat{\varepsilon}_{inp}(x_c,\omega)$ and $\hat{\varepsilon}_{out}(x_c,\omega)$ would then be converted using an inverse Fourier transform to $\varepsilon_{inp}(x_c,t)$ and $\varepsilon_{out}(x_c,t)$, respectively. Figure 107 shows the input and output signals for bar alignment calibration using different striker lengths. The solid line represents the input signal, and the pointed line the output signal. Comparing the output and the input signal confirms the accuracy of the $\kappa_{bar}(\omega)$, and the similitude between the signal confirms the good alignment of the bars.

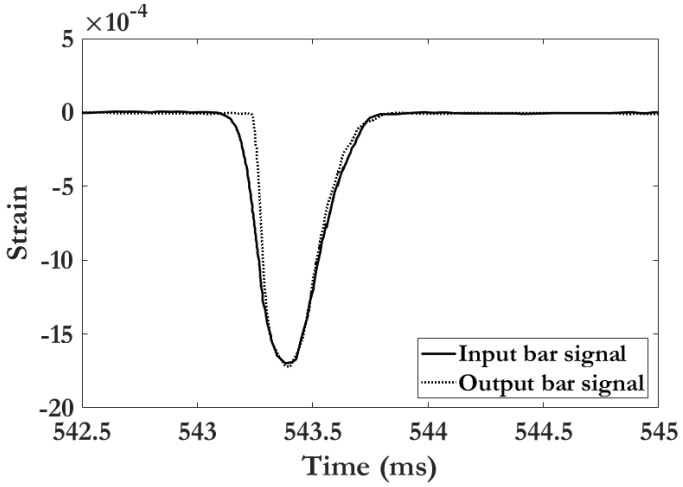
×10^-4
5
0
-5
-10
-15
-20
Strain
542.5
543
543.5
544
544.5
545
Time (ms)
Input bar signal
Output bar signal

(A)

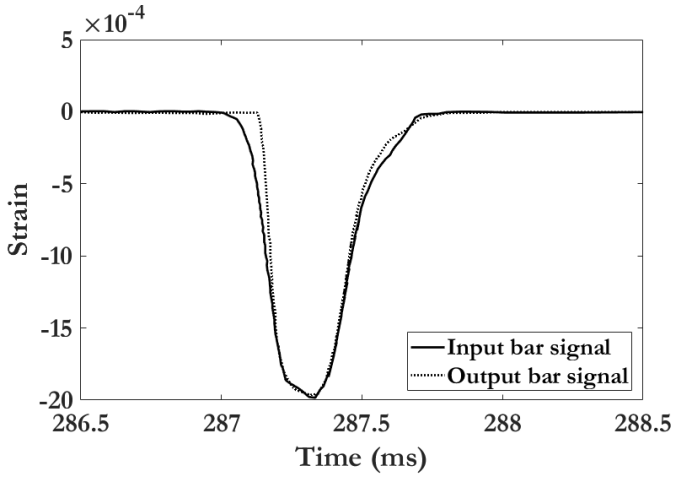
×10^-4
5
0
-5
-10
-15
-20
Strain
286.5
287
287.5
288
288.5
Time (ms)
Input bar signal
Output bar signal

(B)

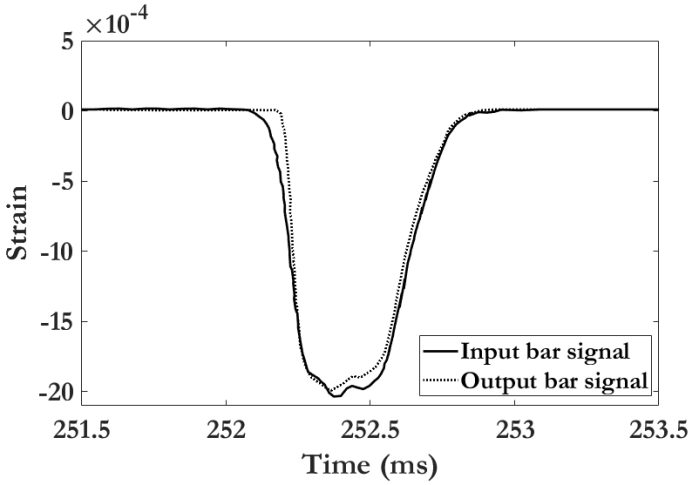
×10^-4
5
0
-5
-10
-15
-20
Strain
251.5
252
252.5
253
253.5
Time (ms)
Input bar signal
Output bar signal

(C)

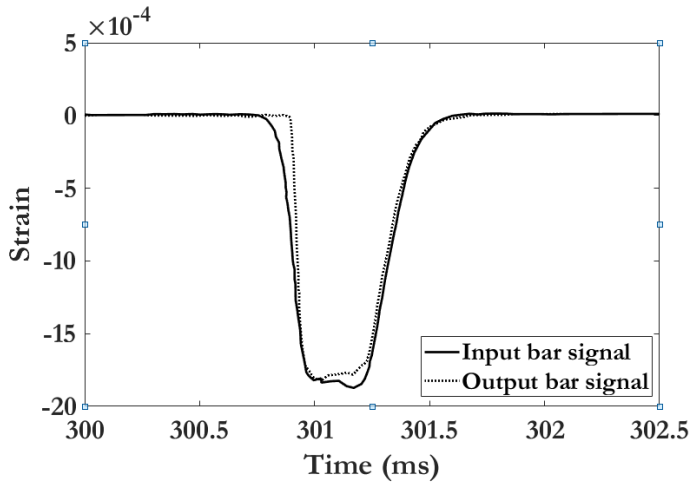

(D)

Figure 107. Bar alignment test results (A) 150 mm striker (B) 200 mm striker (C) 250 mm striker (D) 300 mm striker

6.4 Electrodynamic shaker tests

The phononic crystals experimental study using harmonic small amplitude forces employs electrodynamic shakers [62,155] and piezoelectric actuators [74,156]. However, to study the nonlinear behavior of phononic crystals, higher amplitude dynamic testing conditions and the dispersion properties of the viscoelastic constituents should be considered. In this study, the nonlinear wave transmission behavior of one-dimensional viscoelastic phononic crystals was investigated. However, before investigating the amplitude-dependent vibration attenuation behavior, a reference study using an electrodynamic shaker was conducted with small forces and a high-frequency range. Later an impulse-dependent vibration attenuation of the same specimen was conducted using the SHPB apparatus.

The specimen selected to compare the electrodynamic shaker results and the SHPB impact test results was a bilayered phononic crystal composed of four layers of aluminum 6061-T6 and three layers of silicone rubber (Elite double 32, Zhermack). The properties of each material are detailed in chapter 4, section 4.2.1.

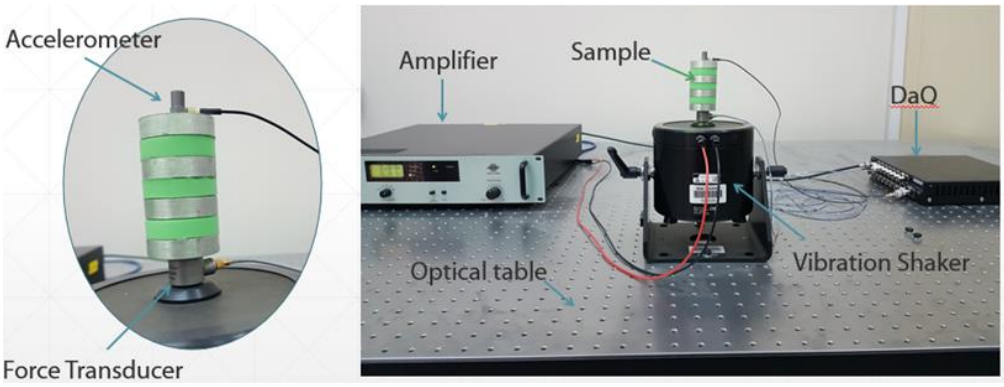

(a) (b)

Figure 108. Specimen and detailed electrodynamic shaker setup

The specimen was subjected to a chirp signal base excitation. The output acceleration signal and the input force signal were recorded. The frequency response function was the Fourier transform ratio of the output acceleration over the input force of the signal (see Figure 109(A). The base excitation force was 21 N. Similarly to section 4.3, a finite element simulation was conducted using Abaqus steady-state harmonic analysis [124] in the 1 to 16000 Hz range. The specimen was modelled asymmetrically (See Figure 110). The vertical loading was applied at the central input node of the lower layer, as illustrated in Figure 110. The vertical acceleration response was computed at the upper central node of the upper layer, as also illustrated in Figure 110. The specimen here was composed of aluminum alloy 6061-T6 and Elite double 32; all material properties and finite element model details (mesh element, mesh size) are shown in chapter 4, section 4.3. The response of the model was computed in the frequency domain under harmonic vertical excitation. The numerical results are shown in Figure 109(B). Three low transmission zones appear in the numerical frequency response in Figure 109 (B). The low transmission zones are highlighted in yellow: (A) Experimental: 2kHz, 3 kHz, 10 kHz, and 14 kHz, and (B) Numerical: 2kHz, 3 kHz, 10 kHz, and 14 kHz. The experimental low-frequency zones in Figure 109(A) are in good agreement with the finite element equivalent.

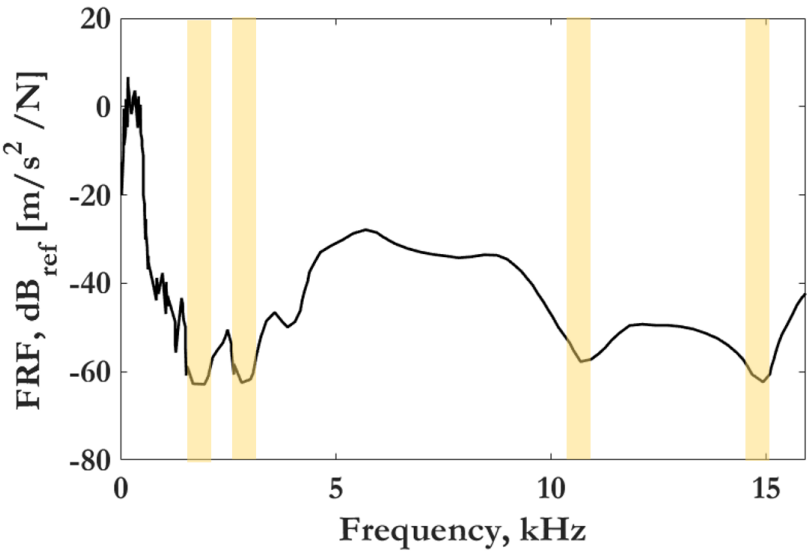

(A)

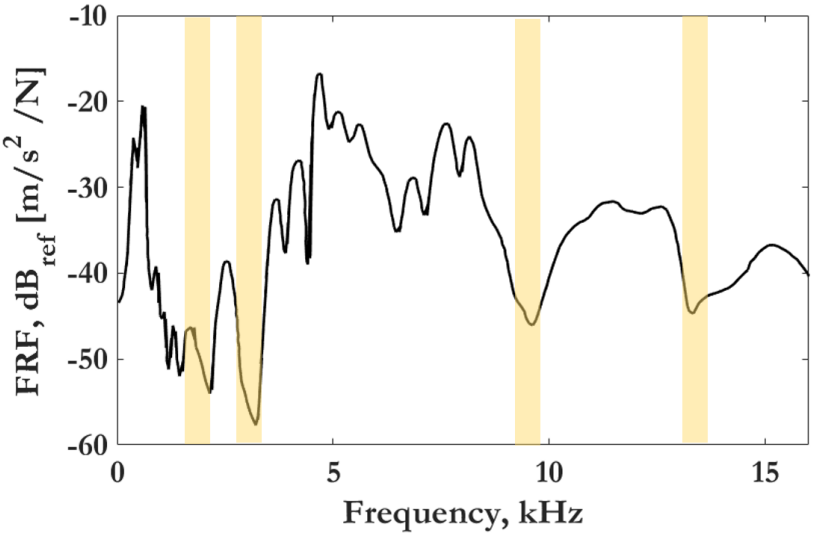

(B)

Figure 109. Frequency response function. (A) Experimental FRF (B) Numerical FRF

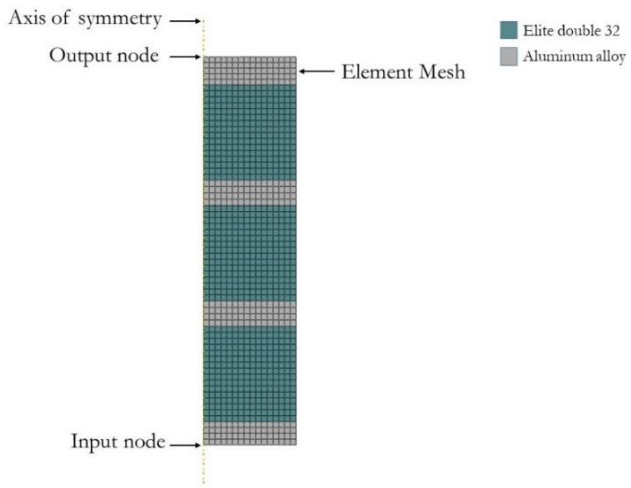

Figure 110. MM axisymmetric specimen FE model

6.5 Impact Excitation Analysis and Results

Recent studies by Feng and Liu [81,82] proposed the SHPB apparatus as a mean to study wave propagation in phononic crystals. The SHPB was preferred for its high strain rate tests [153]. Feng and Liu used a steel SHPB setup to test steel/epoxy phononic crystals ($E_{epoxy} \approx 4GPa \ll E_{steel} \approx 210\ GPa$). The difference between the two materials' moduli of elasticity produced an impedance mismatch in the mechanical conductivity between the two mediums. The viscoelastic properties of the constituents of the phononic crystals therefore require proper attention to correctly determine their propagation properties. Some researchers have attempted to use hollow bars [157,158] or polymeric bars [159,160] to override this problem. Nevertheless, the modified SHPB bar system should still provide high impact energy that ensures a good signal-to-noise ratio, which is not the case if the input bar significantly dissipates the incident wave. Additionally, the length of the striker does affect the spectrum of the incident wave, where a long striker causes amplitude-drops in the incident wave at some frequencies [150,161]. This study adapted the SHPB apparatus for viscoelastic phononic crystal analysis with proposed solutions to the above-mentioned limitation.

6.5.1 Hybrid SHPB Configuration

In the typical SHPB, a striker is launched at a certain speed and hits the input bar producing a stress wave. The wave passes through the input bar, the specimen, and the output bar. A metallic SHPB setup would ensure a high signal-to-noise ratio of the incident wave. However, the transmitted wave would be very weak due to the viscoelastic damping of the phononic crystal constituents. The transmitted wave would have a low signal-to-noise ratio. If a modified SHPB is adopted namely a polymeric SHPB, the transmitted wave would have a high signal-to-noise ratio. However, a high impulse could deform the polymeric input bar. Such an impulse in the elastic domain of the bar would also be attenuated by passing through the viscoelastic material of the input bar [147,162]. Thus, the requirement for a fitting SHPB setup is a configuration which both allows the transmission of a *large input force* and the recording of *weak transmitted wave*. For this purpose, a *hybrid SHPB* was developed, where the input bar was made of aluminum and the output bar of nylon. The equipment used for this setup is detailed in section 6.2.2. The details about the hybrid bar system are listed in Table 20.

Table 20. Hybrid SHPB bar system

Components	Material type	Length, m	Diameter, mm	Longitudinal wave speed, m/s	Mass density, kg/m^3	Distance between the specimen/bar interface and the strain gauge, m
Striker	Aluminum alloy 6061-T6	0.05, 0.15, 0.25, 0.3	45	5070	2700	-
Input bar	Aluminum alloy 6061-T6	3	45	5070	2700	1.5
Output bar	Nylon PA-66	3	50	1700	1140	0.3

The apparatus aluminum and nylon bars are calibrated as shown in section 6.3.2.2 and the phase velocity $c_{bar}(\omega) = \omega/\kappa_{bar}^{R}(\omega)$ and the attenuation coefficient $\kappa_{bar}^{I}(\omega)$ for both bars are shown in Figure 106.

To study the wave attenuation behavior of phononic crystals, the incident signal should be high to excite the amplitude-dependent behavior of the specimen and its impulse sharp in time domain. The nearer the input signal is to the Dirac delta function, the better. In SHPB, a sharp impulse can be obtained using a short striker, but due to the low inertia of short strikers, a high launching speed is required. The launching speed is limited by the specifications of the launching system. Conversely, a long striker can generate high impulses due to its inertia. However, the input wave suffers amplitude drops [150–152]. An amplitude drop means that the incident wave lacks some frequencies in its range. When an amplitude drop occurs, the transmission coefficient of the specimen is compromised.

To study this effect, additional single bar tests were conducted with different lengths of strikers (50, 150, 250 mm). The input bar signal was recorded and using the Fast Fourier transform (FFT) of the incident signal, the input strain is plotted in Figure 111. Amplitude drops can be noted in Figure 111 which occur at different frequencies according to the striker length. By analyzing the results plotted in Figure 111, the frequency ranges valid for each striker can be determined. The frequency ranges up to 8 kHz, 14 kHz and 20 kHz are the validity ranges of the 250, 150, 50 mm strikers, respectively.

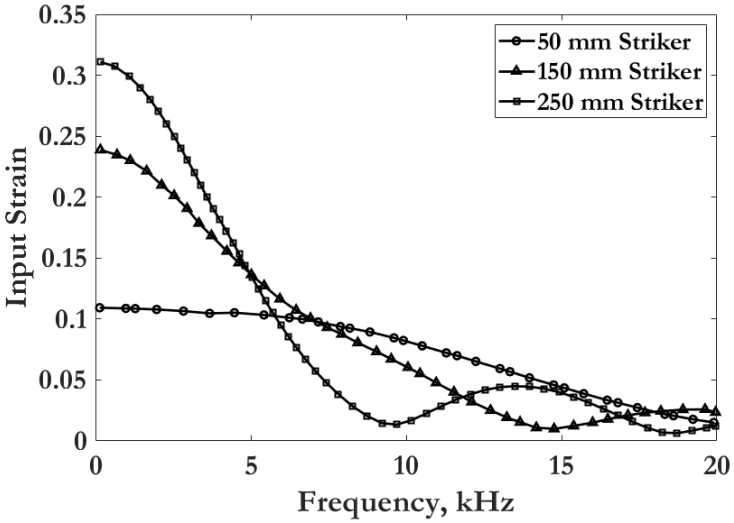

Figure 111. Input strain signal at different striker lengths

The hybrid SHPB tests were conducted on the phononic crystal specimen composed of four layers of aluminum 6061-T6 and three layers of silicone rubber (Elite double 32, Zhermack) (Figure 112). Three different striker conditions were operated: (A-1) 50 mm striker (A-2) 150 mm striker (A-3) 250 mm striker (See Figure 113). The input force spectrum $F(\omega)$ and the output acceleration spectrum $A(\omega)$ are a function of the FFT of the incident and the transmitted strain signals.

$$F(\omega) = \frac{s_{al}\rho_{al}\omega^2}{\kappa_{al}(\omega)^2}\hat{\varepsilon}_{inc}(\omega)e^{i\kappa_{al}(\omega)\Delta_{al}}$$

$$A(\omega) = \frac{-i\omega^2}{\kappa_{ny}(\omega)}\hat{\varepsilon}_{tra}(\omega)e^{i\kappa_{ny}(\omega)\Delta_{ny}} \quad (24)$$

Where $\hat{\varepsilon}_{inc}(\omega)$ and $\hat{\varepsilon}_{tra}(\omega)$ are the FFT of the incident and transmitted signals; ρ is the density and s is the cross-section area; al is for aluminum alloy 6061-T6 and ny is for Nylon-66. Delta (Δ) is the distance between the strain gauge location and the specimen bar interface. The wave transmission coefficient $C_t(\omega)$ is then calculated:

$$C_t(\omega) = \frac{\|A_{out}(\omega)\|}{\|F_{in}(\omega)\|}, \quad (25)$$

where $\|\quad\|$ is the Euclidean norm.

The wave transmission coefficient for the experimental SHPB is plotted in Figure

113A. Note that the highlighted areas in yellow indicate the low transmission zones. The solid line represents the transmission coefficient and the dotted part the distorted experimental transmission coefficient due to the amplitude drop discussed above. The impulse applied to the specimen can be calculated by reconstructing the time history of the incident wave then dividing it by the loading duration. The time signal is the inverse of the FFT of $F(\omega)$. The 50, 150, 250 mm strikers' impulses are then 5.6, 13.2, 18.6 N.s respectively. By examining the solid line in Figure 113(A-1), three low transmission zones appear around 1.5, 3, and 7.5 kHz. These low transmission zones are close to the one found for the electrodynamic shaker test in section 6.4. However, the 14 kHz low-frequency zone cannot be identified in Figure 113(A-1), due to the low signal-to-noise ratio in this frequency range. As the impulse gets higher in Figure 113(A-2) and Figure 113(A-3), a new low transmission zone appears around 5.5 kHz and becomes more pronounced at higher impulses. The latter low transmission zone was not observed from the electrodynamic shaker test in section 6.4.

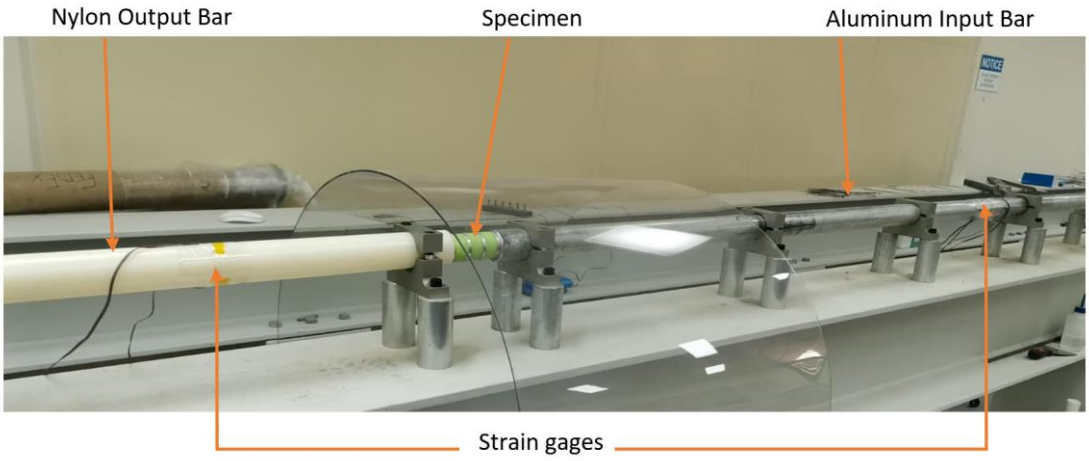

Figure 112. Hybrid SHPB

6.5.2 Time-domain FE Simulations

An explicit Abaqus model has been simulated representing the SHPB components (Striker, input bar, specimen, output bar). The simulation is run in the time domain

using a two-dimensional axisymmetric model, see Figure 114. The axisymmetric element CAX8RH (a 4-node bilinear, reduced integration with hourglass control) was chosen with a 1.25 mm mesh for the specimen and 2.5 mm for the bars. The aluminum bar was modeled as an elastic material with properties listed in Table 11. The nylon bar was modeled as a linear viscoelastic material with scaled Prony series parameters from Fujikawa and Takashi Generalized Model [163]. The contact face between the specimen and the bars was modeled with a Coulomb friction of 1.2 for the aluminum/aluminum interface and 0.1 for the nylon/aluminum interface [164,165].

The numerical transmission coefficient $C_t(\omega)$ is shown in Figure 113B. Figure 113B simulations correspond to Figure 113A testing conditions. The solid line represents the transmission coefficient and the dotted part the distorted experimental transmission coefficient due to the amplitude drop. In Figure 113(B-1), three low transmission zones can be identified around 2, 8 and 15 kHz. The low transmission zone around 15 kHz corresponds to the electrodynamic shaker test at 14 kHz, with the difference due to a low signal to noise ratio. Interestingly, the 5.5 kHz new transmission zone is predicted numerically in Figure 113(B-2,3) similar to the experiments 5.22(A-2,3). Moreover, another new transmission zone appears around 12 kHz in Figure 113(B-1,2) that does not appear in experiments due to the low signal to noise ratio in high frequencies.

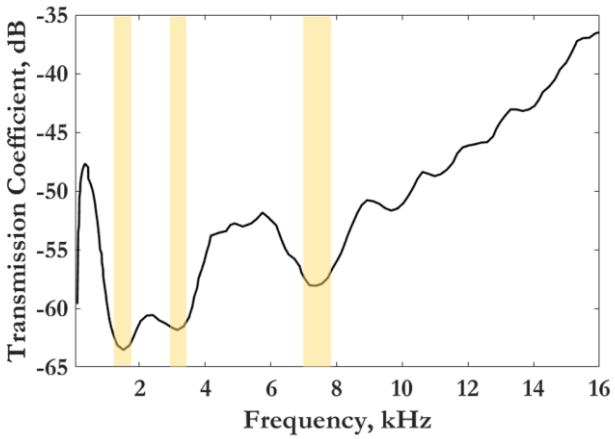

(A-1)

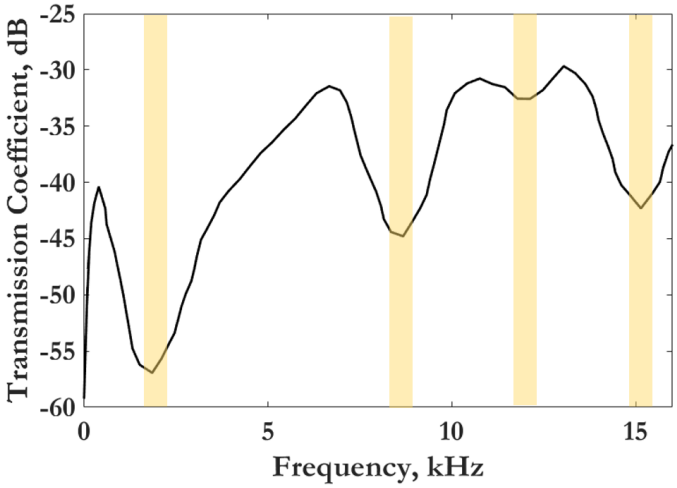
Transmission Coefficient, dB
-25
-30
-35
-40
-45
-50
-55
-60
0
5
10
15
Frequency, kHz

(B-1)

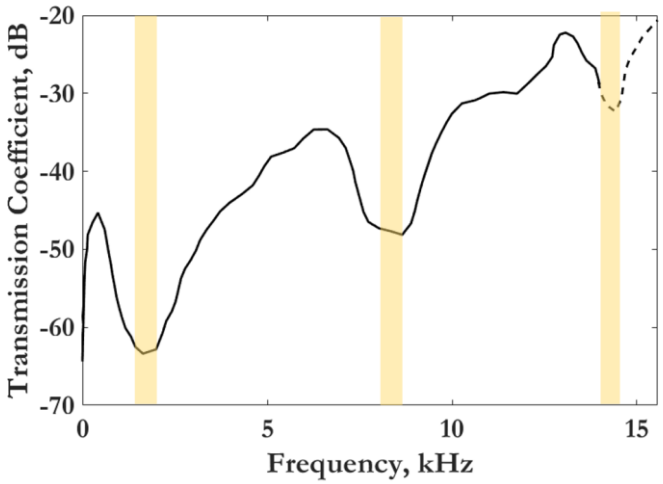
Transmission Coefficient, dB
-20
-30
-40
-50
-60
-70
0
5
10
15
Frequency, kHz

(C-1)

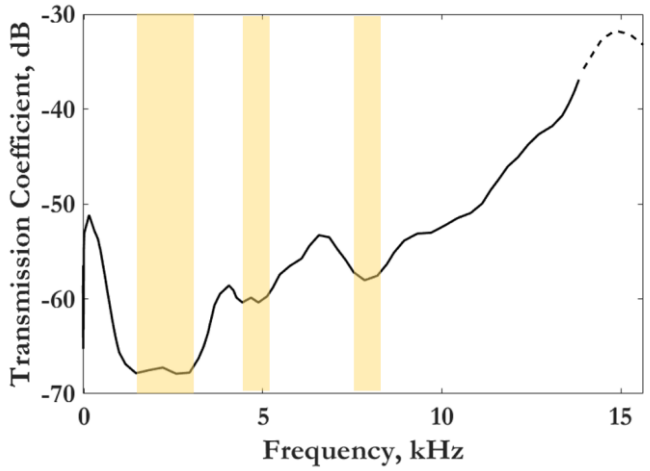
Transmission Coefficient, dB
-30
-40
-50
-60
-70
0
5
10
15
Frequency, kHz

(A-2)

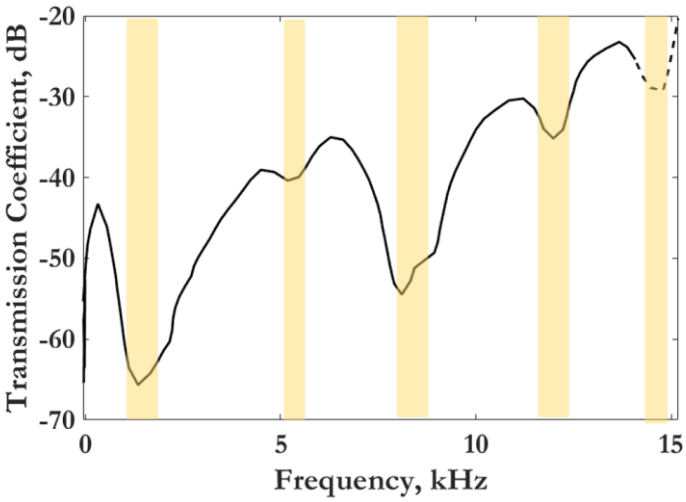
Transmission Coefficient, dB
-20
-30
-40
-50
-60
-70
0
5
10
15
Frequency, kHz

(B-2)

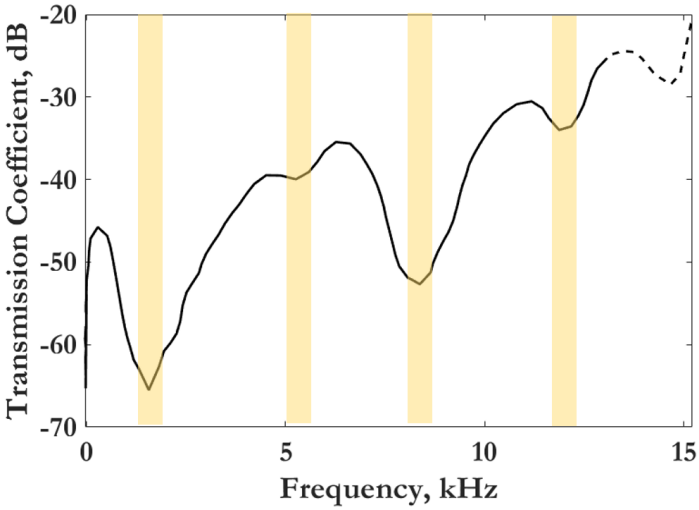
Transmission Coefficient, dB
-20
-30
-40
-50
-60
-70
0
5
10
15
Frequency, kHz

(C-2)

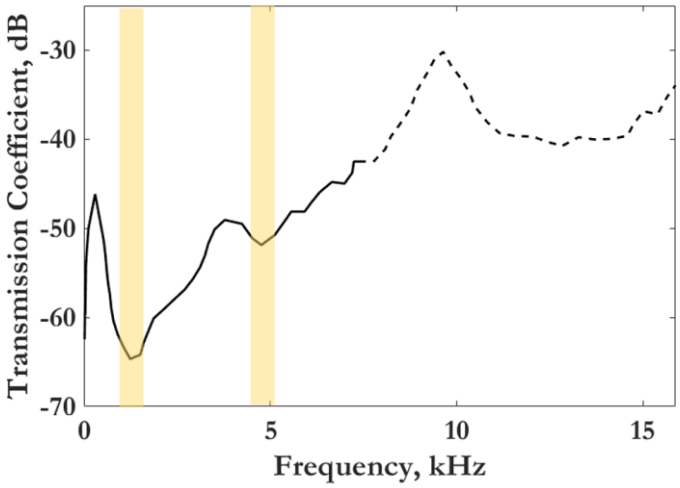
Transmission Coefficient, dB
-30
-40
-50
-60
-70
0
5
10
15
Frequency, kHz

(A-3)

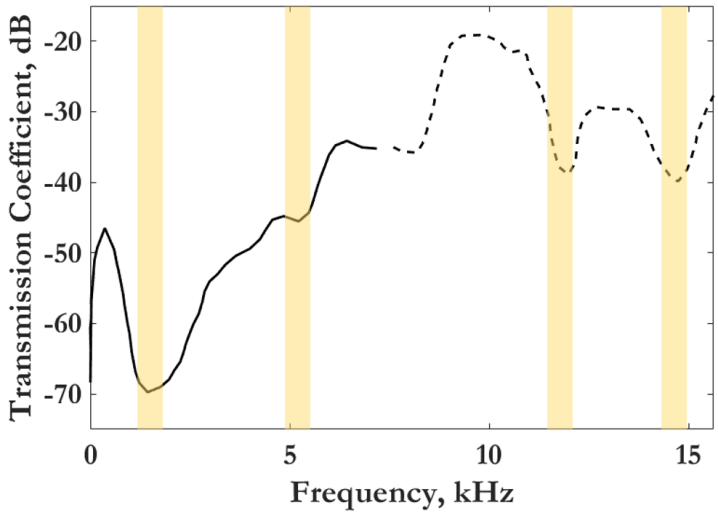

(B-3)

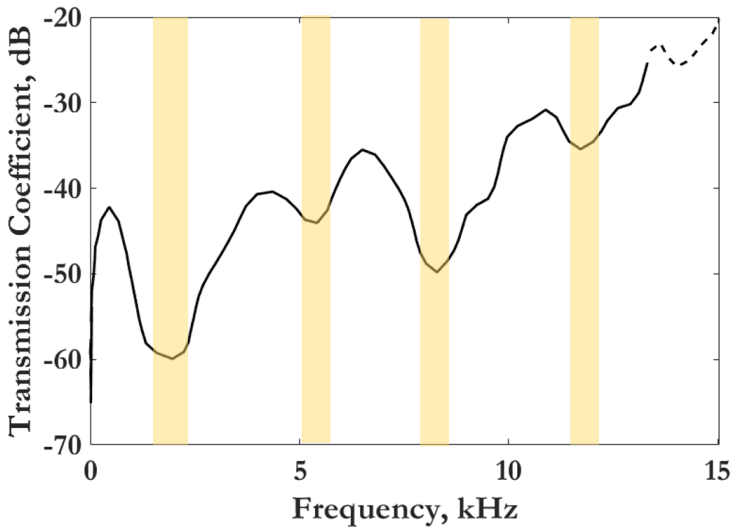

(C-3)

Figure 113. Transmission coefficient (A) Experimental tests (A-1) 50 mm striker with 5.6 N.s impulse; (A-2) 150 mm striker with 13.2 N.s impulse; (A-3) 250 mm striker with 18.6 N.s impulse; (B) FE simulation of the experimental tests ;(A-1) 50 mm striker with 5.5 N.s impulse; (A-2) 150 mm striker with 13.6 N.s impulse; (A-3) 250 mm

striker with 18.5 N.s impulse; (C) 150 mm striker FE simulation ;(A-1) 5.5 N.s impulse (A-2) 13.6 N.s impulse; (A-3) 18.7 N.s impulse

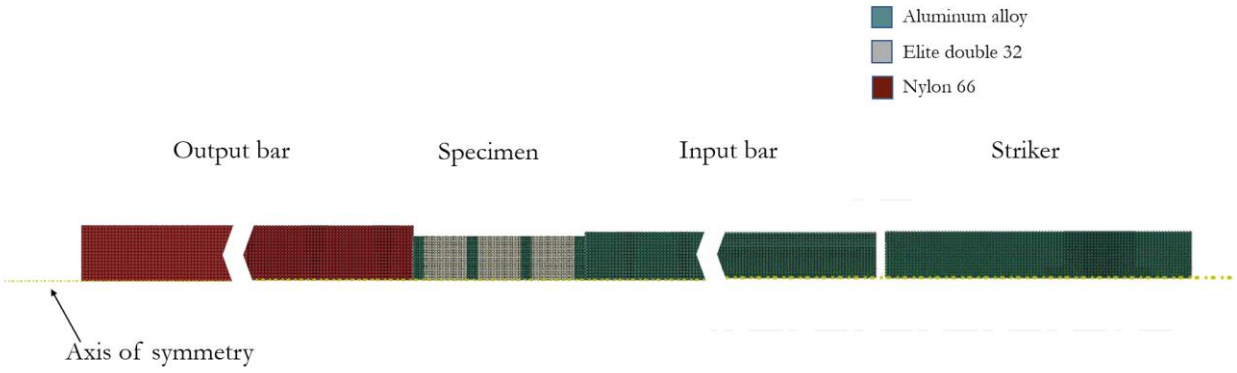

Figure 114. Hybrid SHPB FEM mesh in Abaqus

6.5.3 Impulse-dependent Wave Transmission behavior analysis

In Figure 109 (A, B) the electrodynamic shaker simulation and its corresponding numerical simulation both display low transmission zones around 2 kHz, 3 kHz, 10 kHz, and 14 kHz. The shaker tests are used as a low-amplitude reference to the SHPB that has higher amplitude excitations. To discern the difference between the excitation in these tests, the shaker test chirp signal is converted to a pulse signal. For this, the artificial energy-equivalent pulse needs to be determined. Cook [166] and Klauder et al. [167] proposed the following closed-form formula:

$$p_c(t) = \left|\sqrt{iB_cT_c}\,\frac{\sin(\pi B_c t)}{\pi B_c t}\,e^{i2\pi(f_c t - k_c t^2/2)}\right| \qquad (26)$$

Where T_c is the chirp signal time duration, B_c is the linear frequency bandwidth, f_c the signal starting frequency, k_c is the linear rate of frequency change $= B_c/T_c$.

The resultant energy artificial pulse $p_c(t)$ has a duration of $2/B_c$ and a maximum

amplitude of $\sqrt{B_c T_c}$. According to Klauder et al. [167], $p_c(t)$ is an exponentially decaying Sine function, therefore the central peak carries most of the stored energy. Accordingly, to convert the chirp signal to an impulse, the energy equivalent pulse signal is multiplied by each average of each swept frequency force to get the energy equivalent pulse force time signal. The latter is then integrated over the sweep time to get the impulse. For section 6.4 chirp signal with 21 N amplitude, the calculated impulse is 0.04 N. Note that the shaker test equivalent pulse is approximately 400 times smaller than the hybrid SHPB.

The results plotted in Figure 113 are discussed here to assess the performance of the proposed hybrid SHPB in studying the wave transmission behavior of phononic crystals. Figure 113A-1/B-1 displays the transmission coefficient obtained experimentally and numerically, respectively. Both plots show low transmission zones around 2 and 8 kHz, which are comparable to the electrodynamic shaker results. In Figure 113A-2,3/B-2,3 the impulse increases and two new frequency zones around 5.5 kHz and 12 kHz appear which were not detected in the shaker test results. Note that in SHPB results, the reliable transmission frequencies depend on the striker length (Figure 111). On the other hand, the FE simulation in Figure 113B is free from the limitations of signal-to-noise ratio and striker launching speed. Thus, a striker length was selected with an acceptable frequency range of transmission coefficient validity. Namely, the aluminum striker of 150 mm with an amplitude drop of 14 kHz. FE simulation was performed for 5.5, 13.6, 18.7 N.s impulse using the 150 mm striker at different speeds. The striker speeds were selected to provide comparable impulses to those in Figure 113A and B. For instance, launching the 150 mm striker at 8 m/s generated a 5.5 N.s impulse, and in Figure 113A the 50 mm striker at 12.18 m/s generated a 5.6 N.s speed.

The 150 mm striker FE simulation results are plotted in Figure 113C, where the impulse in Figure 113(C-1,2,3) is equivalent to the impulse in Figure 113(A/B-1,2,3), respectively. When analyzing the transmission coefficients of Figure 113B and Figure 113C, a good agreement is found in the locations of the low transmission zones in the valid frequency range. This consistency in results of the same impulse energy suggests that the impulse is a good parameter to monitor the wave transmission behavior of the considered one dimensional viscoelastic mechanical metamaterial. The new low-frequency zones around 5.5 kHz and 12 kHz observed in Figure 113A/B appear more pronounced in the Figure 113C. The 12 kHz low transmission zone appears in 18.7 N.s impulse in Figure 113(C-3), but it does not appear in the 250 mm striker with the same impulse due to an amplitude drop caused by the length of the striker. All the results from Figure 109 and Figure 113 suggest that the behavior of the viscoelastic phononic crystals is impulse dependent and that the hybrid SHPB is a fitting apparatus to investigate this impulse-dependent behavior.

6.6 Conclusion

Over the last years, investigation of the nonlinear wave transmission behavior of viscoelastic phononic crystals has been of interest due to their advantageous potential application in mechanical wave control. Electrodynamic shaker and piezoelectric actuators have been used to investigate the wave motion through these materials. However, the nonlinear behavior of the viscoelastic constituent of these materials has made it difficult for the proper identification with low amplitude tests. This study proposes a modified SHPB setup to investigate the impulse-dependent behavior of viscoelastic phononic crystals. The proposed modified SHPB setup is a hybrid SHPB with an aluminum input bar and a nylon output bar to bypass the conventional SHPB limitations such as high signal-to-noise ratios and low incident impulses. The

aluminum bar permits high incident impulses to reach the specimen, while the nylon bar allows a higher signal to noise reading. There is a good agreement between the low transmission zones observed in the shaker test and their counterparts in the SHPB tests. Nevertheless, new low transmission zones appear in the SHPB high impulse test that does not show in the shaker test with linear harmonic excitation.

The corresponding FE simulations demonstrate low transmission zones at different launching conditions with good agreement with their experimental counterparts in terms of their function of impulse. The wave propagation in viscoelastic phononic crystals is thus impulse dependent. Moreover, results reveal that the hybrid SHPB setup is a fitting experimental investigation tool to investigate viscoelastic phononic crystals. This study therefore opens the door to more investigation of phononic crystals using different types of SHPB setups such as tension torsion and shear SHPB. It also expands the SHPB tool from the high strain material testing sphere to the emerging field of nonlinear wave characteristics of mechanical metamaterials.

CHAPTER 7: CONCLUSION

7.1 Summary

In this dissertation, different types of Mechanical Metamaterials were investigated experimentally and numerically for their vibration attenuation properties. Viscoelastic phononic crystals and thin plate host structures with locally resonant inserts were the focus of this study. For the viscoelastic phononic crystals, the analytical dispersion relation of an arbitrary multilayered crystal was computed using the transfer matrix method. Analytical results showed that the periodically arranged metals and viscoelastic materials permit the formation of band gaps in the low-frequency range. However, the analytical model did not encompass the inherent damping effect of the viscoelastic material on the overall vibration attenuation. On the other hand, the vibration attenuation of the viscoelastic phononic crystals was dependent on their unit cell geometry. A multiobjective genetic algorithm optimization was conducted on the geometric parameters for a targeted low-frequency range. The multiobjective optimization allowed for the consideration of the attenuation due to the MM inertia versus the Bragg scattering effect resulting from the periodicity of the MM. The fitness function of the optimization was based on an FEM. This modeled the viscoelastic material damping as frequency-dependent, which is key for an accurate representation of the response of the viscoelastic phononic crystal in the function of frequency. The FE results are validated by experimental testing. The optimization successfully generated an optimal phononic crystal with a low transmission zone in the targeted frequency range, which was validated numerically and experimentally. The main outcomes for the low amplitude viscoelastic phononic crystal study are:

- The Analytical dispersion relation using the transfer Matrix method shows potential pass bands and stop bands but does not account for the inherent

damping effect of the constituting viscoelastic materials.

- Pairing low modulus polymeric material with high modulus metals improves the performance of phononic crystals in low-frequency vibration attenuation.
- Extensive investigation of the complex modulus of viscoelastic materials allows a more accurate representation of the frequency-dependent transmission behavior of viscoelastic phononic crystals.
- The FEM of viscoelastic phononic crystals offered a good prediction of the location of the low transmission zone.
- The optimal specimen validated numerically and experimentally shows that a FEM based on the loss and storage modulus on the viscoelastic material gives a good prediction on the frequency-dependent PC behavior.
- The multiobjective optimization algorithm developed for the viscoelastic phononic crystal shows that considering a mass cost value along with the vibration attenuation cost value allows generation of a Pareto front of different optimal specimens and avoids the yielding of a massive specimen with large layer thicknesses which is undesirable in practice.

The second vibration attenuation mechanism studied in this dissertation was the local resonance. Zigzag resonants embedded in thin aluminum plates were optimized to generate a low transmission zone to replace an otherwise resonant frequency range. Two zigzags were cut out of the host structure for minimum structural intervention but positioned geometrically for maximum efficiency of vibration attenuation. The optimization generated optimal specimens were validated numerically and experimentally. This optimization was reliable and could be used as a tool to tune host structures for their structural dynamic service needs. The main outcomes for the locally resonant plate study were:

- The Aluminum plate genetic algorithm optimization is a tool for tuning the band gap of plates without compromising their structural stability.
- The optimization of zigzag plates generated optimal specimens that have been validated numerically and experimentally.

The main focus of this study was to revitalize the practical applications of viscoelastic MMs since it explored nonlinear experimental studies on composites. However, the conventional experimental methods are limited to the identification of small amplitude low transmission zones. Thus, this study proposed a detailed procedure to allow the experimental identification of amplitude-dependent waves of transmission of viscoelastic MMs. A modified SHPB setup is therefore proposed to adapt the conventional SHPB to study the impulse-dependent behavior of viscoelastic phononic crystals. A new hybrid SHPB apparatus is proposed with an Aluminum alloy input bar and a Nylon66 output bar to bypass the SHPB limitations of the low incident impulse of the polymeric SHPB, and the high signal-to-noise ratios in the metallic SHPB, respectively. Low transmission zones identified in the low amplitude shaker test corresponded to the hybrid SHPB zones. Nevertheless, new low transmission zones emerged in the high amplitude SHPB tests which did not appear in the shaker test. In conclusion, the viscoelastic phononic crystals vibration transmission behavior was amplitude-dependent, and the proposed apparatus expanded the SHPB tool from the high strain material testing sphere to the emerging field of nonlinear wave characteristics of mechanical metamaterials. The main outcomes for the high amplitude viscoelastic phononic crystal study were:

- The hybrid SHPB with a metallic input bar and a polymeric output bar allows the adaptation of an impact-based test on viscoelastic mechanical metamaterial for wave propagation characterization.

- Viscoelastic phononic materials are impulse dependent, and new low transmission zones appear at a higher amplitude which is not observed using conventional methods.
- The incident wave suffers amplitude drops which prevents acquisition of accurate results for higher frequencies. The SHPB apparatus for viscoelastic MMs testing should have a high launching speed and a short striker.
- New low transmission zones appearing at a higher amplitude experimentally are predicted numerically with a full hybrid SHPB setup/phononic crystal specimen FE model.

7.2 Future investigation and recommendations

The outcomes of the current thesis lead the way for the following research pursuits:

- Investigation of closed-form analytical solutions for wave propagation in viscoelastic phononic crystals to better predict the vibration attenuation behavior of nonlinear metamaterials. Moreover, incorporating an analytical model as a fitness function in the optimization process reduced the computational time and effort required to carry out the optimization with successful convergence.
- Use of a full 3D model to provide information on the optimization if the specimen was subjected to multiple excitation forces in different directions.
- Investigate the amplitude-dependent wave transmission behavior in 2D and 3D viscoelastic phononic crystals.
- Increase the reliable transmission coefficient frequencies in the SHPB by adapting the experimental setup of SHPB to reduce the impulse duration resulting in a high sharp impulse.
- Investigation wave transmission for deformed 2D and 3D MMs.

REFERENCES

[1] Z. Liu, X. Zhang, Y. Mao, Y.Y. Zhu, Z. Yang, C.T. Chan, P. Sheng, Locally resonant sonic materials, Science (80-.). 289 (2000) 1734–1736. doi:10.1126/science.289.5485.1734.

[2] P. Gudmundson, M. Åberg, The usage of standard finite element codes for computation of dispersion relations in materials with periodic microstructure, J. Acoust. Soc. Am. 102 (1997) 2007–2013. http://link.aip.org/link/jasman/v102/i4/p2007/s1.

[3] S. Minagawa, S. Nemat-Nasser, On harmonic waves in layered composites, J. Appl. Mech. Trans. ASME. 44 (1977) 689–695. doi:10.1115/1.3424158.

[4] S. Minagawa, S. Nemat-Nasser, M. Yamada, Finite element analysis of harmonic waves in layered and fibre-reinforced composites, Int. J. Numer. Methods Eng. 17 (1981) 1335–1353. doi:https://doi.org/10.1002/nme.1620170905.

[5] J.H. Lee, J.P. Singer, E.L. Thomas, Micro-/nanostructured mechanical metamaterials, Adv. Mater. 24 (2012) 4782–4810. doi:10.1002/adma.201201644.

[6] M. Kadic, T. Bückmann, R. Schittny, M. Wegener, Metamaterials beyond electromagnetism, Reports Prog. Phys. 76 (2013) 126501. doi:10.1088/0034-4885/76/12/126501.

[7] M. Wegener, Metamaterials beyond optics, Science (80-.). 342 (2013) 939–940. doi:10.1126/science.1246545.

[8] M. Sigalas, E.N. Economou, Band structure of elastic waves in two dimensional systems, Solid State Commun. 86 (1993) 141–143. doi:10.1016/0038-1098(93)90888-T.

[9] M.S. Kushwaha, P. Halevi, L. Dobrzynski, B. Djafari-Rouhani, Acoustic band structure of periodic elastic composites, Phys. Rev. Lett. 71 (1993) 2022–2025. doi:10.1103/PhysRevLett.71.2022.

[10] M. Ruzzene, F. Scarpa, Directional and band-gap behavior of periodic auxetic lattices, Phys. Status Solidi Basic Res. 242 (2005) 665–680. doi:10.1002/pssb.200460385.

[11] M. Maldovan, E.L. Thomas, Simultaneous complete elastic and electromagnetic band gaps in periodic structures, Appl. Phys. B Lasers Opt. 83 (2006) 595–600. doi:10.1007/s00340-006-2241-y.

[12] J.R. Willis, A polarization approach to the scattering of elastic waves-II. Multiple scattering from inclusions, J. Mech. Phys. Solids. 28 (1980) 307–327. doi:10.1016/0022-5096(80)90022-8.

[13] G.W. Milton, J.R. Willis, On modifications of Newton's second law and linear continuum elastodynamics, Proc. R. Soc. A Math. Phys. Eng. Sci. 463 (2007) 855–880. doi:10.1098/rspa.2006.1795.

[14] G.W. Milton, M. Briane, J.R. Willis, On cloaking for elasticity and physical equations with a transformation invariant form, New J. Phys. 8 (2006). doi:10.1088/1367-2630/8/10/248.

[15] T. Bückmann, M. Thiel, M. Kadic, R. Schittny, M. Wegener, An elasto-mechanical unfeelability cloak made of pentamode metamaterials, Nat. Commun. 5 (2014). doi:10.1038/ncomms5130.

[16] S. Zhang, C. Xia, N. Fang, Broadband acoustic cloak for ultrasound waves, Phys. Rev. Lett. 106 (2011). doi:10.1103/PhysRevLett.106.024301.

[17] F. Casadei, B.S. Beck, K. a. Cunefare, M. Ruzzene, Vibration control of plates through hybrid configurations of periodic piezoelectric shunts, J. Intell. Mater.

Syst. Struct. 23 (2012) 1169–1177. doi:10.1177/1045389X12443014.

[18] F. Casadei, L. Dozio, M. Ruzzene, K.A. Cunefare, Periodic shunted arrays for the control of noise radiation in an enclosure, J. Sound Vib. 329 (2010) 3632–3646. doi:10.1016/j.jsv.2010.04.003.

[19] J.O. Vasseur, A.C. Hladky-Hennion, B. Djafari-Rouhani, F. Duval, B. Dubus, Y. Pennec, P.A. Deymier, Waveguiding in two-dimensional piezoelectric phononic crystal plates, J. Appl. Phys. 101 (2007). doi:10.1063/1.2740352.

[20] I.E. Psarobas, Viscoelastic response of sonic band-gap materials, Phys. Rev. B - Condens. Matter Mater. Phys. 64 (2001). doi:10.1103/PhysRevB.64.012303.

[21] P.J. Wei, Y.P. Zhao, The influence of viscosity on band gaps of 2D phononic crystal, Mech. Adv. Mater. Struct. 17 (2010) 383–392. doi:10.1080/15376494.2010.483320.

[22] M.I. Hussein, M.J. Frazier, Band structure of phononic crystals with general damping, J. Appl. Phys. 108 (2010) 1–12. doi:10.1063/1.3498806.

[23] B. Merheb, P.A. Deymier, M. Jain, M. Aloshyna-Lesuffleur, S. Mohanty, A. Berker, R.W. Greger, Elastic and viscoelastic effects in rubber/air acoustic band gap structures: A theoretical and experimental study, J. Appl. Phys. 104 (2008). doi:10.1063/1.2980330.

[24] Y.P. Zhao, P.J. Wei, The band gap of 1D viscoelastic phononic crystal, Comput. Mater. Sci. 46 (2009) 603–606. doi:10.1016/j.commatsci.2009.03.040.

[25] J. Cabaret, V. Tournat, P. Béquin, Amplitude-dependent phononic processes in a diatomic granular chain in the weakly nonlinear regime, Phys. Rev. E - Stat. Nonlinear, Soft Matter Phys. 86 (2012). doi:10.1103/PhysRevE.86.041305.

[26] J.D. Achenbach, Wave Propagation in Lamellar Composite Materials, J. Acoust. Soc. Am. 43 (1968) 1451–1452. doi:10.1121/1.1911010.

[27] L.M. Brekhovskikh, Waves in layered media, 2nd edition, IEEE Antennas Propag. Soc. Newsl. 23 (1981) 38. doi:10.1109/MAP.1981.27557.

[28] J. He, B. Djafari-Rouhani, J. Sapriel, Theory of light scattering by longitudinal-acoustic phonons in superlattices, Phys. Rev. B. 37 (1988) 4086–4098. doi:10.1103/PhysRevB.37.4086.

[29] G.H. Cocoletzi, Band Structure for the Propagation of Elastic Waves in Superlattices, J. Acoust. Soc. Am. 95 (1994) 86–90. doi:10.1121/1.408301.

[30] M.I. Hussein, G.M. Hulbert, R.A. Scott, Dispersive elastodynamics of 1D banded materials and structures: Analysis, J. Sound Vib. 289 (2006) 779–806. doi:10.1016/j.jsv.2005.02.030.

[31] S. Tamura, J.P. Wolfe, Acoustic phonons in multiconstituent superlattices, Phys. Rev. B. 38 (1988) 5610–5614. doi:10.1103/PhysRevB.38.5610.

[32] A. Nougaoui, B.D. Rouhani, Elastic waves in periodically layered infinite and semi-infinite anisotropic media, Surf. Sci. 185 (1987) 125–153. doi:10.1016/S0039-6028(87)80618-0.

[33] A. Nougaoui, B. Djafari Rouhani, Complex band structure of acoustic waves in superlattices, Surf. Sci. 199 (1988) 623–637. doi:10.1016/0039-6028(88)90926-0.

[34] J. Sapriel, B.D. Rouhani, Vibrations in superlattices, Surf. Sci. Rep. 10 (1989) 189–275. doi:10.1016/0167-5729(89)90003-4.

[35] A.M.B. Braga, G. Herrmann, Floquet Waves In Anisotropic Periodically Layered Composites, J. Acoust. Soc. Am. 91 (1992) 1211–1227. doi:10.1121/1.402505.

[36] A.H. Nayfeh, The general problem of elastic wave propagation in multilayered anisotropic media, J. Acoust. Soc. Am. 89 (1991) 1521–1531.

doi:10.1121/1.400988.

[37] A.B.M. Tahidul Haque, R.F. Ghachi, W.I. Alnahhal, A. Aref, J. Shim, Sagittal plane waves in infinitely periodic multilayered composites composed of alternating viscoelastic and elastic solids, J. Appl. Mech. Trans. ASME. 85 (2018) 041001. doi:10.1115/1.4039039.

[38] A.B.M.T. Haque, R.F. Ghachi, W.I. Alnahhal, A. Aref, J. Shim, Generalized spatial aliasing solution for the dispersion analysis of infinitely periodic multilayered composites using the finite element method, J. Vib. Acoust. Trans. ASME. 139 (2017) 051010. doi:10.1115/1.4036469.

[39] K. Tanaka, A. Kon-no, Harmonic Viscoelastic Waves Propagating Normal To the Layers of Laminated Media, Bull. JSME. 23 (1980) 1092–1099. doi:10.1299/jsme1958.23.1092.

[40] B. Djafari-Rouhani, L. Dobrzynski, O.H. Duparc, R.E. Camley, A.A. Maradudin, Sagittal elastic waves in infinite and semi-infinite superlattices, Phys. Rev. B. 28 (1983) 1711–1720. doi:10.1103/PhysRevB.28.1711.

[41] T. Naciri, P. Navi, A. Ehrlacher, Harmonic wave propagation in viscoelastic heterogeneous materials Part I: Dispersion and damping relations, Mech. Mater. 18 (1994) 313–333. doi:10.1016/0167-6636(94)90042-6.

[42] S. Mukherjee, E.H. Lee, Dispersion relations and mode shapes for waves in laminated viscoelastic composites by variational methods, Int. J. Solids Struct. 14 (1978) 1–13. doi:10.1016/0020-7683(78)90061-6.

[43] Y. Chevalier, Dispersion of Harmonic Waves in Elastic and Viscoelastic Periodic Composite Materials, (1988) 260–268. doi:10.1007/978-3-642-83508-7_27.

[44] G.A. Hegemier, T.C. Bache, A general continuum theory with miorostructure

for wave propagation in elastic laminated composites, J. Appl. Mech. Trans. ASME. 41 (1974) 101–105. doi:10.1115/1.3423202.

[45] G.A. Hegemier, A.H. Nayfeh, A continuum theory for wave propagation in laminated composites case 1: Propagation normal to the laminates, J. Appl. Mech. Trans. ASME. 40 (1973) 503–510. doi:10.1115/1.3423013.

[46] J.A. G. Herrmann, on Dynamic Theories of Fiber-Reinforced Composites, in: 8th Struct. Dyn. Mater. Conf., 1967. doi:10.2514/6.1967-1112.

[47] M. Stern, A. Bedford, Wave propagation in elastic laminates using a multi-continuum theory, Acta Mech. 15 (1972) 21–38. doi:10.1007/BF01177284.

[48] C.T. Sun, J.D. Achenbach, G. Herrmann, Continuum theory for a laminated medium, J. Appl. Mech. Trans. ASME. 35 (1964) 467–475. doi:10.1115/1.3601237.

[49] H. Murakami, A mixture theory for wave propagation in angle-ply laminates: Part 1: Theory, J. Appl. Mech. Trans. ASME. 52 (1985) 331–337. doi:10.1115/1.3169049.

[50] H. Murakami, A. Akiyama, A mixture theory for wave propagation in angle-ply laminates: Part 2: Application, J. Appl. Mech. Trans. ASME. 52 (1985) 338–344. doi:10.1115/1.3169050.

[51] H. Murakami, A. Maewal, G.A. Hegemier, Mixture theory for longitudinal wave propagation in unidirectional composites with cylindrical fibers of arbitrary cross section-I. Formulation, Int. J. Solids Struct. 15 (1979) 325–334. doi:10.1016/0020-7683(79)90011-8.

[52] W. Kohn, J.A. Krumhansl, E.H. Lee, Variational Methods for Dispersion Relations and Elastic Properties of Composite Materials, J. Appl. Mech. 39 (1972) 327–336. doi:10.1115/1.3422679.

[53] S. Nemat-Nasser, Harmonic Waves in Layered Composites, J. Appl. Mech. 39 (1972) 850–852. doi:10.1115/1.3422814.

[54] N. Guarín-Zapata, J. Gomez, Evaluation of the Spectral Finite Element Method with the Theory of Phononic Crystals, J. Comput. Acoust. 23 (2015) 1550004. doi:10.1142/S0218396X15500046.

[55] P. Wang, J. Shim, K. Bertoldi, Effects of geometric and material nonlinearities on tunable band gaps and low-frequency directionality of phononic crystals, Phys. Rev. B. 88 (2013) 14304. doi:10.1103/PhysRevB.88.014304.

[56] A. Bayat, F. Gordaninejad, A magnetically field-controllable phononic crystal, Act. Passiv. Smart Struct. Integr. Syst. 2014. 9057 (2014) 905713. doi:10.1117/12.2046345.

[57] D. Mousanezhad, S. Babaee, R. Ghosh, E. Mahdi, K. Bertoldi, A. Vaziri, Honeycomb phononic crystals with self-similar hierarchy, Phys. Rev. B - Condens. Matter Mater. Phys. 92 (2015). doi:10.1103/PhysRevB.92.104304.

[58] J. Shim, P. Wang, K. Bertoldi, Harnessing instability-induced pattern transformation to design tunable phononic crystals, Int. J. Solids Struct. 58 (2015) 52–61. doi:10.1016/j.ijsolstr.2014.12.018.

[59] L. Wang, K. Bertoldi, Mechanically tunable phononic band gaps in three-dimensional periodic elastomeric structures, Int. J. Solids Struct. 49 (2012) 2881–2885. doi:https://doi.org/10.1016/j.ijsolstr.2012.05.008.

[60] J. Wen, G. Wang, D. Yu, H. Zhao, Y. Liu, X. Wen, Study on the vibration band gap and vibration attenuation property of phononic crystals, Sci. China, Ser. E Technol. Sci. 51 (2008) 85–99. doi:10.1007/s11431-008-0008-x.

[61] Y.L. Wang, M.W. Chen, Z.D. Wang, Study on band gap structure of one dimensional phononic crystals, Adv. Mater. Res. 152–153 (2011) 1696–1699.

doi:10.4028/www.scientific.net/AMR.152-153.1696.

[62] F. Casadei, K. Bertoldi, Harnessing fluid-structure interactions to design self-regulating acoustic metamaterials, J. Appl. Phys. 115 (2014). doi:10.1063/1.4862643.

[63] P.G. Domadiya, E. Manconi, M. Vanali, L.V. Andersen, A. Ricci, Numerical and experimental investigation of stop-bands in finite and infinite periodic one-dimensional structures, JVC/Journal Vib. Control. 22 (2016). doi:10.1177/1077546314537863.

[64] W. Ji-Hong, S. Hui-Jie, Y. Dian-Long, W. Xi-Sen, Theoretical and Experimental Investigation of Flexural Wave Propagating in a Periodic Pipe with Fluid-Filled Loading, Chinese Phys. Lett. 27 (2010) 114301. doi:10.1088/0256-307X/27/11/114301.

[65] Z. Chen, Y. Yang, Z. Lu, Y. Luo, Broadband characteristics of vibration energy harvesting using one-dimensional phononic piezoelectric cantilever beams, Phys. B Condens. Matter. 410 (2013) 5–12. doi:https://doi.org/10.1016/j.physb.2012.10.029.

[66] S. Shan, S.H. Kang, P. Wang, C. Qu, S. Shian, E.R. Chen, K. Bertoldi, Harnessing multiple folding mechanisms in soft periodic structures for tunable control of elastic waves, Adv. Funct. Mater. 24 (2014) 4935–4942. doi:10.1002/adfm.201400665.

[67] Y. He, X. Jin, Vibrational properties of the phononic crystal structural cavity, J. Vibroengineering. (2015) 1079–1090.

[68] P. Wang, F. Casadei, S. Shan, J.C. Weaver, K. Bertoldi, Harnessing buckling to design tunable locally resonant acoustic metamaterials, Phys. Rev. Lett. 113 (2014). doi:10.1103/PhysRevLett.113.014301.

[69] T. Delpero, S. Schoenwald, A. Zemp, A. Bergamini, Structural engineering of three-dimensional phononic crystals, J. Sound Vib. 363 (2016) 156–165. doi:10.1016/j.jsv.2015.10.033.

[70] S. Krödel, N. Thomé, C. Daraio, Wide band-gap seismic metastructures, Extrem. Mech. Lett. 4 (2015) 111–117. doi:10.1016/j.eml.2015.05.004.

[71] G.W. Leppelmeier, Experimental Verification of Dispersion Relations for Layered Composites, (2014) 89–91.

[72] T. HAYASHI, Y. MORIMOTO, M. SERIKAWA, K. TOKUDA, T. TANAKA, Experimental Study on Cut-Off Phenomenon for Layered Composite, Bull. JSME. 26 (1983) 23–29. doi:10.1299/jsme1958.26.23.

[73] M. Meidani, E. Kim, F. Li, J. Yang, D. Ngo, Tunable evolutions of wave modes and bandgaps in quasi-1D cylindrical phononic crystals, J. Sound Vib. 334 (2015) 270–281. doi:10.1016/j.jsv.2014.09.01.

[74] B. Manzanares-Martínez, J. Sánchez-Dehesa, A. Håkansson, F. Cervera, F. Ramos-Mendieta, Experimental evidence of omnidirectional elastic bandgap in finite one-dimensional phononic systems, Appl. Phys. Lett. 85 (2004) 154–156. doi:10.1063/1.1766074.

[75] Y. Dian-Long, L. Yao-Zong, Q. Jing, Z. Hong-Gang, L. Zhi-Ming, Experimental and Theoretical Research on the Vibrational Gaps in Two-Dimensional Three-Component Composite Thin Plates, Chinese Phys. Lett. 22 (2005) 1958–1960. doi:10.1088/0256-307x/22/8/038.

[76] C. Pachiu, EXPERIMENTAL OBSERVATIONS IN 2D PHONONIC STRUCTURE WITH GRANULAR CRYSTALS, (n.d.) 299–302.

[77] P. Celli, S. Gonella, Laser-enabled experimental wavefield reconstruction in two-dimensional phononic crystals, J. Sound Vib. 333 (2014) 114–123.

doi:10.1016/j.jsv.2013.09.001.

[78] H.W. Dong, Y.S. Wang, C. Zhang, Inverse design of high-Q wave filters in two-dimensional phononic crystals by topology optimization, Ultrasonics. 76 (2017) 109–124. doi:10.1016/j.ultras.2016.12.018.

[79] A. Merkel, V. Tournat, V. Gusev, Elastic waves in noncohesive frictionless granular crystals, Ultrasonics. 50 (2010) 133–138. doi:10.1016/j.ultras.2009.09.032.

[80] A. Merkel, V. Tournat, V. Gusev, Experimental evidence of rotational elastic waves in granular phononic crystals, Phys. Rev. Lett. 107 (2011) 1–5. doi:10.1103/PhysRevLett.107.225502.

[81] R. Feng, K. Liu, Tuning the band-gap of phononic crystals with an initial stress, Phys. B Condens. Matter. 407 (2012) 2032–2036. doi:10.1016/j.physb.2012.01.135.

[82] R. Feng, K. Liu, Tuning of band-gap of phononic crystals with initial confining pressure, Phys. B Condens. Matter. 407 (2012) 2032–2036. doi:10.1016/j.physb.2012.01.135.

[83] E.B. Herbold, J. Kim, V.F. Nesterenko, S.Y. Wang, C. Daraio, Pulse propagation in a linear and nonlinear diatomic periodic chain: Effects of acoustic frequency band-gap, Acta Mech. 205 (2009) 85–103. doi:10.1007/s00707-009-0163-6.

[84] C. Daraio, V.F. Nesterenko, E.B. Herbold, S. Jin, Strongly nonlinear waves in a chain of Teflon beads, Phys. Rev. E - Stat. Nonlinear, Soft Matter Phys. 72 (2005) 1–9. doi:10.1103/PhysRevE.72.016603.

[85] D. Ngo, D. Khatri, C. Daraio, Highly nonlinear solitary waves in chains of ellipsoidal particles, Phys. Rev. E - Stat. Nonlinear, Soft Matter Phys. 84 (2011) 26610. doi:10.1103/PhysRevE.84.026610.

[86] J. Yang, C. Daraio, Frequency- and Amplitude-Dependent Transmission of Stress Waves in Curved One-Dimensional Granular Crystals Composed of Diatomic Particles, Exp. Mech. 53 (2013) 469–483. doi:10.1007/s11340-012-9652-y.

[87] J. Yang, M. Sutton, Nonlinear wave propagation in a hexagonally packed granular channel under rotational dynamics, Int. J. Solids Struct. 77 (2015) 65–73. doi:10.1016/j.ijsolstr.2015.07.017.

[88] J. Renno, N. Søndergaard, S. Sassi, M.R. Paurobally, Wave Scattering and Power Flow in Straight-Helical-Straight Waveguide Structure, Int. J. Appl. Mech. 11 (2019). doi:10.1142/S1758825119500753.

[89] S. Li, Y. Dou, T. Chen, Z. Wan, Z. Guan, A novel metal-matrix phononic crystal with a low-frequency, broad and complete, locally-resonant band gap, Mod. Phys. Lett. B. 32 (2018). doi:10.1142/S0217984918502214.

[90] Z. Liu, C.T. Chan, P. Sheng, Three-component elastic wave band-gap material, Phys. Rev. B - Condens. Matter Mater. Phys. 65 (2002) 1651161–1651166. doi:10.1103/PhysRevB.65.165116.

[91] Y. Liu, D. Yu, H. Zhao, J. Wen, X. Wen, Theoretical study of two-dimensional phononic crystals with viscoelasticity based on fractional derivative models, J. Phys. D. Appl. Phys. 41 (2008). doi:10.1088/0022-3727/41/6/065503.

[92] B. Merheb, P.A. Deymier, K. Muralidharan, J. Bucay, M. Jain, M. Aloshyna-Lesuffleur, R.W. Greger, S. Mohanty, A. Berker, Viscoelastic effect on acoustic band gaps in polymer-fluid composites, Model. Simul. Mater. Sci. Eng. 17 (2009). doi:10.1088/0965-0393/17/7/075013.

[93] Y. Zhang, Z.Q. Ni, L. Han, Z.M. Zhang, H.Y. Chen, Study of improved plane wave expansion method on phononic crystal, Optoelectron. Adv. Mater. Rapid

Commun. 5 (2011) 870–873.

[94] H.Y. Hwang, J.W. Lee, J. Yang, C.W. Shul, E. Kim, Sandwich-Structured Woodpile Metamaterials for Impact Mitigation, Int. J. Appl. Mech. 10 (2018). doi:10.1142/S1758825118500783.

[95] S. Muhammad, S. Wang, F. Li, C. Zhang, Bandgap enhancement of periodic nonuniform metamaterial beams with inertial ampli fi cation mechanisms, (2020). doi:10.1177/1077546319895630.

[96] B. Chen, O. Shiryayev, N. Vahdati, A. El-Sinawi, Validation of a Modeling Tool for In-Plane Longitudinal Resonators with Zigzag Topology, Int. J. Appl. Mech. 11 (2019).

[97] P. Zhang, A.C. To, Broadband wave filtering of bioinspired hierarchical phononic crystal, Appl. Phys. Lett. 102 (2013). doi:10.1063/1.4799171.

[98] X. Yuan, Z.H. Zhu, Wave reflection in piezoelectric half-plane, Int. J. Appl. Mech. 5 (2013). doi:10.1142/S1758825113500142.

[99] P. Grootenhuis, The control of vibrations with viscoelastic materials, J. Sound Vib. 11 (1970) 421–433. doi:10.1016/S0022-460X(70)80004-9.

[100] R.F. Lyon, Human and machine hearing: Extracting meaning from sound, Cambridge University Press, 2017. doi:10.1017/9781139051699.

[101] R. Huang, S. Zheng, Z. Liu, T.Y. Ng, Recent Advances of the Constitutive Models of Smart Materials - Hydrogels and Shape Memory Polymers, 2020. doi:10.1142/S1758825120500143.

[102] S. Zheng, Z. Li, Z. Liu, The fast homogeneous diffusion of hydrogel under different stimuli, Int. J. Mech. Sci. 137 (2018) 263–270. doi:10.1016/j.ijmecsci.2018.01.029.

[103] H. Meng, J. Wen, H. Zhao, X. Wen, Optimization of locally resonant acoustic

metamaterials on underwater sound absorption characteristics, J. Sound Vib. 331 (2012) 4406–4416. doi:10.1016/j.jsv.2012.05.027.

[104] H. Zhao, J. Wen, D. Yu, X. Wen, Low-frequency acoustic absorption of localized resonances: Experiment and theory, J. Appl. Phys. 107 (2010). doi:10.1063/1.3284943.

[105] Z.J. Wu, F.M. Li, Y.Z. Wang, Vibration band gap properties of periodic Mindlin plate structure using the spectral element method, Meccanica. 49 (2014) 725–737. doi:10.1007/s11012-013-9822-8.

[106] J. Dong, Q.H. Qin, Y. Xiao, Nelder-Mead Optimization of Elastic Metamaterials via Machine-Learning-Aided Surrogate Modeling, Int. J. Appl. Mech. 12 (2020) 1–17. doi:10.1142/S1758825120500118.

[107] M.I. Hussein, K. Hamza, G.M. Hulbert, R.A. Scott, K. Saitou, Multiobjective evolutionary optimization of periodic layered materials for desired wave dispersion characteristics, Struct. Multidiscip. Optim. 31 (2006) 60–75. doi:10.1007/s00158-005-0555-8.

[108] M.I. Hussein, G.M. Hulbert, R.A. Scott, Dispersive elastodynamics of 1D banded materials and structures: Design, J. Sound Vib. 307 (2007) 865–893. doi:10.1016/j.jsv.2007.07.021.

[109] H.W. Dong, X.X. Su, Y.S. Wang, C. Zhang, Topology optimization of two-dimensional asymmetrical phononic crystals, Phys. Lett. Sect. A Gen. At. Solid State Phys. 378 (2014) 434–441. doi:10.1016/j.physleta.2013.12.003.

[110] Z.C. He, G.Y. Zhang, L. Deng, E. Li, G.R. Liu, Topology optimization using node-based smoothed finite element method, Int. J. Appl. Mech. 7 (2015). doi:10.1142/S1758825115500854.

[111] O. Sigmund, J. Sondergaard Jensen, Systematic design of phononic band-gap

materials and structures by topology optimization, Philos. Trans. R. Soc. A Math. Phys. Eng. Sci. 361 (2003) 1001–1019. doi:10.1098/rsta.2003.1177.

[112] H. Abu Qdais, K.B. Hani, N. Shatnawi, Modeling and optimization of biogas production from a waste digester using artificial neural network and genetic algorithm, Resour. Conserv. Recycl. 54 (2010) 359–363. doi:doi: 10.1016/j.resconrec.2009.08.012.

[113] J.-D. Mathias, X. Balandraud, M. Grediac, Applying a genetic algorithm to the optimization of composite patches, Comput. Struct. 84 (2006) 823–834. doi:10.1016/j.compstruc.2005.12.004.

[114] M. Mitchell, An Introduction to Genetic Algorithms, MIT Press, Cambridge, MA, USA, 1998.

[115] Z. Xiong, X.H. Li, J.C. Liang, L.J. Li, A Multi-Objective Hybrid Algorithm for Optimization of Grid Structures, Int. J. Appl. Mech. 10 (2018). doi:10.1142/S1758825118500096.

[116] P. Maréchal, O. Lenoir, A. Khaled, M.E.C. El Kettani, D. Chenouni, Viscoelasticity effect on a periodic plane medium immersed in water, Acta Acust. United with Acust. 100 (2014) 1036–1043. doi:10.3813/AAA.918783.

[117] S. Babaee, P. Wang, K. Bertoldi, Three-dimensional adaptive soft phononic crystals, J. Appl. Phys. 117 (2015). doi:10.1063/1.4923032.

[118] H.H. Winter, M. Mours, The cyber infrastructure initiative for rheology, Rheol. Acta. 45 (2006) 331–338. doi:10.1007/s00397-005-0041-7.

[119] M.M. Sigalas, C.M. Soukoulis, Elastic-wave propagation through disordered and/or absorptive layered systems, Phys. Rev. B. 51 (1995) 2780–2789. doi:10.1103/PhysRevB.51.2780.

[120] J.Y. Yeh, L.W. Chen, Wave propagations of a periodic sandwich beam by FEM

and the transfer matrix method, Compos. Struct. 73 (2006) 53–60. doi:10.1016/j.compstruct.2005.01.026.

[121] A. Haque, R.F. Ghachi, W.I. Alnahhal, A. Aref, J. Shim, Hybrid Split Hopkinson Pressure Bar to Identify Impulse-dependent Wave Characteristics of Viscoelastic Phononic Crystals, Exp. Mech. (2018). doi:10.1007/s11340-018-00441-8.

[122] P. De Miranda, J.M.C. Dos Santos, Flexural Wave Band Gaps in Phononic Crystal Euler-Bernoulli Beams Using Wave Finite Element and Plane Wave Expansion Methods, Mater. Res. (2017) 1–14. doi:DOI: http://dx.doi.org/10.1590/1980-5373-MR-2016-0877.

[123] D.C. Cassidy, G.J. Holton, F.J. (Floyd J. Rutherford, Harvard Project Physics., Understanding physics, 2002. https://books.google.com/?id=rpQo7f9F1xUC&pg=PA382.

[124] Dassault Systèmes, Abaqus/CAE version 6.14., (2014).

[125] MathWorks Inc., MATLAB. Version 2013a., (2013). Natick, Massachusetts.

[126] T. Chen, K. Tang, G. Chen, X. Yao, A large population size can be unhelpful in evolutionary algorithms, Theor. Comput. Sci. 436 (2012) 54–70.

[127] P.F. Pai, Metamaterial-based broadband elastic wave absorber, J. Intell. Mater. Syst. Struct. 21 (2010) 517–528. doi:10.1177/1045389X09359436.

[128] H. Sun, X. Du, P.F. Pai, Theory of metamaterial beams for broadband vibration absorption, J. Intell. Mater. Syst. Struct. 21 (2010) 1085–1101. doi:10.1177/1045389X10375637.

[129] P.F. Pai, H. Peng, S. Jiang, Acoustic metamaterial beams based on multi-frequency vibration absorbers, Int. J. Mech. Sci. 79 (2014) 195–205. doi:10.1016/j.ijmecsci.2013.12.013.

[130] J.D. Hobeck, D.J. Inman, Magnetoelastic metastructures for passive broadband

vibration suppression, Act. Passiv. Smart Struct. Integr. Syst. 2015. 9431 (2015) 943119. doi:10.1117/12.2083887.

[131] B.C. Essink, J.D. Hobeck, R.B. Owen, D.J. Inman, Magnetoelastic energy harvester for structural health monitoring applications, Act. Passiv. Smart Struct. Integr. Syst. 2015. 9431 (2015) 943123. doi:10.1117/12.2084580.

[132] M.A. Karami, D.J. Inman, Analytical modeling and experimental verification of the vibrations of the zigzag microstructure for energy harvesting, J. Vib. Acoust. Trans. ASME. 133 (2011). doi:10.1115/1.4002783.

[133] O. Abdeljaber, O. Avci, S. Kiranyaz, D.J. Inman, Optimization of linear zigzag insert metastructures for low-frequency vibration attenuation using genetic algorithms, Mech. Syst. Signal Process. 84 (2017) 625–641. doi:10.1016/j.ymssp.2016.07.011.

[134] ANSYS Inc., ANSYS Manual Documentation, (2009) 1286.

[135] D.B. Barker, R.J. Sanford, R. Chona, Determining K and related stress-field parameters from displacement fields, Exp. Mech. 25 (1985) 399–407. doi:10.1007/BF02321339.

[136] J.R. Berger, J.W. Dally, An overdeterministic approach for measuring KI using strain gages, Exp. Mech. 28 (1988) 142–145. doi:10.1007/BF02317564.

[137] P. Compston, P.Y.B. Jar, P. Davies, Matrix effect on the static and dynamic interlaminar fracture toughness of glass-fibre marine composites, Compos. Part B Eng. 29 (1998) 505–516. doi:10.1016/S1359-8368(98)00004-3.

[138] E. Courtney, A. Courtney, M. Courtney, Shock tube design for high intensity blast waves for laboratory testing of armor and combat materiel, Def. Technol. 10 (2014) 245–250. doi:10.1016/j.dt.2014.04.003.

[139] W. Payman, H. Titman, J.F. Thorpe, Explosion waves and shock waves III-The

initiation of detonation in mixtures of ethylene and oxygen and of carbon monoxide and oxygen, Proc. R. Soc. A Math. Phys. Eng. Sci. 152 (1935) 418–445. doi:10.1098/rspa.1935.0199.

[140] C. Cranz, H. Schardin, Kinematographie auf ruhendem Film und mit extrem hoher Bildfrequenz, Zeitschrift Für Phys. 56 (1929) 147–183. doi:10.1007/BF01342777.

[141] A. Fernández-Canteli, A. Argüelles, J. Viña, M. Ramulu, A.S. Kobayashi, Dynamic fracture toughness measurements in composites by instrumented Charpy testing: Influence of aging, Compos. Sci. Technol. 62 (2002) 1315–1325. doi:10.1016/S0266-3538(02)00074-X.

[142] N.A. Fomin, 110 Years of Experiments on Shock Tubes, J. Eng. Phys. Thermophys. 83 (2010) 1118–1135. doi:10.1007/s10891-010-0437-9.

[143] B.A. Gama, S.L. Lopatnikov, J.W. Gillespie, Hopkinson bar experimental technique: A critical review, Appl. Mech. Rev. 57 (2004) 223–250. doi:10.1115/1.1704626.

[144] J. Duffy, R.H. Hawley, The torsional Kolsky (split-Hopkinson) bar, Mech. Test. 8 (1985) 218–230.

[145] S. Heimbs, S. Heller, P. Middendorf, F. Hähnel, J. Weiße, Low velocity impact on CFRP plates with compressive preload: Test and modelling, Int. J. Impact Eng. 36 (2009) 1182–1193. doi:10.1016/j.ijimpeng.2009.04.006.

[146] J.D. Helm, Improved three-dimensional image correlation for surface displacement measurement, Opt. Eng. 35 (1996) 1911. doi:10.1117/1.600624.

[147] C. Bacon, An experimental method for considering dispersion and attenuation in a viscoelastic hopkinson bar, Exp. Mech. 38 (1998) 242–249. doi:10.1007/BF02410385.

[148] H.-H. Forrester, High strain rate compression testing of polymers : PTFE , PCTFE , PVC and PMMA, 2013. Loughborough University.

[149] W.W. Chen, B. Song, Split Hopkinson (Kolsky) Bar: Design, Testing and Applications., 2013.

[150] B. Ahonsi, J.J. Harrigan, M. Aleyaasin, On the propagation coefficient of longitudinal stress waves in viscoelastic bars, Int. J. Impact Eng. 45 (2012) 39–51. doi:10.1016/j.ijimpeng.2012.01.004.

[151] W.G. Halvorsen, D.L. Brown, Impulse technique for structural frequency response testing, S V Sound Vib. 11 (1977) 8–21. doi:10.1121/1.2016847.

[152] P. Wickramarachi, Effects of windowing on the spectral content of a signal, Sound Vib. 37 (2003) 10–11.

[153] J. Shim, D. Mohr, Using split Hopkinson pressure bars to perform large strain compression tests on polyurea at low, intermediate and high strain rates, Int. J. Impact Eng. 36 (2009) 1116–1127. doi:10.1016/j.ijimpeng.2008.12.010.

[154] K.F. Graff, Wave Motion in Elastic Solids, Dover Publications Inc, (1991).

[155] H. Policarpo, M.M. Neves, A.M.R. Ribeiro, Dynamical response of a multi-laminated periodic bar: Analytical, numerical and experimental study, Shock Vib. 17 (2010) 521–535. doi:10.3233/SAV-2010-0545.

[156] C.W. Robinson, G.W. Leppelmeier, Experimental verification of dispersion relations for layered composites, J. Appl. Mech. Trans. ASME. 41 (1974) 89–91. doi:10.1115/1.3423280.

[157] W. Chen, B. Zhang, M.J. Forrestal, A split Hopkinson bar technique for low-impedance materials, Exp. Mech. 39 (1999) 81–85. doi:10.1007/BF02331109.

[158] F. Pervin, W.W. Chen, Dynamic mechanical response of bovine gray matter and white matter brain tissues under compression, J. Biomech. 42 (2009) 731–735.

doi:10.1016/j.jbiomech.2009.01.023.

[159] L. Wang, K. Labibes, Z. Azari, G. Pluvinage, Generalization of split Hopkinson bar technique to use viscoelastic bars, Int. J. Impact Eng. 15 (1994) 669–686. doi:10.1016/0734-743X(94)90166-I.

[160] H. Zhao, G. Gary, J.R. Klepaczko, On the use of a viscoelastic split Hopkinson pressure bar, Int. J. Impact Eng. 19 (1997) 319–330. doi:10.1016/S0734-743X(96)00038-3.

[161] R. Othman, On the use of complex Young's modulus while processing polymeric Kolsky-Hopkinson bars' experiments, Int. J. Impact Eng. 73 (2014) 123–134. doi:10.1016/j.ijimpeng.2014.06.009.

[162] B. Lundberg, R.H. Blanc, Determination of mechanical material properties from the two-point response of an impacted linearly viscoelastic rod specimen, J. Sound Vib. 126 (1988) 97–108. doi:10.1016/0022-460X(88)90401-4.

[163] M. FUJIKAWA, M. TAKASHI, Prony series approximation with Generalized Maxwell Model Based on Collocation Method, J. Japanese Soc. Exp. Mech. 3 (2003) 278–284. doi:10.11395/jjsem2001.3.278.

[164] D. Muhammad Nuruzzaman, M. Asaduzzaman Chowdhury, Effect of Load and Sliding Velocity on Friction Coefficient of Aluminum Sliding Against Different Pin Materials, Am. J. Mater. Sci. 2 (2012) 26–31. doi:10.5923/j.materials.20120201.05.

[165] V.A. Kagan, S.P. Weitzel, Smart structure and integrated system: Reinforced nylon and aluminum self-tapping screws, SAE Tech. Pap. (2002). doi:10.4271/2002-01-2030.

[166] C.E. Cook, Pulse Compression—Key to More Efficient Radar Transmission, Proc. IRE. 48 (1960) 310–316. doi:10.1109/JRPROC.1960.287599.

[167] J.R. Klauder, A.C. Price, S. Darlington, W.J. Albersheim, The Theory and Design of Chirp Radars, Bell Syst. Tech. J. 39 (1960) 745–808. doi:10.1002/j.1538-7305.1960.tb03942.x.

APPENDIX A: DMA TESTS

Temperature Ramp – Elite double 32

Angular frequency	Step time	Temperature	Oscillation strain	Oscillation stress	Tan(delta)	Storage modulus	Loss modulus	Phase angle	Oscillation force
rad/s	s	°C	%	Pa		Pa	Pa	°	N
6.28319	8.52983	-79.676	0.613556	37455	0.094937	6077260	576957	5.42324	0.412005
6.28319	22.234	-80.188	0.613523	53765.8	0.087746	8729900	766011	5.01461	0.591424
6.28319	31.53	-80.169	0.613524	60197.2	0.086088	9775550	841560	4.92036	0.66217
6.28319	40.5303	-79.998	0.613525	65555.9	0.086908	10645000	925135	4.96697	0.721115
6.28319	49.5307	-79.413	0.613525	70558.5	0.087867	11456400	1006630	5.02149	0.776143
6.28319	58.531	-78.762	0.613528	75533	0.08882	12263000	1089190	5.07568	0.830863
6.28319	67.5313	-78.205	0.613528	80619.3	0.089623	13087800	1172970	5.12133	0.886813
6.28319	76.5315	-77.416	0.613529	85906.7	0.090767	13944700	1265730	5.18637	0.944974
6.28319	85.5315	-76.698	0.613527	91552.5	0.091952	14859600	1366370	5.25368	1.00708
6.28319	94.532	-75.97	0.613532	97644.2	0.093441	15846100	1480670	5.33824	1.07409
6.28319	103.532	-75.239	0.613532	104367	0.095169	16934400	1611630	5.43641	1.14804
6.28319	112.532	-74.611	0.61353	111912	0.097133	18155300	1763480	5.54791	1.23104
6.28319	121.532	-73.988	0.613531	120587	0.099551	19558000	1947010	5.68512	1.32646
6.28319	130.533	-73.45	0.613539	130759	0.102149	21201900	2165760	5.83249	1.43835
6.28319	139.533	-72.958	0.613554	142978	0.10501	23175800	2433690	5.99466	1.57276
6.28319	148.533	-72.447	0.613567	157281	0.108472	25484400	2764340	6.19076	1.73009
6.28319	157.534	-72.009	0.613603	174566	0.112106	28272200	3169490	6.3965	1.92023
6.28319	166.534	-71.514	0.613647	195582	0.117498	31654200	3719310	6.70141	2.1514
6.28319	175.534	-71.078	0.613698	221620	0.123565	35839700	4428530	7.04405	2.43782
6.28319	184.534	-70.638	0.613767	253293	0.130404	40922100	5336390	7.42965	2.78622
6.28319	193.535	-70.166	0.61386	291384	0.138422	47019200	6508460	7.88089	3.20522
6.28319	202.535	-69.71	0.614007	336608	0.146263	54244300	7933960	8.32128	3.70269
6.28319	212.975	-69.212	0.614277	399069	0.154826	64200700	9939970	8.80102	4.38976
6.28319	222.536	-68.744	0.614705	463886	0.162829	74483900	12128200	9.24826	5.10275
6.28319	231.536	-68.304	0.615081	533644	0.169942	85533600	14535700	9.6448	5.87008
6.28319	246.941	-67.553	0.615715	678532	0.181515	1.08E+08	19681800	10.288	7.46386
6.28319	256.537	-67.089	0.616144	792513	0.187848	1.26E+08	23746600	10.6389	8.71765

6.28319	265.538	-66.642	0.616438	894240	0.193663	1.42E+08	27581400	10.9604	9.83664
6.28319	274.538	-66.175	0.61677	990510	0.198956	1.58E+08	31337500	11.2524	10.8956
6.28319	287.788	-65.508	0.616992	1124510	0.204014	1.79E+08	36432500	11.5309	12.3696
6.28319	297.539	-65.052	0.616953	1199410	0.206117	1.9E+08	39245800	11.6465	13.1935
6.28319	306.54	-64.601	0.617178	1268840	0.20656	2.01E+08	41588200	11.6709	13.9573
6.28319	315.54	-64.145	0.617316	1334020	0.20614	2.12E+08	43629300	11.6478	14.6742
6.28319	324.54	-63.701	0.617505	1382690	0.204864	2.19E+08	44938700	11.5776	15.2095
6.28319	333.54	-63.251	0.617453	1403110	0.202777	2.23E+08	45160300	11.4628	15.4342
6.28319	342.541	-62.802	0.617082	1405030	0.200101	2.23E+08	44675100	11.3155	15.4553
6.28319	351.541	-62.372	0.616698	1424800	0.197885	2.27E+08	44848900	11.1933	15.6728
6.28319	360.541	-61.937	0.61627	1428890	0.195323	2.28E+08	44447700	11.052	15.7178
6.28319	369.542	-61.486	0.615844	1404740	0.192372	2.24E+08	43089800	10.8891	15.4521
6.28319	378.542	-61.023	0.615504	1393310	0.189075	2.22E+08	42055400	10.7068	15.3264
6.28319	387.542	-60.572	0.615349	1379090	0.185952	2.2E+08	40972300	10.5339	15.17
6.28319	396.542	-60.114	0.61534	1363680	0.183313	2.18E+08	39958900	10.3877	15.0004
6.28319	405.543	-59.668	0.615355	1340530	0.181236	2.14E+08	38848900	10.2726	14.7459
6.28319	414.543	-59.244	0.615363	1308930	0.179779	2.09E+08	37637300	10.1917	14.3983
6.28319	423.543	-58.761	0.615373	1274530	0.178852	2.04E+08	36464300	10.1402	14.0199
6.28319	432.543	-58.314	0.615404	1231920	0.178482	1.97E+08	35172900	10.1197	13.5511
6.28319	441.543	-57.892	0.615449	1185330	0.178371	1.9E+08	33819700	10.1136	13.0386
6.28319	450.543	-57.441	0.615456	1135270	0.178365	1.82E+08	32390100	10.1132	12.488
6.28319	459.544	-56.962	0.615486	1081710	0.178446	1.73E+08	30874000	10.1177	11.8988
6.28319	468.544	-56.535	0.6155	1024090	0.178631	1.64E+08	29257900	10.128	11.265
6.28319	477.544	-56.106	0.615508	964886	0.178889	1.54E+08	27604900	10.1423	10.6137
6.28319	486.544	-55.632	0.615494	902749	0.179278	1.44E+08	25882200	10.1639	9.93024
6.28319	495.545	-55.166	0.615492	838723	0.179756	1.34E+08	24108800	10.1904	9.22595
6.28319	504.545	-54.721	0.615462	776011	0.180292	1.24E+08	22371600	10.2202	8.53612
6.28319	513.545	-54.282	0.615396	713958	0.180869	1.14E+08	20648600	10.2522	7.85354
6.28319	522.545	-53.82	0.615345	653184	0.181559	1.04E+08	18962300	10.2904	7.18502
6.28319	531.546	-53.414	0.615271	594689	0.182203	95089300	17325500	10.3262	6.54158
6.28319	540.546	-52.945	0.61519	535444	0.182962	85616000	15664500	10.3683	5.88989
6.28319	549.546	-52.501	0.615078	477733	0.183642	76392800	14028900	10.4059	5.25506

6.28319	558.546	-52.057	0.61497	424654	0.184264	67909600	12513300	10.4405	4.6712
6.28319	567.546	-51.585	0.614843	372612	0.184733	59594400	11009000	10.4664	4.09873
6.28319	576.547	-51.151	0.614715	324334	0.184783	51883400	9587150	10.4692	3.56768
6.28319	585.547	-50.656	0.614584	280225	0.184286	44840900	8263550	10.4417	3.08248
6.28319	594.547	-50.223	0.614458	239645	0.182964	38364100	7019260	10.3684	2.63609
6.28319	603.547	-49.789	0.614335	202489	0.180639	32435700	5859140	10.2394	2.22738
6.28319	612.548	-49.334	0.614204	169451	0.176986	27166500	4808100	10.0366	1.86396
6.28319	621.548	-48.912	0.614082	140601	0.172356	22563400	3888940	9.77918	1.54661
6.28319	630.548	-48.446	0.613967	115963	0.166256	18631700	3097640	9.43943	1.27559
6.28319	639.548	-48.007	0.613861	95011.4	0.159514	15284500	2438090	9.06313	1.04513
6.28319	648.549	-47.56	0.613775	78555.3	0.151605	12654100	1918420	8.620 67	0.86410 8
6.28319	657.549	-47.112	0.613703	66100.7	0.142806	10662600	1522690	8.12722	0.72710 8
6.28319	666.549	-46.666	0.613648	56562.5	0.133359	9136520	1218440	7.59608	0.62218 7
6.28319	675.549	-46.199	0.613611	46888	0.123227	7583950	934551	7.025	0.51576 8
6.28319	684.55	-45.733	0.613586	35807.9	0.113285	5798760	656913	6.463 2	0.39388 7
6.28319	693.55	-45.304	0.613564	26827	0.104646	4348580	455060	5.974 02	0.29509 7
6.28319	702.55	-44.851	0.613557	20621.3	0.096198	3345500	321832	5.494 85	0.22683 4
6.28319	711.55	-44.405	0.613554	16611.9	0.088816	2696870	239525	5.075 47	0.18273 1
6.28319	720.55	-43.945	0.61355	14101.4	0.082262	2290600	188430	4.702 69	0.15511 6
6.28319	732.282	-43.369	0.613548	12215.7	0.075369	1985360	149634	4.310 18	0.13437 2
6.28319	741.551	-42.914	0.613545	11380.7	0.070893	1850270	131172	4.055 1	0.12518 8
6.28319	750.552	-42.471	0.613542	10988.3	0.067407	1786900	120449	3.856 28	0.12087 1
6.28319	759.552	-42.026	0.613541	10821.2	0.064677	1760060	113835	3.700 55	0.11903 4
6.28319	768.552	-41.56	0.61354	10750.2	0.062617	1748730	109501	3.583 03	0.11825 2
6.28319	777.553	-41.103	0.613539	10720.4	0.061138	1744050	106628	3.498 61	0.11792 5
6.28319	786.553	-40.671	0.61354	10704.8	0.060161	1741620	104777	3.442 81	0.11775 3
6.28319	795.553	-40.182	0.61354	10697	0.059247	1740440	103116	3.390 66	0.11766 7
6.28319	804.553	-39.771	0.61354	10694.4	0.058637	1740080	102033	3.355 81	0.11763 8
6.28319	813.554	-39.321	0.613543	10693.4	0.058076	1739950	101049	3.323 76	0.11762 7
6.28319	822.554	-38.874	0.613542	10704.1	0.057646	1741750	100404	3.299 19	0.11774 5
6.28319	831.554	-38.389	0.613541	10698.3	0.057175	1740850	99533.3	3.272 33	0.11768 1
6.28319	840.555	-37.946	0.613538	10699.9	0.056722	1741170	98762.4	3.246 44	0.11769 9

6.28319	849.555	-37.525	0.613537	10700.5	0.056329	1741300	98085	3.22398	0.117705
6.28319	858.555	-37.091	0.613537	10709.5	0.055952	1742800	97513	3.20246	0.117804
6.28319	867.555	-36.609	0.613536	10711.1	0.055541	1743120	96813.8	3.17897	0.117823
6.28319	876.555	-36.144	0.613537	10714.4	0.055106	1743680	96087.9	3.15417	0.117858
6.28319	885.556	-35.68	0.613537	10727.3	0.054716	1745820	95523.6	3.13185	0.118
6.28319	894.556	-35.227	0.613536	10727.8	0.054397	1745940	94973.5	3.11364	0.118006
6.28319	903.556	-34.817	0.613535	10733.9	0.054065	1746960	94449.6	3.09469	0.118072
6.28319	912.556	-34.367	0.613536	10733.7	0.053718	1746970	93844.5	3.07488	0.118071
6.28319	921.557	-33.931	0.613537	10736.2	0.053351	1747390	93225.9	3.05391	0.118098
6.28319	930.557	-33.467	0.613535	10745.1	0.052969	1748890	92636.1	3.03204	0.118196
6.28319	939.557	-33.013	0.613535	10752	0.052641	1750040	92123.4	3.01331	0.118272
6.28319	948.557	-32.562	0.613532	10758.7	0.052301	1751170	91588.2	2.99391	0.118346
6.28319	957.558	-32.116	0.613534	10764.9	0.05193	1752210	90992.3	2.9727	0.118414
6.28319	966.558	-31.633	0.613534	10769.8	0.051567	1753040	90399.5	2.95197	0.118468
6.28319	975.558	-31.175	0.613536	10769.7	0.051216	1753050	89784.2	2.93189	0.118467
6.28319	984.558	-30.739	0.613537	10773.5	0.050936	1753700	89327.1	2.91592	0.118509
6.28319	993.558	-30.304	0.613536	10784.2	0.050571	1755470	88775.4	2.89502	0.118626
6.28319	1002.56	-29.882	0.613535	10787	0.05029	1755950	88306.8	2.87898	0.118657
6.28319	1011.56	-29.401	0.613537	10797.7	0.049963	1757720	87820.8	2.86029	0.118775
6.28319	1020.56	-28.945	0.613537	10803.3	0.04966	1758650	87333.8	2.84295	0.118836
6.28319	1029.56	-28.532	0.613538	10815	0.049417	1760580	87002.6	2.82908	0.118965
6.28319	1038.56	-28.063	0.613534	10813.7	0.049109	1760410	86452.4	2.81149	0.118951
6.28319	1047.56	-27.628	0.613534	10820.2	0.048819	1761490	85993.7	2.79489	0.119022
6.28319	1056.56	-27.173	0.613535	10828.7	0.048604	1762890	85682.8	2.78259	0.119116
6.28319	1065.56	-26.712	0.613537	10837.9	0.048311	1764410	85240.3	2.76586	0.119217
6.28319	1074.56	-26.245	0.613534	10844.4	0.048049	1765490	84830	2.75089	0.119288
6.28319	1083.56	-25.815	0.613536	10848.3	0.047759	1766150	84349.7	2.73431	0.119332
6.28319	1092.56	-25.366	0.613536	10857.7	0.047504	1767690	83972.9	2.71975	0.119434
6.28319	1101.56	-24.909	0.613537	10868.7	0.047242	1769510	83594.3	2.70473	0.119556
6.28319	1110.56	-24.475	0.613538	10868.6	0.046971	1769510	83115.5	2.68926	0.119554
6.28319	1119.56	-24.045	0.613535	10880.5	0.046708	1771480	82742.9	2.67425	0.119685
6.28319	1128.56	-23.589	0.613534	10891.6	0.04643	1773310	82335.4	2.65836	0.119807

6.28319	1137.56	-23.127	0.613536	10903.9	0.046172	1775340	81970.1	2.64356	0.119943
6.28319	1146.56	-22.676	0.613534	10905.9	0.045973	1775680	81633	2.6322	0.119965
6.28319	1155.56	-22.175	0.613536	10916.7	0.045676	1777450	81186.2	2.6152	0.120084
6.28319	1164.56	-21.752	0.613534	10925.6	0.045391	1778940	80747.9	2.59893	0.120182
6.28319	1172.56	-21.33	0.613534	10934.7	0.045163	1780440	80410.5	2.5859	0.120282
6.28319	1181.56	-20.896	0.613533	10937.5	0.044968	1780910	80083.4	2.57472	0.120313
6.28319	1190.56	-20.471	0.613535	10949.6	0.044771	1782880	79821.7	2.56348	0.120445
6.28319	1199.56	-20.012	0.613532	10955.2	0.044488	1783830	79358.6	2.54728	0.120507
6.28319	1208.56	-19.57	0.613534	10967.7	0.044272	1785880	79064.8	2.53495	0.120645
6.28319	1217.56	-19.129	0.613536	10981.5	0.044057	1788130	78779.6	2.52264	0.120796
6.28319	1226.56	-18.672	0.613533	10986.8	0.043846	1789030	78442.2	2.5106	0.120855
6.28319	1235.56	-18.248	0.613535	10997.3	0.043629	1790740	78127.3	2.49814	0.12097
6.28319	1244.57	-17.767	0.613535	11007.8	0.043395	1792470	77784.4	2.48479	0.121086
6.28319	1253.57	-17.288	0.613532	11011.2	0.043146	1793060	77363.9	2.47057	0.121124
6.28319	1262.57	-16.847	0.613534	11023.9	0.042969	1795130	77135	2.46043	0.121263
6.28319	1271.57	-16.374	0.613531	11037.4	0.042733	1797350	76806.1	2.44692	0.121411
6.28319	1280.57	-15.986	0.613531	11041.7	0.042499	1798070	76416.6	2.43356	0.121459
6.28319	1289.57	-15.496	0.613532	11051.6	0.042229	1799700	75998.9	2.41809	0.121567
6.28319	1298.57	-15.038	0.613532	11066	0.042049	1802060	75775.4	2.40783	0.121726
6.28319	1307.57	-14.643	0.613532	11075.5	0.041878	1803620	75531.2	2.39801	0.12183
6.28319	1316.57	-14.17	0.613531	11085.2	0.041686	1805220	75252.7	2.38705	0.121937
6.28319	1325.57	-13.735	0.61353	11095.3	0.041492	1806880	74970.7	2.37594	0.122048
6.28319	1334.57	-13.262	0.61353	11101.5	0.041228	1807910	74536	2.36084	0.122116
6.28319	1343.57	-12.779	0.613533	11116.9	0.040966	1810430	74166.3	2.34587	0.122286
6.28319	1352.57	-12.323	0.61353	11129.6	0.040789	1812510	73931.4	2.33577	0.122425
6.28319	1361.57	-11.871	0.61353	11135.1	0.0406	1813430	73625.8	2.32495	0.122486
6.28319	1370.57	-11.453	0.61353	11144.4	0.04043	1814960	73378.1	2.31519	0.122588
6.28319	1379.57	-11.013	0.613529	11151.7	0.040216	1816170	73039.6	2.30298	0.122669
6.28319	1388.57	-10.575	0.61353	11169	0.040053	1818990	72855.4	2.29362	0.122859
6.28319	1397.57	-10.12	0.613528	11180.9	0.039809	1820960	72489.7	2.27966	0.12299
6.28319	1406.57	-9.639	0.613529	11184.1	0.039609	1821490	72147.9	2.26826	0.123025
6.28319	1415.57	-9.234	0.613526	11196.6	0.039448	1823540	71935.3	2.25904	0.123163

6.28319	1424.57	-8.782	0.613528	11207.6	0.039273	1825340	71687.3	2.24904	0.123284
6.28319	1433.57	-8.314	0.613529	11220.2	0.039116	1827410	71480	2.24001	0.123423
6.28319	1442.57	-7.838	0.613528	11231.7	0.038949	1829280	71248.9	2.23049	0.123548
6.28319	1451.57	-7.394	0.613528	11245.8	0.038718	1831610	70915.3	2.21724	0.123704
6.28319	1460.57	-6.966	0.613526	11250.5	0.03856	1832380	70656.1	2.20821	0.123756
6.28319	1469.57	-6.496	0.613531	11262	0.038386	1834250	70409.4	2.19827	0.123882
6.28319	1478.57	-6.064	0.613528	11274.4	0.038282	1836290	70295.9	2.1923	0.124018
6.28319	1487.57	-5.64	0.613532	11285.7	0.038099	1838130	70030.5	2.18184	0.124143
6.28319	1496.57	-5.174	0.613528	11292.4	0.037954	1839250	69807	2.17357	0.124217
6.28319	1505.57	-4.737	0.613529	11308.8	0.03778	1841930	69588.3	2.16362	0.124397
6.28319	1514.57	-4.307	0.613529	11318.7	0.037594	1843550	69306.5	2.15296	0.124506
6.28319	1523.57	-3.782	0.61353	11331.6	0.037348	1845670	68931.8	2.13888	0.124648
6.28319	1532.57	-3.366	0.613529	11347.8	0.03721	1848310	68775.7	2.13099	0.124826
6.28319	1541.57	-2.893	0.613528	11359.6	0.036988	1850250	68437.2	2.11829	0.124955
6.28319	1550.57	-2.478	0.613529	11367.3	0.03686	1851520	68246.9	2.11096	0.125041
6.28319	1559.57	-2.016	0.613528	11378.1	0.036643	1853300	67904.5	2.09837	0.125159
6.28319	1568.57	-1.557	0.613527	11386.9	0.036452	1854740	67608	2.08759	0.125256
6.28319	1577.57	-1.112	0.613527	11405.9	0.036257	1857850	67360.3	2.07647	0.125465
6.28319	1586.57	-0.68	0.613527	11412.5	0.036129	1858930	67161	2.06913	0.125537
6.28319	1595.57	-0.231	0.613529	11427.8	0.035973	1861430	66961.4	2.06022	0.125706
6.28319	1604.57	0.397	0.613526	11438.6	0.035763	1863220	66634.8	2.04821	0.125825
6.28319	1613.57	0.764	0.613526	11455.7	0.035567	1866010	66368.2	2.03698	0.126013
6.28319	1622.58	1.235	0.613526	11458.3	0.035423	1866440	66115.2	2.02875	0.126041
6.28319	1631.58	1.639	0.613525	11478.2	0.035311	1869690	66021.2	2.02235	0.126266
6.28319	1640.58	2.083	0.613524	11483.9	0.035237	1870630	65915.7	2.01811	0.126323
6.28319	1649.58	2.553	0.613526	11495.6	0.035073	1872540	65676.2	2.00873	0.126452
6.28319	1658.58	2.992	0.613531	11530.1	0.034979	1878150	65696.1	2.00334	0.126831
6.28319	1667.58	3.336	0.613532	11535.5	0.034822	1879040	65431.2	1.99433	0.12689
6.28319	1683.83	4.136	0.613525	11544.3	0.034572	1880520	65013.5	1.98005	0.126988
6.28319	1693.58	4.568	0.613526	11554.7	0.034472	1882210	64882.8	1.97429	0.127102
6.28319	1702.58	4.977	0.613527	11567.9	0.034324	1884360	64679.5	1.96586	0.127247
6.28319	1711.58	5.365	0.613527	11579.4	0.034215	1886250	64538.8	1.95963	0.127374

6.28319	1720.58	5.75	0.613525	11588.6	0.034178	1887760	64520	1.9575	0.127475
6.28319	1729.58	6.241	0.613528	11608.1	0.034042	1890930	64370.1	1.94968	0.127689
6.28319	1738.58	6.664	0.613528	11611.5	0.033901	1891500	64122.7	1.94161	0.127727
6.28319	1747.58	7.155	0.613524	11624.9	0.033704	1893710	63826.2	1.93039	0.127874
6.28319	1756.58	7.736	0.613526	11646.3	0.033561	1897180	63671.4	1.92218	0.128109
6.28319	1765.58	8.373	0.613526	11663.3	0.033361	1899970	63384.1	1.91071	0.128296
6.28319	1774.58	8.976	0.613525	11674.8	0.033242	1901850	63221.7	1.90393	0.128423
6.28319	1783.58	9.577	0.613527	11695.7	0.033039	1905270	62947.9	1.8923	0.128653
6.28319	1792.58	10.162	0.613526	11708.9	0.032825	1907420	62611.4	1.88006	0.128797
6.28319	1801.58	10.716	0.613525	11725.2	0.032664	1910110	62391.5	1.87084	0.128978
6.28319	1810.58	11.246	0.613524	11739.9	0.032494	1912510	62145.8	1.86113	0.129139
6.28319	1819.58	12.009	0.613525	11759.5	0.032242	1915710	61765.5	1.84667	0.129354
6.28319	1828.58	12.781	0.613526	11783	0.032025	1919550	61474.4	1.83429	0.129613
6.28319	1837.58	13.568	0.613524	11797.9	0.031783	1922000	61087.2	1.82043	0.129776
6.28319	1846.58	14.354	0.613527	11822.4	0.031555	1926000	60775.3	1.80738	0.130046
6.28319	1855.58	15.126	0.613526	11841.2	0.031324	1929080	60426.1	1.79413	0.130254
6.28319	1864.58	15.854	0.613525	11861.2	0.031119	1932350	60132.6	1.7824	0.130473
6.28319	1873.58	16.598	0.613525	11888.5	0.030881	1936810	59810	1.76877	0.130773
6.28319	1882.58	17.325	0.613524	11907	0.030685	1939850	59523.2	1.75754	0.130977
6.28319	1891.58	17.821	0.613523	11927.6	0.030522	1943210	59309.7	1.74821	0.131203
6.28319	1900.58	17.992	0.613526	11936.8	0.030448	1944710	59213.3	1.74403	0.131305
6.28319	1909.58	17.982	0.613525	11948.1	0.030462	1946540	59294.7	1.74478	0.131429
6.28319	1918.58	18.314	0.613524	11953	0.030362	1947350	59124.7	1.73906	0.131483
6.28319	1927.58	18.616	0.613527	11961	0.030232	1948650	58912.3	1.73166	0.131571
6.28319	1936.58	18.702	0.613528	11967	0.030205	1949630	58888.2	1.73008	0.131637
6.28319	1945.59	18.965	0.613527	11976.6	0.030112	1951200	58754.4	1.72476	0.131742
6.28319	1954.59	19.301	0.613525	11984.7	0.029991	1952540	58557.7	1.71781	0.131832
6.28319	1963.59	19.474	0.613526	11992.8	0.029927	1953860	58473.4	1.71418	0.131921
6.28319	1972.59	19.721	0.613523	12004.2	0.029842	1955720	58362.9	1.70932	0.132046
6.28319	1981.59	20.068	0.613524	12013.9	0.029726	1957310	58183.8	1.7027	0.132153
6.28319	1990.59	20.264	0.613524	12021.3	0.029664	1958530	58098	1.69913	0.132234
6.28319	1999.59	20.568	0.613526	12030.1	0.029548	1959960	57913	1.69248	0.132331

6.28319	2008.59	20.519	0.613528	12038.5	0.029563	1961320	57981.9	1.69332	0.132424
6.28319	2017.59	20.266	0.613526	12035.9	0.029663	1960890	58166.4	1.69908	0.132394

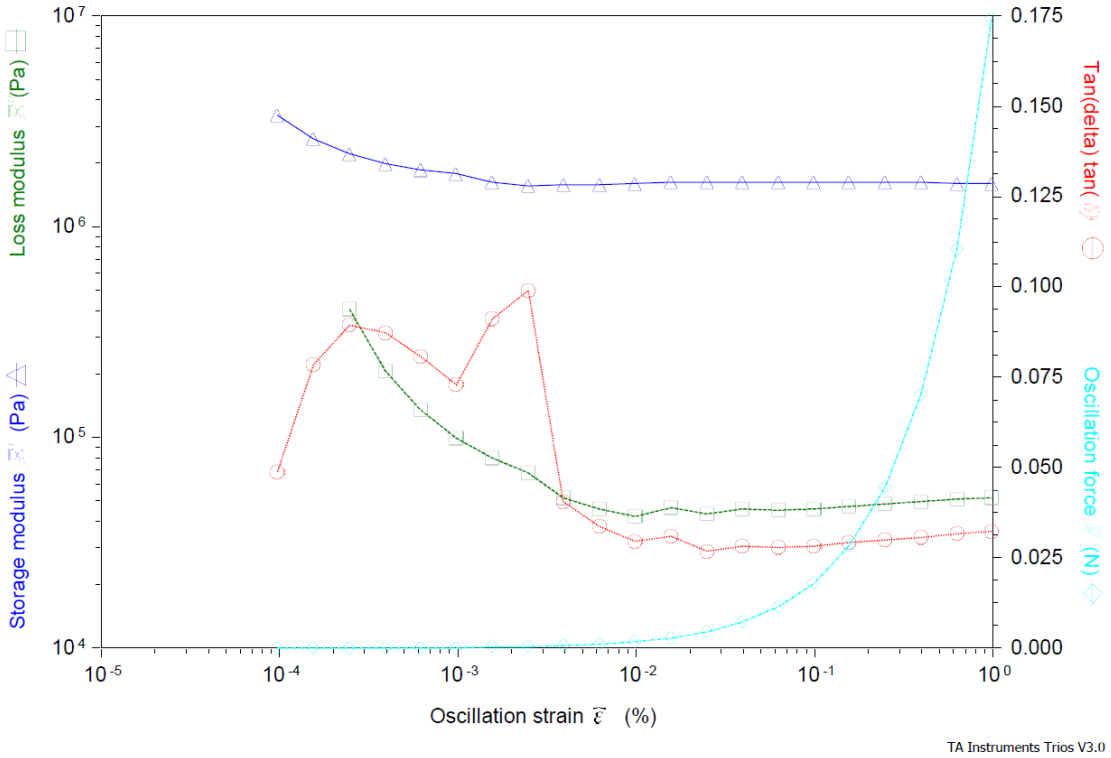

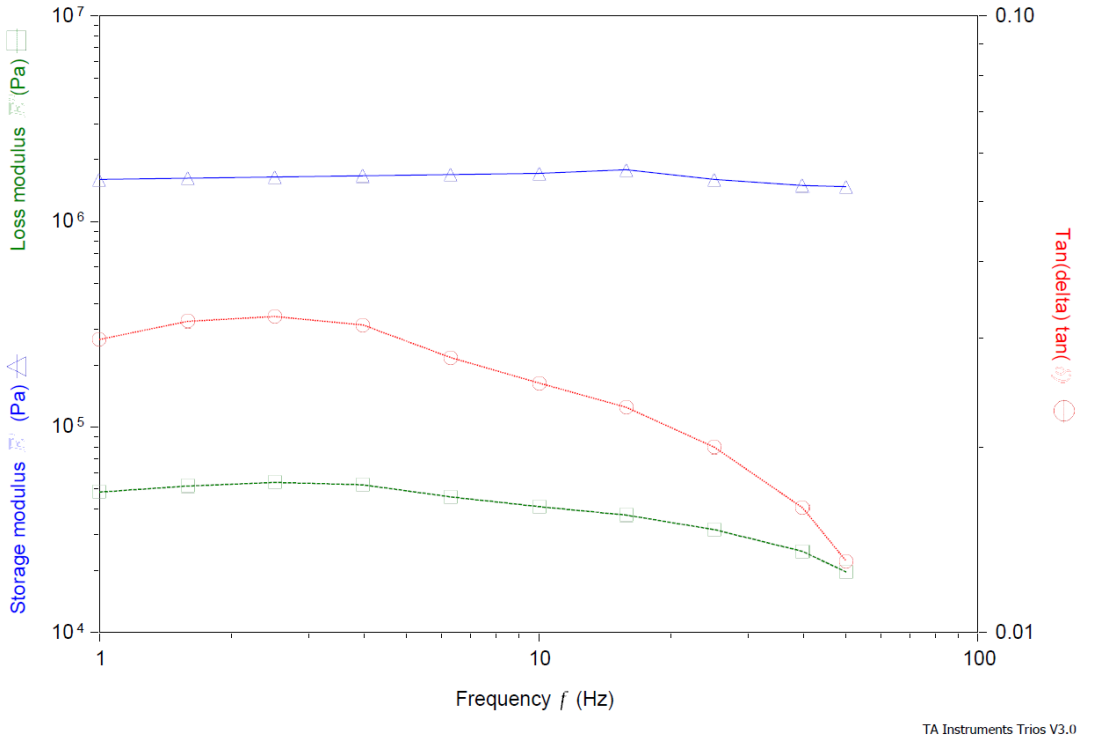

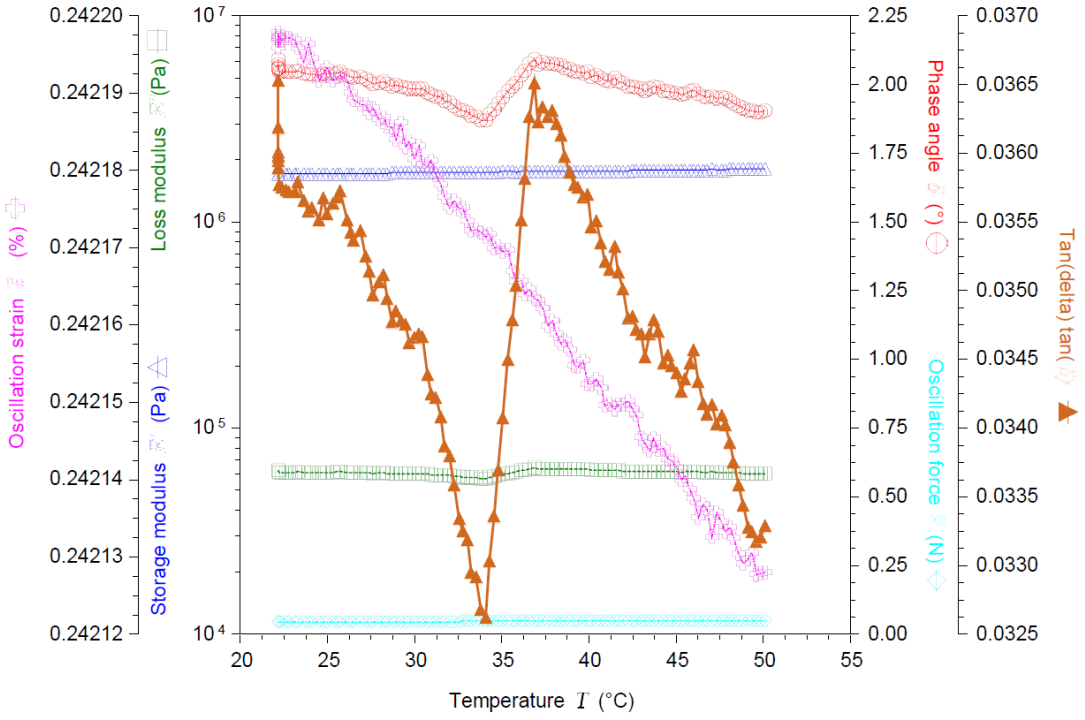
Oscillation strain (%)
Loss modulus (Pa)
Storage modulus (Pa)
Phase angle (°)
Oscillation force (N)
Tan(delta) tan(
Temperature T (°C)
0.24220
0.24219
0.24218
0.24217
0.24216
0.24215
0.24214
0.24213
0.24212
10^7
10^6
10^5
10^4
2.25
2.00
1.75
1.50
1.25
1.00
0.75
0.50
0.25
0.00
0.0370
0.0365
0.0360
0.0355
0.0350
0.0345
0.0340
0.0335
0.0330
0.0325
20
25
30
35
40
45
50
55

APPENDIX B: PHONONIC CRYSTALS SHAKER TESTS

Cylindrical specimens were manufactured using cylinders of polymers: Elite Double 32/Elite double 8/Hapflex 560 alternating in periodic arrangement with aluminum alloy cylinders (Table 21). Different specimens of 40 mm diameter are described in Table 22. The experimental set up for the vibration test is shown in Figure 66(a). The specimens were placed on a circular base connected to the force transducer and were attached to an accelerometer at the top Figure 115. These linear perturbation tests were performed by applying a chirp sine sweep signal to the specimen up from 1 Hz to 20 kHz. The pseudo-transfer functions were determined from the fast Fourier transform (FFT) ratio of acceleration and force signal as below:

$$FRF(\omega) = \frac{|A_{out}(\omega)|}{|F_{in}(\omega)|}$$

Where $|A_{out}(\omega)|$ and $|F_{in}(\omega)|$ represents the frequency spectrum of acceleration and force signals, respectively.

Table 21. Elastic Properties of the Materials

Properties	Elite Double-32	Hapflex-560	Elite Double-8
Elastic Modulus (MPa)	0.83	9.58	0.28
Density (kg/m^3)	1196	1060	980

Table 22. Shaker test specimen's composition

Specimen		Composition		Number of Layers
		Aluminum alloy	Polymer	
Elite double 32	510ED32	5 mm	10 mm	4
	1010ED32	10 mm	10 mm	3
Elite double 8	510ED8	5 mm	10 mm	4

Specimen		Composition		Number of Layers
		Aluminum alloy	Polymer	
	1010ED8	10 mm	10 mm	3
	520ED8	5 mm	20 mm	3
Hapflex 560	510H560	5 mm	10 mm	4
	1010H560	10 mm	10 mm	3
	520H560	5 mm	20 mm	3

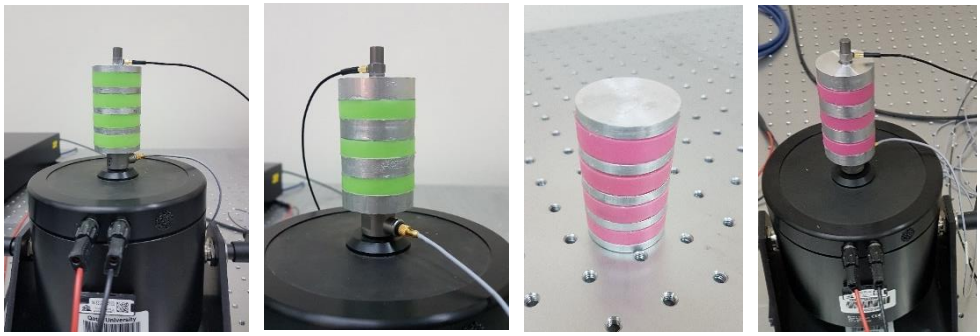

(A) (B) (C) (D)

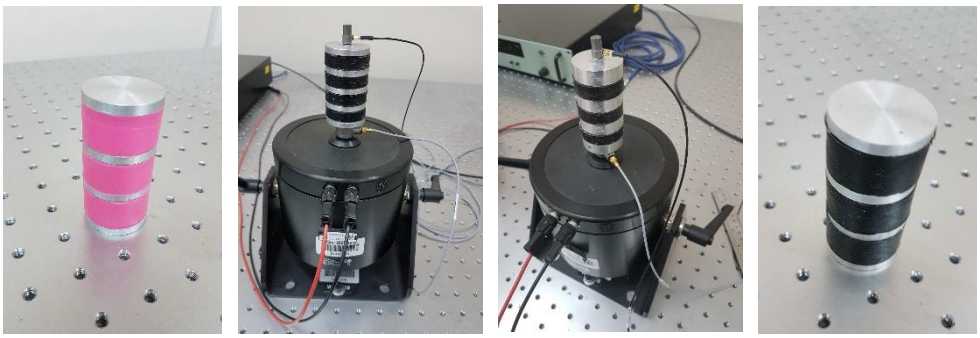

(E) (F) (G) (H)

Figure 115. Vibration shaker experiment set-up for specimens (A) 510ED32 (B) 1010ED32 (C) 510ED8 (D) 1010ED8 (E) 520 ED8 (F) 510H560 (G) 1010H560 (H) 520H560, respectively

The pseudo-transfer functions for specimens 510ED32, 1010ED32, 510ED8, 1010ED8, 520 ED8, 510H560, 1010H560, 520H560 are shown in Figure 116 to

Figure 123, respectively.

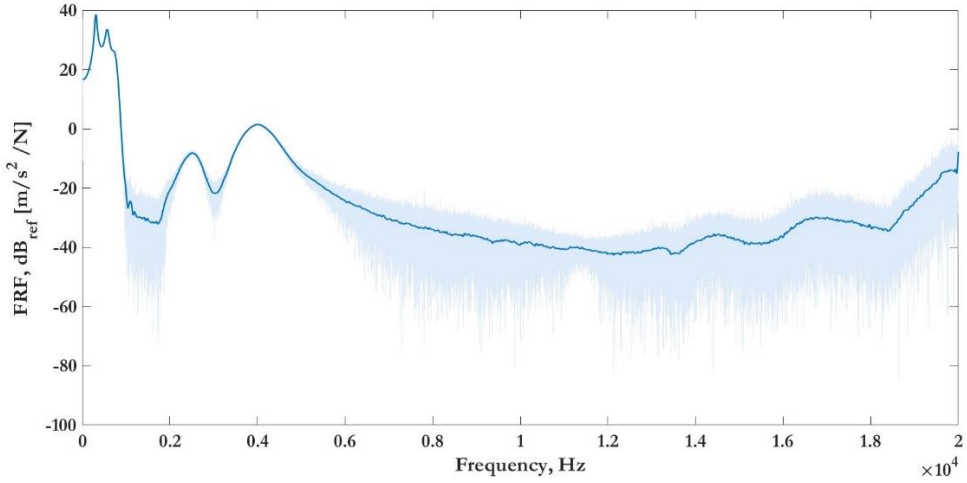

Figure 116. Frequency response function of the specimen 510ED32

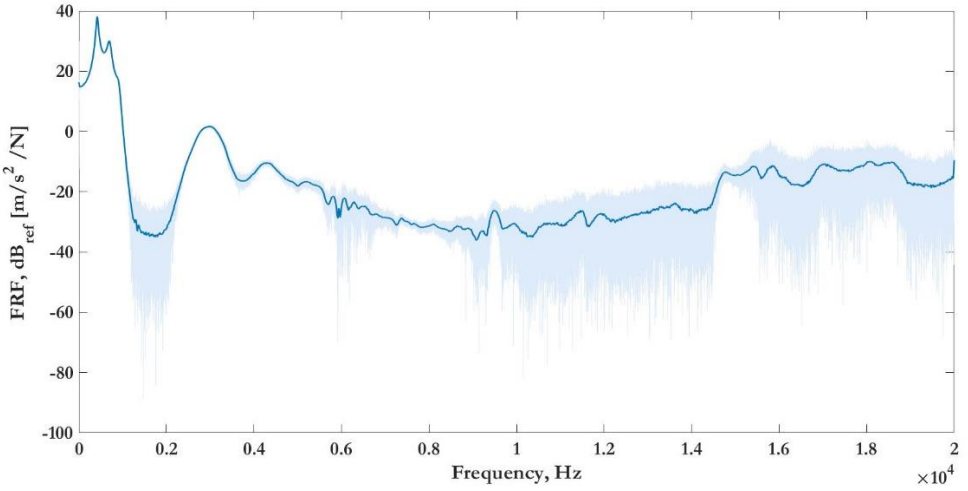

Figure 117. Frequency response function of the specimen 1010ED32

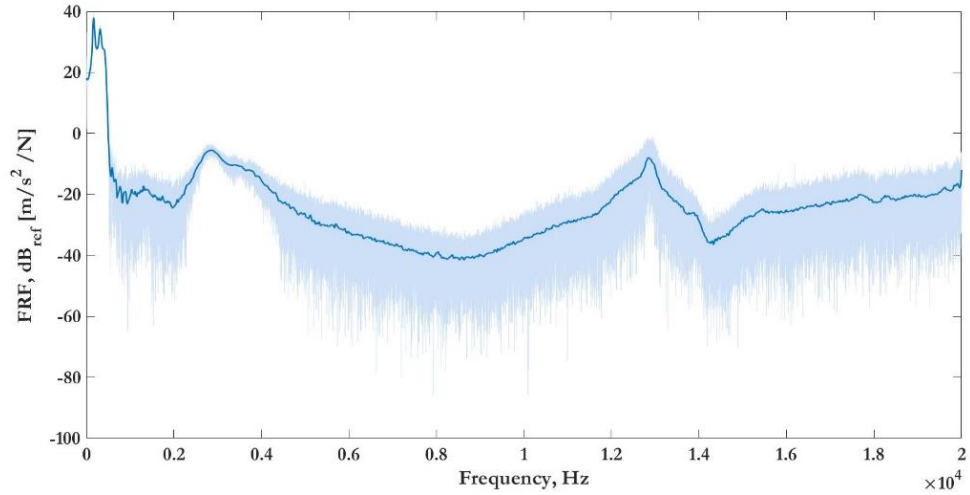

Figure 118. Frequency response function of the specimen 510ED8

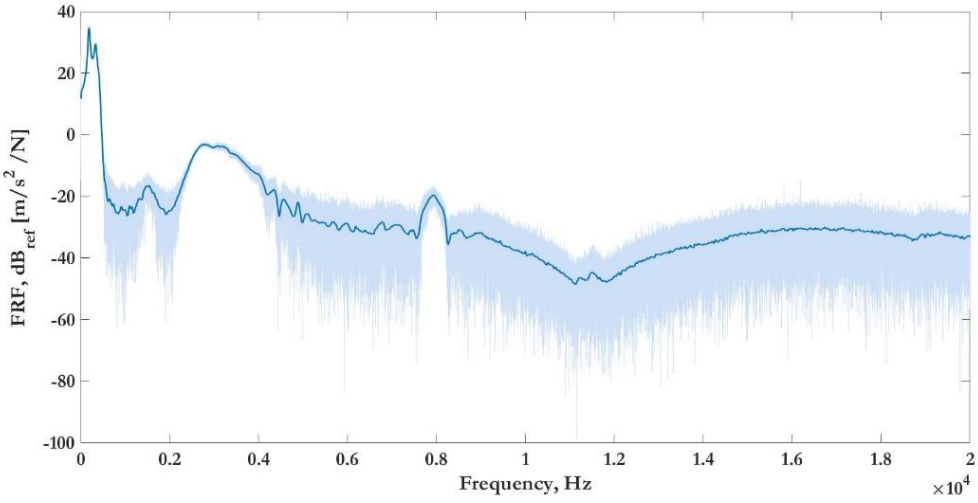

Figure 119. Frequency response function of the specimen 1010ED8

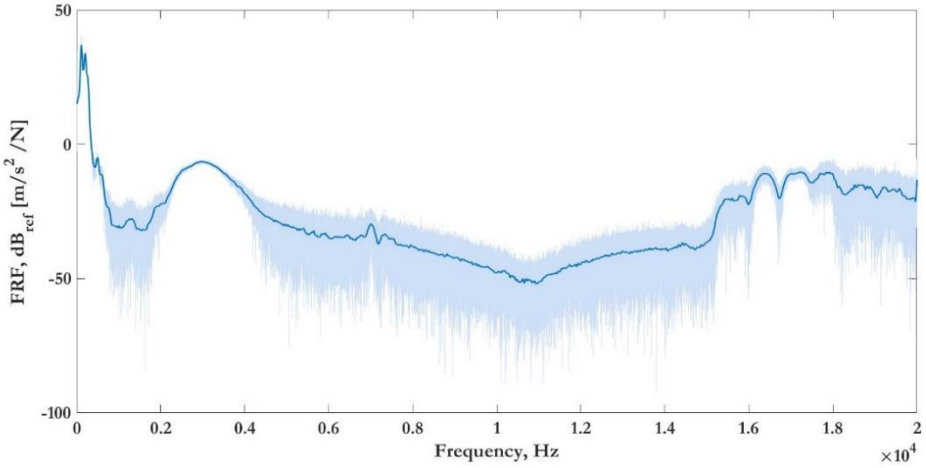

Figure 120. Frequency response function of the specimen 520ED8

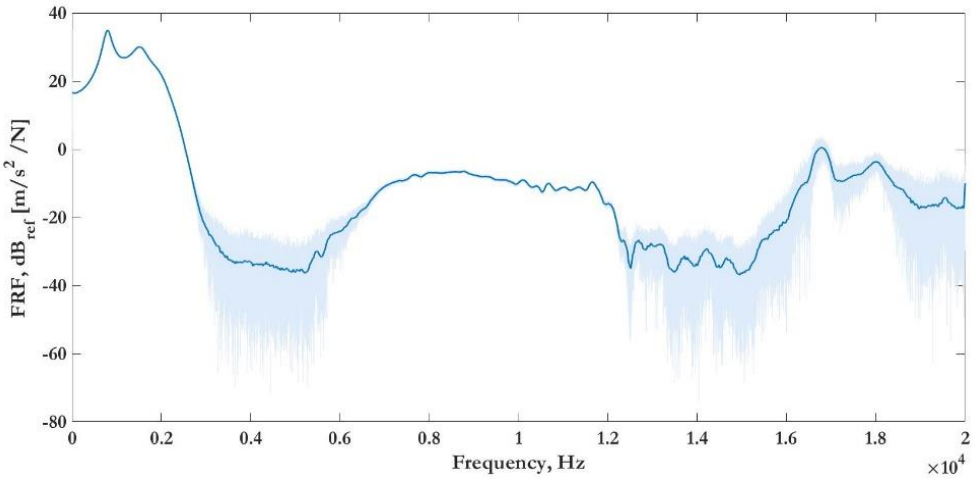

Figure 121. Frequency response function of the specimen 510H560

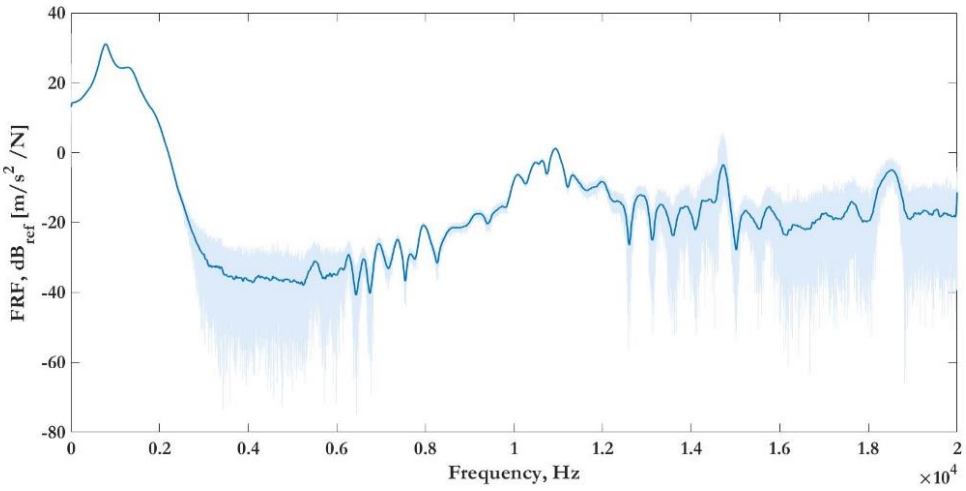

Figure 122. Frequency response function of the specimen 1010H560

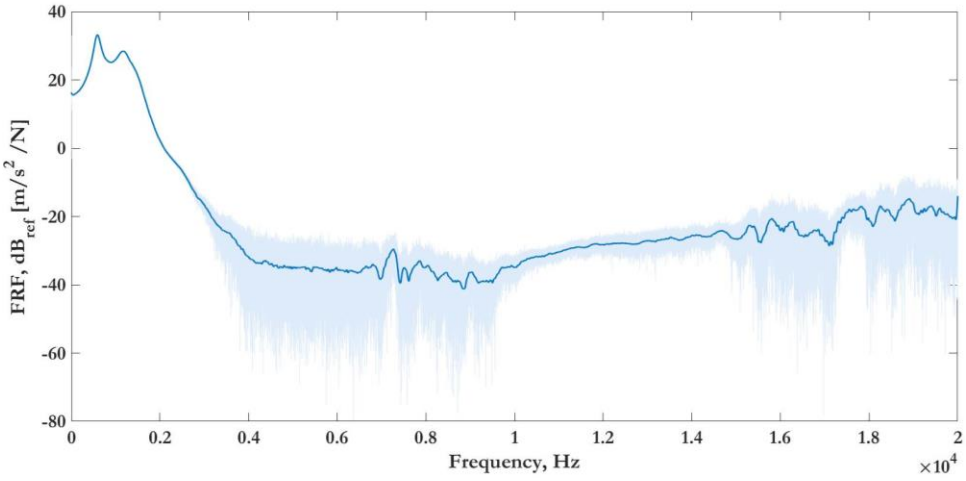

Figure 123. Frequency response function of the specimen 520H560

APPENDIX C: LABVIEW G PROGRAM